National Aeronautics and
Space Administration

ANALYTICAL STUDY OF THE EFFECTS OF WIND TUNNEL TURBULENCE ON TURBOFAN ROTOR NOISE

FINAL REPORT

by

P.R. Gliebe and E.J. Kerschen

GENERAL ELECTRIC COMPANY

Prepared For

National Aeronautics and Space Administration

NASA Ames Research Center

Contract NAS2-10002

1. Report No.	2. Government Accession No.	3. Recipient's Catalog No.
NASA CR-152359		

4. Title and Subtitle	5. Report Date
ANALYTICAL STUDY OF THE EFFECTS OF WIND TUNNEL TURBULENCE ON TURBOFAN ROTOR NOISE	December 1979
	6. Performing Organization Code
7. Author(s)	8. Performing Organization Report No.
P.R. Gliebe and E.J. Kerschen	
	10. Work Unit No.
9. Performing Organization Name and Address	
General Electric Company Aircraft Engine Group Cincinnati, Ohio 45215	11. Contract or Grant No. NAS2-10002
	13. Type of Report and Period Covered Final Contract Report
12. Sponsoring Agency Name and Address	
National Aeronautics and Space Administration Washington, D.C. 20546	14. Sponsoring Agency Code

15. Supplementary Notes

Project Manager, Warren Ahtye, NASA Ames Research Center, Moffett Field, California

16. Abstract

An analytical study of the effects of wind tunnel turbulence on turbofan rotor noise was carried out to evaluate the effectiveness of the NASA Ames 40 by 80 foot wind tunnel in simulating flight levels of fan noise. A previously developed theory for predicting rotor/turbulence interaction noise was refined and extended to include first-order effects of inlet turbulence anisotropy. This theory was then verified by carrying out extensive data/theory comparisons. The resulting model computer program was then employed to carry out a parametric study of the effects of fan size, blade number, and operating line on rotor/turbulence noise for outdoor test stand, NASA Ames wind tunnel, and flight inlet turbulence conditions. A major result of this study is that although wind tunnel rotor/turbulence noise levels are not as low as flight levels they are substantially lower than the outdoor test stand levels and do not mask other sources of fan noise.

17. Key Words (Suggested by Author(s))	18. Distribution Statement
Fan Noise Atmospheric Turbulence Wind Tunnels Turbulence Contraction	Unclassified - Unlimited

19. Security Classif. (of this report)	20. Security Classif. (of this page)	21. No. of Pages	22. Price*
UNCLASSIFIED	UNCLASSIFIED	119	

* For sale by the National Technical Information Service, Springfield, Virginia 22151

TABLE OF CONTENTS

LIST OF ILLUSTRATIONS

LIST OF ILLUSTRATIONS (Continued)

LIST OF ILLUSTRATIONS (Continued)

LIST OF ILLUSTRATIONS (Concluded)

LIST OF TABLES

1.0 SUMMARY

An analytical study of the effects of wind tunnel turbulence on turbofan rotor noise was carried out. A previously established prediction model was used to evaluate wind tunnel turbulence/rotor interaction noise. The prediction model was first extended to include the effects of turbulence anisotropy by deriving and incorporating a turbulence spectrum model based on axisymmetric turbulence theory. The extended prediction model was verified through extensive data/theory comparisons with scale model and full-scale fan measurements, with various inlet turbulence conditions.

It was found that the classical Ribner/Tucker sudden-contraction theory does not adequately describe the turbulence free-stream to fan-face contraction effects for the wind tunnel environment, and, hence, some uncertainty in the prediction of wind tunnel turbulence/rotor interaction noise was identified. It was estimated that the predicted levels could be at most 6 dB too low for the highest contractions normally encountered.

A literature survey of fan inlet turbulence properties was carried out, and data ranges were identified for anechoic chambers, outdoor test stands, wind tunnels, and atmospheric flight environment. Considerable scatter and variability in turbulence properties was found to exist, and "expected average" values for the various test site conditions were determined.

A parametric study of the effects of fan rotor size, blade number, operating line, and tip speed on rotor/turbulence noise was carried out. The predicted noise levels for the NASA-Ames 40x80 wind tunnel environment were compared with both outdoor test stand levels and altitude flyover levels. The extended rotor/turbulence noise prediction model was used to predict the noise level trends with tip speed, rotor geometry, and environmental conditions.

Results of the study showed the Ames wind tunnel rotor/turbulence noise levels to be 15-20 dB lower than outdoor test stand levels for all combinations of tip speed, rotor diameter, blade number, and operating line investigated. The wind tunnel levels were also compared with flight levels and found to be

10-15 dB higher, but still lower than the other sources of fan noise (broadband, multiple-pure-tones, rotor/stator, etc.).

Due to the random variability of atmospheric turbulence properties, it was found that a wide range in rotor/turbulence noise levels can be expected from different conditions and that the wind-tunnel and flight bands can overlap.

It was concluded that wind tunnel turbulence/rotor interaction noise is sufficiently low such that forward flight effects are adequately simulated as far as inlet "clean-up" effects are concerned. Although the wind tunnel turbulence characteristics (small-scale, low intensity) are far different from atmospheric flight turbulence characteristics (very large scale, moderate-to-high intensity), the net effect on noise is similar.

It was found that rotor/turbulence noise, for contracting large-scale inlet turbulence, is characterized by strong, narrow peaks at blade passing frequency and its harmonics, with no significant contribution to the fan broadband noise levels. For axial length scales sufficiently large (greater than one diameter), the transverse turbulence intensity and transverse length scale/blade spacing ratio are the primary parameters which control the rotor/turbulence noise levels for a given fan.

2.0 INTRODUCTION

It is now well known that acoustic testing of turbofan engines in an outdoor test stand facility does not yield the same noise characteristics as those measured in flight. As discussed in Reference 1, atmospheric turbulence is drawn into the inlet during ground static testing, undergoing substantial elongation and contraction. Because of the large contraction of the inflow streamlines, the turbulent eddies convecting with the flow appear as long "sausages" as they pass through the rotor. Many blades will successively "chop" the same eddy, producing blade-passing frequency tones as well as broadband noise. This rotor/turbulence interaction is usually strong enough to dominate other sources of fan inlet noise during static testing.

In flight, the fan inlet flow does not undergo very much contraction because of the aircraft forward motion. The fan inlet contraction ratio, C, defined as fan face through-flow velocity divided by flight speed, is not too different from unity at normal flight approach speeds. At typical approach altitudes (500-1000 ft or 150-300 meters), the atmospheric turbulence scales or eddy sizes are much larger than on the ground, so that the eddies do not appear to the rotor as "sausages" which are successively "chopped" by the rotor blades, but may have cross sections as large as, or larger than, the inlet itself. Very little rotor/turbulence interaction noise is therefore produced in flight, allowing other sources to dominate the observed noise spectrum.

It is desirable to have a "static" or ground-based test facility for acoustic evaluation of turbofan engines; one which correctly simulates the flight inlet turbulence conditions. Flight testing is not only costly and time-consuming, but has severe limits on test conditions, power settings, etc., and is subject to variability and uncertainty with respect to atmospheric propagation, ground reflections, and aircraft location. For research and development purposes, extensive hardware changes and elaborate instrumentation and data acquisition equipment are often required which cannot be easily implemented in a flight test. Acoustic testing of full-scale turbofan engines

in a large wind tunnel is a viable alternative to flight testing. Flight contraction ratios and aircraft speeds can be simulated in a wind tunnel, under more controlled conditions, with test measurement capability and flexibility rivaling that of a conventional outdoor test stand.

The NASA-Ames 40x80 wind tunnel facility at Moffett Field, California, has recently been used for acoustic evaluation of turbofan engines under simulated flight conditions. This wind tunnel facility has turbulence properties which are different from both the outdoor test stand and flight altitude environment, and it is important to know whether the rotor/turbulence interaction noise in the tunnel is low enough to provide a true simulation of flight noise characteristics.

The primary objective of the present study was to evaluate the degree to which the NASA-Ames 40x80 wind tunnel simulates flight conditions in terms of producing sufficiently low levels of rotor/turbulence interaction noise. Guidelines for the ranges of fan size, blade number, and operating speeds over which sufficiently low rotor/turbulence noise levels can be expected were to be established. A previously developed theoretical prediction model was to be used for performing the analytical study.

The theoretical model, described in References 2 through 4, utilizes an isotropic model of the inlet turbulence, along with sudden-contraction theory, Reference 5, to account for inlet flow contraction effects. Experimental measurements, however, indicate that the initial turbulence upstream of the inlet is not isotropic, e.g., Reference 6. Additionally, it is desirable to be able to specify independently the axial and transverse turbulence intensity and length scales. Hence, the theoretical model was to be extended to include an axisymmetric initial turbulence spectrum, prior to carrying out the wind tunnel evaluation study.

The scope of the present study consisted of four primary tasks in support of achieving the above-stated objective:

Task 1 - Modification of previously-developed General Electric rotor/turbulence interaction prediction model to include anisotropic turbulence.

Task 2 - Establishment of representative turbulence properties for three acoustic test facilities or conditions: (1) Outdoor Test Stand static facility, (2) NASA-Ames 40x80 ft Wind Tunnel, and (3) Flight Test. Only existing available data is to be utilized.

Task 3 - Evaluation of rotor/turbulence noise source characteristics of a typical high speed fan for each of the facilities/conditions listed in Task 2.

Task 4 - Evaluation of the degree to which the NASA-Ames 40x80 ft Wind Tunnel simulates flight conditions from the standpoint of acceptably low rotor/turbulence interaction noise.

The following sections describe in detail the work performed in the above four tasks. A brief review of the rotor/turbulence noise theory is first given, followed by a description of the anisotropic turbulence theory modifications. The survey of inlet turbulence properties is then summarized, followed by the parametric study and wind tunnel evaluation.

3.0 REVIEW OF ROTOR/TURBULENCE NOISE THEORY

As discussed in References 2 through 4, there are several mechanisms by which inlet turbulence might produce noise. The turbulence may be regarded as a pattern of vorticity convecting with the flow whose statistical properties are known. The nonuniformity of the velocity associated with the turbulence convecting with the flow produces unsteady fluctuations in angle-of-attack on the rotor blades, leading to unsteady blade forces and, hence, noise radiation. This mechanism is usually referred to as a dipole source and is analyzed in detail in Reference 2.

Further, when the rotor is loaded, i.e., has some steady lift distribution, there is a rotor-locked asymmetric flow pattern spinning in the fan duct having a fundamental period equal to the blade spacing. This asymmetric pattern itself is an ineffective noise source for subsonic tip speeds, but its interaction with inflow turbulence leads to a quadrupole source. Insofar as Mach number dependence alone goes, the ratio of quadrupole to dipole noise should be as M^2. The quadrupole source depends on blade loading, whereas the dipole source, to first order, does not. The quadrupole mechanism is treated in detail in Reference 3.

Finally, a third mechanism, postulated in Reference 4, arises when a zero perpendicular velocity boundary condition is imposed at the blade surface for the quadrupole model problem. This mechanism is analogous to the noise increase experienced when a vibrating tuning fork is brought near a solid surface. A detailed analysis of this mechanism can be found in Reference 4.

Based on the above physical picture of noise generation due to turbulence incident on a blade row, theoretical analyses were developed (References 2 through 4) relating the characteristics of the turbulence, design parameters of the blade row, and the spectrum of the radiated noise. A spectral representation of turbulence which treats the turbulence as a superposition of shear waves was used. The turbulence was assumed to be homogeneous and isotropic. The effects of inlet contraction were subsequently accounted for (Reference 4) by utilizing the sudden-contraction theory of Reference 5, as illustrated in Figure 1.

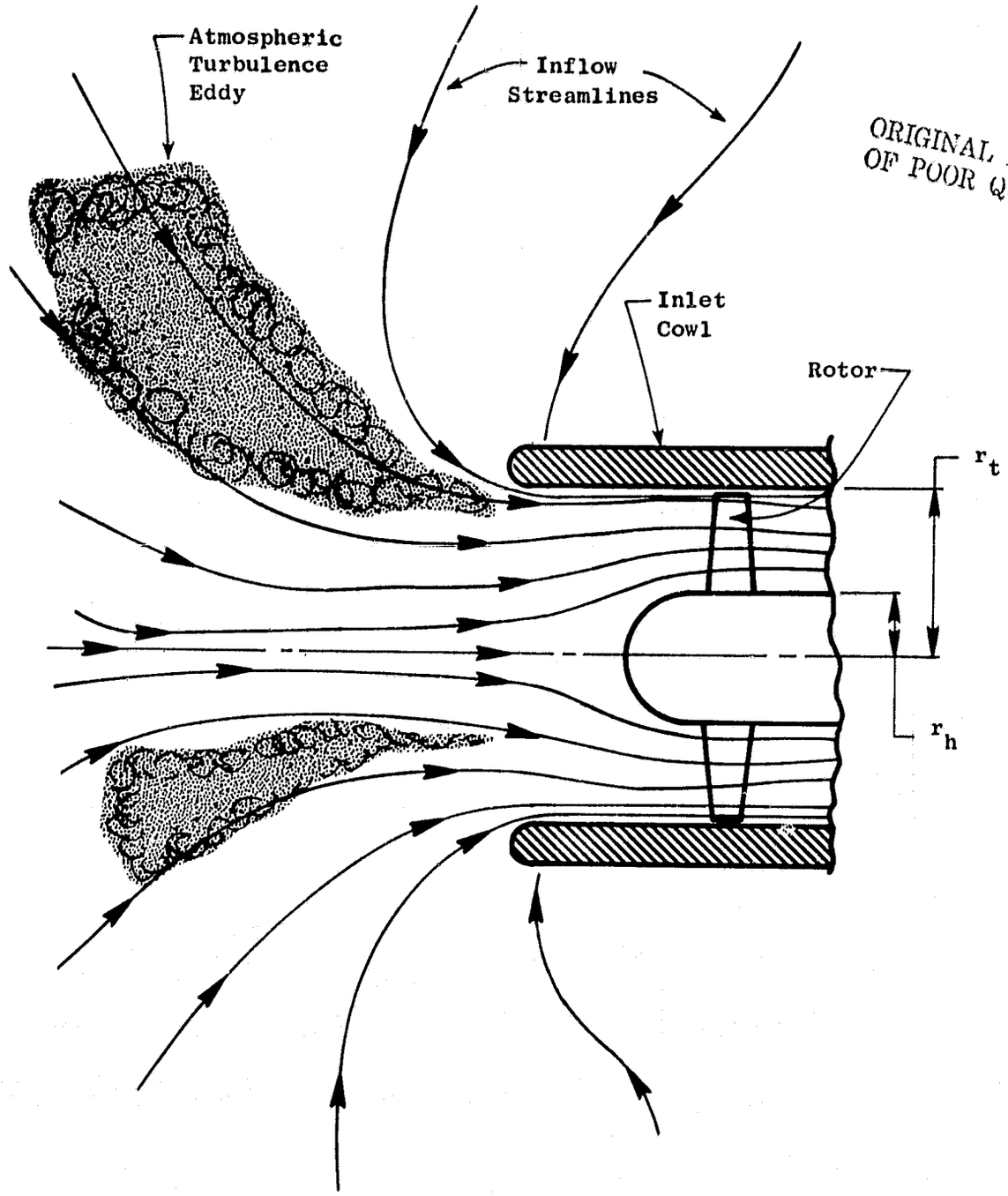

Figure 1. Fan Rotor-Turbulence Interaction and Large-Scale Turbulent Eddy Contraction.

A two-dimensional cascade representation of the blade row was employed, and the blades were idealized as flat plates. The flow was assumed to enter the inlet axially with axial Mach number M_a, while the cascade translated with transverse Mach number M_t, as illustrated in Figure 2. The turbulence was treated as a superposition of shear waves of varying wavenumber in the axial (x), transverse (y), and spanwise (z) directions.

The statistical description of the turbulence assumed determines the amplitude distribution of the velocity shear waves over the wavenumber spectrum. The x, y, and z components of the shear wave velocities are resolved into components normal to the blade chord to determine the unsteady angle-of-attack or upwash incident on the rotor blades.

For the unsteady blade force evaluation, the compressible, two-dimensional, isolated airfoil lift response functions given in References 7 and 8 are used. The low-frequency theory of Reference 7 is used for low reduced frequencies, while the asymptotic high-frequency theory of Reference 8 is used for high reduced frequencies. A correction for airfoil aspect ratio is also included, as was suggested in Reference 9.

As described in Reference 3, the steady blade-to-blade flow field locked to the rotor is modeled by representing the blades as a row of translating, equally-spaced concentrated point forces. The velocity field due to the steady blade loading is coupled with the turbulence velocity field to evaluate the resulting Reynolds stresses which are the quadrupole source strengths, analogous to the fluctuating Reynolds stresses which form the source strengths for jet mixing noise. Since the amplitude of the rotor-locked steady velocity field is proportional to the blade loading or lift coefficient C_ℓ, the quadrupole strength is also proportional to C_ℓ, and hence so is the associated acoustic pressure.

The General Electric Company computer code for the prediction of rotor/turbulence interaction noise is essentially a modified form of the code presented in Reference 3. The incompressible lift response function (Sears' function) has been replaced by the compressible response functions described above, and the contraction effects as discussed in Reference 4 have also been added.

M_t - Blade Speed Mach No.

M_a - Inflow Axial Mach No.

- Fluctuations in M_a Caused by u_a
- Fluctuations in M_t Caused by u_t
- u_a and u_t Produce Fluctuations in Flow Angle α_r

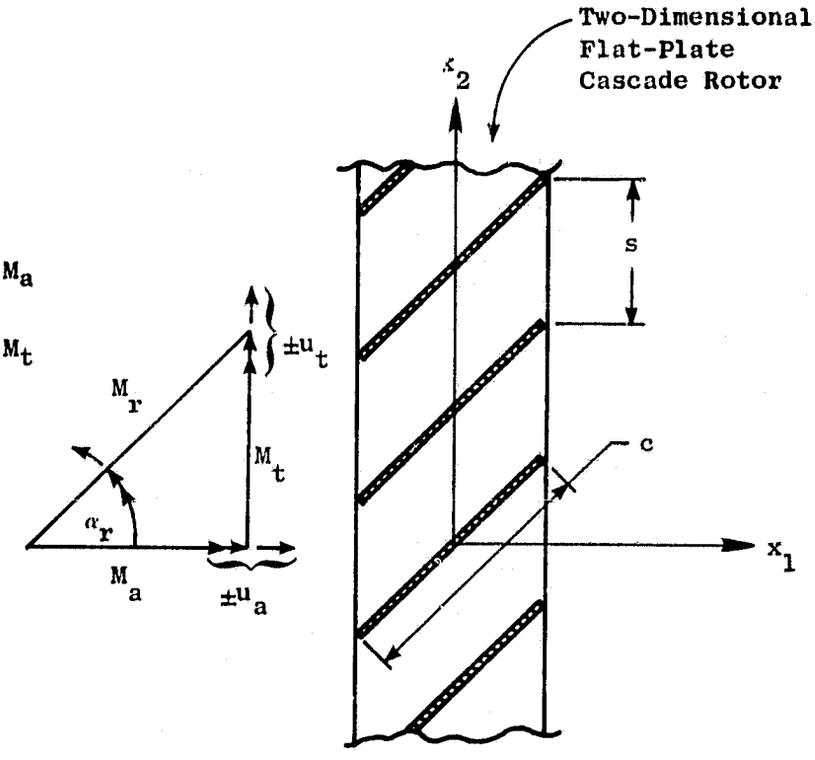

Figure 2. Rotor/Turbulence Interaction Theory Model Geometry and Nomenclature.

The quadrupole/blade interaction source mechanism (tuning fork amplification effect) has not been included, for several reasons. First, diagnostic calculations have shown this mechanism to exhibit "resonances" in its present formulation, which do not appear in the experimental data. Second, the experimental effect of blade loading (Reference 6) was very small on blade-passing frequency, indicating that the dipole source is dominant. Third, the formulation in its present form required certain arbitrary modifications in order to prevent the predicted noise level from becoming either too large or too small, and it was felt that a degree of rigor was sacrificed compared to that of the dipole and quadrupole source models. Finally, the computation time for the quadrupole/blade interaction contribution was an order-of-magnitude larger than that for both dipole and quadrupole contributions combined. In view of the uncertainties associated with this portion of the formulation, the additional expense was not considered worthwhile.

The above-described computer code prediction, prior to the present program modifications, predicts inlet and exhaust radiated power spectra (PWL) in proportional bandwidths. Input required is M_a, M_t, C , rotor solidity (defined as chord c over blade spacing s), inlet turbulence intensity, axial length scale, and inlet contraction ratio. The initial turbulence upstream of the contraction was assumed to be isotropic. Output includes dipole, quadrupole, and total PWL spectra for both inlet and exhaust ducts.

A sample prediction of rotor/turbulence noise inlet duct PWL spectrum and a corresponding measured inlet arc PWL spectrum, taken from Reference 6, is shown in Figure 3. The predicted spectrum utilizes the measured axial turbulence intensities and axial length scales reported in Reference 6, along with a contraction ratio based on the measured ratio of transverse to axial intensity and the sudden contraction relationships of Reference 5. It can be seen from this comparison that there is much room for improvement in the prediction. The basic problem lies in the isotropic turbulence assumption. The measurements of Reference 6 show a ratio of transverse turbulence intensity u_t/U_a to axial turbulence intensity u_a/U_a of about 2.0. The measured ratio of axial length scale ℓ_a to transverse length scale ℓ_t is about 300. Using isotropic turbulence followed by a sudden contraction, it is predicted that u_t/u_a is approximately the same magnitude as ℓ_a/ℓ_t, in strong contradiction to the measured evidence.

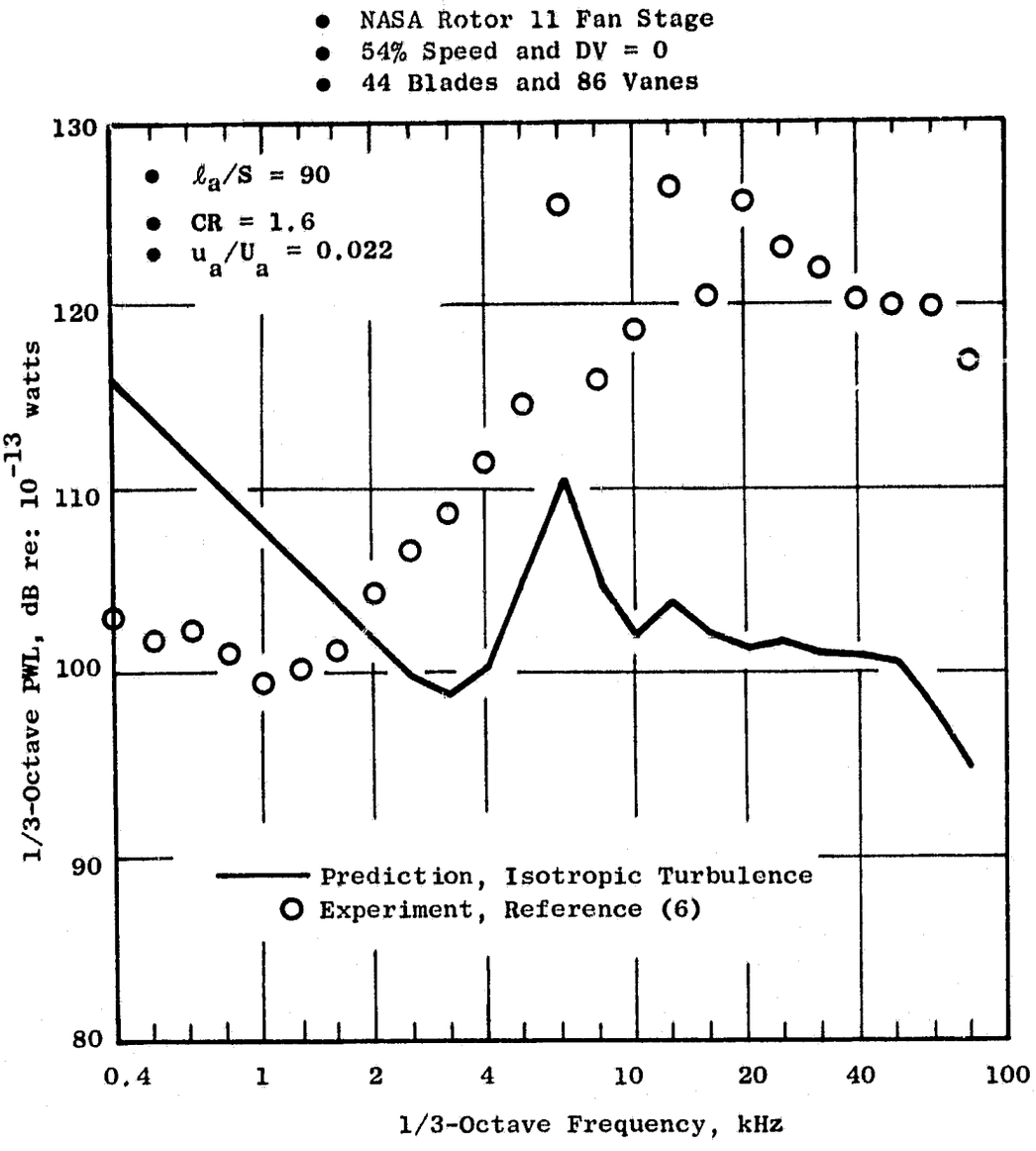

Figure 3. Comparison of Predicted and Measured Inlet Arc PWL Spectra, Isotropic Initial Turbulence with Sudden Contraction Theory.

Hence, before the proposed study outlined in the introduction could be carried out, the inlet turbulence model had to be reformulated to allow independent specification of u_a/u_t and ℓ_a/ℓ_t. Additionally, the new formulation had to be shown reasonably accurate insofar as ability to predict rotor/turbulence noise is concerned, so that reasonable confidence could be established in the parametric study trends and results of the NASA-Ames 40x80 wind tunnel evaluation. The following section describes the formulation of an anisotropic turbulence model for rotor/turbulence interaction predictions.

4.0 ANISOTROPIC TURBULENCE SPECTRUM ANALYSIS

Recognizing that the assumption of isotropic turbulence is inadequate for modeling the turbulence spectra drawn into the fan duct, the next higher order in complexity is to assume that the turbulence is axisymmetric. Axisymmetric turbulence is characterized as having one preferred axis of symmetry, whereas isotropic turbulence has none. The axis of symmetry is assumed to be parallel to but not necessarily coincident with the main axial flow direction. The time-averaged velocity fluctuations (and length-scales) normal and parallel to the axis of symmetry may be different, whereas for isotropic turbulence they are equal. Adoption of an axisymmetric turbulence model, therefore, provides the flexibility to independently specify the axial and transverse turbulence intensities, as well as differing axial and transverse length scales. Because only one axis of symmetry is assumed, the tangential and radial intensities are also assumed to be equal, as are the tangential and radial length scales.

The following development is based on the theory of Axisymmetric Turbulence given in References 10-12. The axial direction (subscript 1) is assumed to be the axis of symmetry. An effort has been made to develop the results so that they will reduce to the previously assumed case of isotropic turbulence when the proper limits are taken. The rotor/turbulence interaction model treats the rotor as a two-dimensional cascade in the axial-tangential plane, from which it follows that only the axial and tangential turbulence quantities are required. Denoting the tangential direction by subscript 2, the turbulence spectra Φ_{11}, Φ_{12}, and Φ_{22} are required as functions of wavenumber components k_1, k_2, and k_3. The corresponding velocity correlation functions are R_{11}, R_{12}, and R_{22}, which are functions of spatial separation distances x_1 (axial), x_2 (tangential), and x_3 (radial).

Chandrasekhar (Reference 11) showed that the general form of a symmetric, second-order, axisymmetric, solenoidal (divergence-free) velocity correlation tensor is as follows:

$$R_{ij} = \epsilon_{j\ell m} \frac{\partial q_{im}}{\partial x_\ell} \qquad (1)$$

where

$$q_{ij} = x_k \left[\epsilon_{ijk} Q_1 + \epsilon_{ilk} \left(\delta_{1j} Q_2 + x_j Q_3 \right) \right]$$

and

$$Q_3 = \left(\frac{\partial}{\partial x_1} - \frac{x_1}{x_3} \frac{\partial}{\partial x_3} \right) Q_1$$

and where Q_1 and Q_2 are arbitrary functions of $|x_1|$ and $x_t = \sqrt{x_2^2 + x_3^2}$. The symbol ϵ_{ijk} is the usual alternating tensor and δ_{ij} is the Kronecker delta tensor. The above result is a generalization of the isotropic result

$$R_{ij} = \frac{f-g}{r^2} x_i x_j + g \delta_{ij} \tag{2a}$$

where f and g are functions of $r = \sqrt{x_1^2 + x_2^2 + x_3^2}$

and

$$g = \frac{1}{2r} \frac{d}{dr} (r^2 f) \tag{2b}$$

Previously (References 2-4), the isotropic result had been used, with f assumed to be of the form $u^2 \exp(-r/\ell)$.

From Equations 1-3, expressions for the correlation tensors R_{11}, R_{12}, and R_{22} can be derived, as follows:

$$R_{11} = -2Q_1 - x_t \frac{\partial Q_1}{\partial x_t} \tag{3a}$$

$$R_{12} = R_{21} = x_2 \frac{\partial Q_1}{\partial x_1} \tag{3b}$$

$$\begin{aligned} R_{22} = {} & -2Q_1 - Q_2 - 2x_1 \frac{\partial Q_1}{\partial x_1} - 2 x_3 \frac{\partial Q_1}{\partial x_3} - x_3 \frac{\partial Q_2}{\partial x_3} \\ & - 2x_1 x_3 \frac{\partial^2 Q_1}{\partial x_1 \partial x_3} + x_1^2 \frac{\partial^2 Q_1}{\partial x_3^2} + x_3^2 \frac{\partial^2 Q_1}{\partial x_1^2} \end{aligned} \tag{3c}$$

Whereas the isotropic turbulence correlation tensors, Equation 2, are characterized by one function f(r), the axisymmetric turbulence correlation tensors, Equations 1 and 3, are characterized by two arbitrary functions Q_1 and Q_2 of variables $|x_1|$ and x_t.

The turbulence velocity spectra corresponding to the velocity correlation functions are given by the Fourier transform of the correlations, as follows:

$$\phi_{ij}(\underline{k}) = \frac{1}{8\pi^3} \int_{-\infty}^{\infty} R_{ij}(\underline{x}) \exp(-j\, \underline{k}\cdot\underline{x})\, d\underline{x} \qquad (4)$$

Thus, if suitable functions Q_1 and Q_2 can be found and substituted into Equation 3, relation 4 can be applied to the result to arrive at velocity spectrum functions ϕ_{11}, ϕ_{12}, and ϕ_{22}.

Certain measurable correlation functions can be derived as limiting forms of Equation 3. For example, the axial cross correlation of the axial turbulence velocity is given by

$$R_{11}(x_1,0,0) = -2Q_1(x_1,0). \qquad (5a)$$

Also, the transverse (tangential) cross correlation of the tangential turbulence velocity is given by

$$R_{22}(0,x_2,0) = -2Q_1(0,x_2) - Q_2(0,x_2) \qquad (5b)$$

It is common practice to curve-fit the measured cross-correlations of Equations 5a and 5b with functions of the type

$$R_{11}(x_1 0,0) = u_a^2 \exp(-|x_1|/\ell_a) \qquad (6a)$$

$$R_{22}(0,x_2,0) = u_t^2 \exp(-|x_2|/\ell_t) \qquad (6b)$$

where u_a and u_t are the axial and transverse intensities, and ℓ_a and ℓ_t are the axial and transverse length scales, respectively. Equation 6a can also be written as an autocorrelation by assuming Taylor's Hypothesis of frozen, convected turbulence. Thus, if the convection velocity in the axial direction is U_a, Equation 6a can be written as $u_a^2 \exp(-U_a \tau/\ell_a)$, where τ is the autocorrelation time delay.

If expressions for Q_1 and Q_2 can be found which satisfy Equations 5 and 6 in the proper limits, the above-described process for deriving ϕ_{11}, ϕ_{12}, and ϕ_{22} can be carried out. Initially, forms for Q_1 and Q_2 were assumed as follows:

$$Q_1 = -\frac{1}{2} u_a^2 \exp\left[-\left(x_1^2/\ell_a^2 + x_t^2/\ell_t^2\right)^{1/2}\right] \tag{7a}$$

$$Q_2 = \left(u_a^2 - u_t^2\right)\exp\left[-\left(x_1^2/\ell_a^2 + x_t^2/\ell_t^2\right)^{1/2}\right] \tag{7b}$$

These expressions yield the empirical forms of Equation 6 for $R_{11}(x_1,0,0)$ and $R_{22}(0,x_2,0)$ when substituted into Equation 3 and the appropriate limits are taken, per Equations 5a and 5b.

Employing the assumptions for Q_1 and Q_2 given by Equations 7a and 7b, the velocity correlation functions given by Equations 3a-c were derived, and the corresponding turbulence spectra were derived by Fourier transform of the results, per Equation 4. The details of the derivations are omitted herein for brevity, but the resulting spectrum expressions are as follows:

$$\phi_{11} = \frac{2\,\ell_a \ell_t^2 u_a^2}{\pi^2 A^6}\left(k_2^2\ell_t^2 + k_3^2\ell_t^2\right) \tag{8a}$$

$$\phi_{12} = -\frac{2\ell_a \ell_t^2 u_a^2}{\pi^2 A^6 \lambda}(k_1\ell_a)(k_2\ell_t) \tag{8b}$$

$$\phi_{22} = \frac{4\ell_a \ell_t^2 u_a^2}{\pi^2 A^6}\left\{\left[\mu^2 - 1 + \frac{\lambda^2}{2}\right](k_3\ell_t)^2 + \frac{1}{2\lambda^2}(k_1\ell_a)^2 - \frac{3}{A^2}(k_1\ell_a)^2(k_3\ell_t)^2(\lambda - 1/\lambda)^2\right\} \tag{8c}$$

where

$$A^2 = 1 + k_1^2\ell_a^2 + k_2^2\ell_t^2 + k_3^2\ell_t^2 \tag{9a}$$

$$\lambda = \ell_a/\ell_t \tag{9b}$$

$$\mu = u_t/u_a \tag{9c}$$

The rotor/turbulence noise prediction requires the integral of the spectra over the spanwise wave number k_3, defined as follows:

$$\tilde{\phi}_{ij}(k_1,k_2) = \int_{-\infty}^{\infty} \phi_{ij}(k_1,k_2,k_3)\, dk_3 \tag{10}$$

Utilizing Equations 8 and 9, application of Equation 10 yields the following relations for $\tilde{\phi}_{11}$, $\tilde{\phi}_{12}$ and $\tilde{\phi}_{22}$:

$$\tilde{\phi}_{11}(k_1,k_2) = \frac{\ell_a \ell_t u_a^2}{4\pi A_o^5}\left(3\, k_2^2\, \ell_t^2 + A_o^2\right) \tag{11a}$$

$$\tilde{\phi}_{12}(k_1,k_2) = -\frac{3\ell_t^2 u_a^2}{4\pi A_o^5}\left[(k_1\ell_a)(k_2\ell_t)\right] \tag{11b}$$

$$\tilde{\phi}_{22}(k_1,k_2) = \frac{\ell_a \ell_t u_a^2}{4\pi A_o^5}\left[3(k_1\ell_a)^2(2-\lambda^2) + A_o^2\,(2\mu^2 - 2+\lambda^2)\right] \tag{11c}$$

where

$$A_o^2 = 1 + k_1^2\ell_a^2 + k_2^2\ell_t^2 .$$

When expressions 11 were programmed and installed in the rotor/turbulence noise computer program, problems were encountered when attempting to compute cases where the axial-to-tangential turbulence length scale ratio λ was greater than ~3. The source of this difficulty was traced to negative values of $\tilde{\phi}_{22}$, which were physically unrealistic. Examination of the expression for $\tilde{\phi}_{22}$ given in Equation 11 shows that, in order to avoid negative values, we must have

$$3(k_1\ell_a)^2(2-\lambda^2) + A_o^2(2\mu^2-2+\lambda^2) > 0$$

Now for the range $0 \leq (k_1 \ell_a) \leq \infty$, the ratio $(k_1 \ell_a / A_o)^2$ varies over the range from 0 to 1. At the lower limit, the above inequality gives

$$2\mu^2 - 2 + \lambda^2 > 0$$

which holds for all λ as long as $\mu > 1$. At the upper limit, the above inequality gives

$$\mu^2 + 2 - \lambda^2 > 0$$

which only holds as long as

$$\lambda^2 < 2 + \mu^2$$

For a typical velocity ratio $\mu = 2$, the maximum allowable value of length scale ratio is thus $\lambda = 2.45$. Thus, for $\lambda > 2.45$, negative values of $\tilde{\Phi}_{22}$ should occur, explaining the computational difficulties which were encountered.

The source of this difficulty was found to be the assumed forms for Q_1 and Q_2 given by Equation 7. An additional constraint on the selection of Q_1 and Q_2 must be enforced which insures non-negative autospectra Φ_{11} and Φ_{22}.

An extensive analysis of this problem was carried out to determine the forms of the spectrum functions which are non-negative for all practical values of λ and μ. It is shown that (see Reference 12) the spectra can be expressed in the form

$$\Phi_{11}(\underline{k}) = (k_2^2 + k_3^2)\, F(\underline{k}) \tag{12a}$$

$$\Phi_{12}(\underline{k}) = -k_1 k_2\, F(\underline{k}) \tag{12b}$$

$$\Phi_{22}(\underline{k}) = (k_1^2 + k_3^2)\, F(\underline{k}) + k_3^2\, G(\underline{k}) \tag{12c}$$

where $F(\underline{k})$ and $G(\underline{k})$ are arbitrary functions of k_1^2 and $k_t^2 = k_2^2 + k_3^2$; in order for Φ_{11} and Φ_{22} to be non-negative, they must satisfy the following constraints:

$$F(\underline{k}) \geq 0 \tag{13a}$$

$$F(\underline{k}) + (k_2^2 + k_3^2)\, k^{-2}\, G(\underline{k}) \geq 0 \tag{13b}$$

Note that ϕ_{11} and ϕ_{12} given by Equation 8 can be put in the form given by Equation 12 and additionally meet the requirement $F(\underline{k}) \geq 0$. The expression for ϕ_{22} given by Equation 8 can also be put in the form given by Equation 12, but does not meet the constraints of Equation 13. Particular functional forms for $F(\underline{k})$ and $G(\underline{k})$ have been derived which satisfy inequalities 13, and they are as follows:

$$F(\underline{k}) = \frac{2\ell_a \ell_t^4 u_a^2}{\pi^2 A^6} \tag{14a}$$

$$G(\underline{k}) = F(\underline{k}) \left[2\mu^2 - 1 - 1/\lambda^2 \right] \tag{14b}$$

The above expression for $F(\underline{k})$ is identical to that implied for Equation 8, but the relation above for $G(\underline{k})$ is much simpler. If Equations 14 are substituted into Equation 12, it is easily derived that ϕ_{22} remains non-negative as long as

$$\lambda^2 \geq \frac{1}{2\mu^2} \quad \text{or} \quad \frac{\ell_a^2}{\ell_t^2} \geq \frac{1}{2} \frac{u_a^2}{u_t^2} \tag{15}$$

Since, for the rotor/turbulence interaction problem, $u_a^2 < u_t^2$ and $\ell_a > \ell_t$, the above constraint is usually always met.

To obtain the two-dimensional spectra, expressions 12 and 14 are substituted into 10, integrating over spanwise wavenumber, to obtain the following:

$$\tilde{\phi}_{11}(k_1,k_2) = \frac{\ell_a \ell_t u_a^2}{4\pi A_o^5} (3 k_2^2 \ell_t^2 + A_o^2) \tag{16a}$$

$$\tilde{\phi}_{12}(k_1,k_2) = - \frac{3\ell_t^2 u_a^2}{4\pi A_o^5} (k_1 \ell_a)(k_2 \ell_t) \tag{16b}$$

$$\tilde{\phi}_{22}(k_1,k_2) = \frac{\ell_a \ell_t u_a^2}{4\pi A_o^5} \left[3 k_1^2 \ell_a^2 (1/\lambda^2) + (2\mu^2 - 1/\lambda^2) A_o^2 \right] \tag{16c}$$

It can be seen that these expressions are the same as those previously derived, Equations 11, with the exception that a term $(2-\lambda^2)$ in $\tilde{\phi}_{22}$ of Equation 11 is now replaced by $(1/\lambda^2)$. The requirement for $\tilde{\phi}_{22}$ to be non-negative is the same as that given by Equation 15.

It may be noted in passing that the final form for $G(\underline{k})$ given herein (Equation 14) is very similar to one expression suggested by Sreenivasan, Reference 12, i.e.,

$$G(\underline{k}) = F(\underline{k}) \left[2\mu^2 - 2\right] .$$

Expressions 16 were programmed and installed in the rotor/turbulence interaction program, and diagnostic calculations of narrowband (1 Hz bandwidth) PWL were carried out for the same case (Rotor 11 at 54% speed, from Reference 6) as was shown in Figure 3. Axial and transverse length scales were parametrically varied, and results of these calculations are shown in Figures 4 through 8. Figure 4 shows the portion of the spectrum centered around blade-passing frequency (BPF), for a fixed transverse length scale of one blade spacing. Figure 5 shows the corresponding results at 2 x BPF. Note that the spectra are very peaky for axial scales $\ell_a/s \geq 50$, and that the second-harmonic spectra are broader than the fundamental spectra. The fall off in peak tone level with harmonic number (n) is shown in Figure 6. The curves have similar shapes for $\ell_a/s > 10$. The increase in tone peak level at BPF with ℓ_a/s is shown in Figure 7. Above about $\ell_a/s > 50$-70, the tone peak increases linearly with ℓ_a/s. The effect of transverse length scale variations, wtih axial scale held fixed, is shown in Figure 8. Smaller ℓ_t/s increases the peak level and makes the spectrum narrower, but the peak appears to maximize for this case at about $\ell_t/s = 0.1$.

From the results shown in Figures 4 through 8, it can be expected that, for typical values of $\ell_a/s \approx 50$-100 and $\ell_t/s \approx 0.5$-1.0, the rotor turbulence interaction will produce spectra which are very peaky around blade-passing frequency and its harmonics, and will have broadband levels which are substantially below the peaks, by as much as 40-50 dB or more. A complete spectrum for one combination of ℓ_a/s and ℓ_t/s typical of that measured in Reference 6 is shown in Figure 9. This result confirms that the expectation is correct.

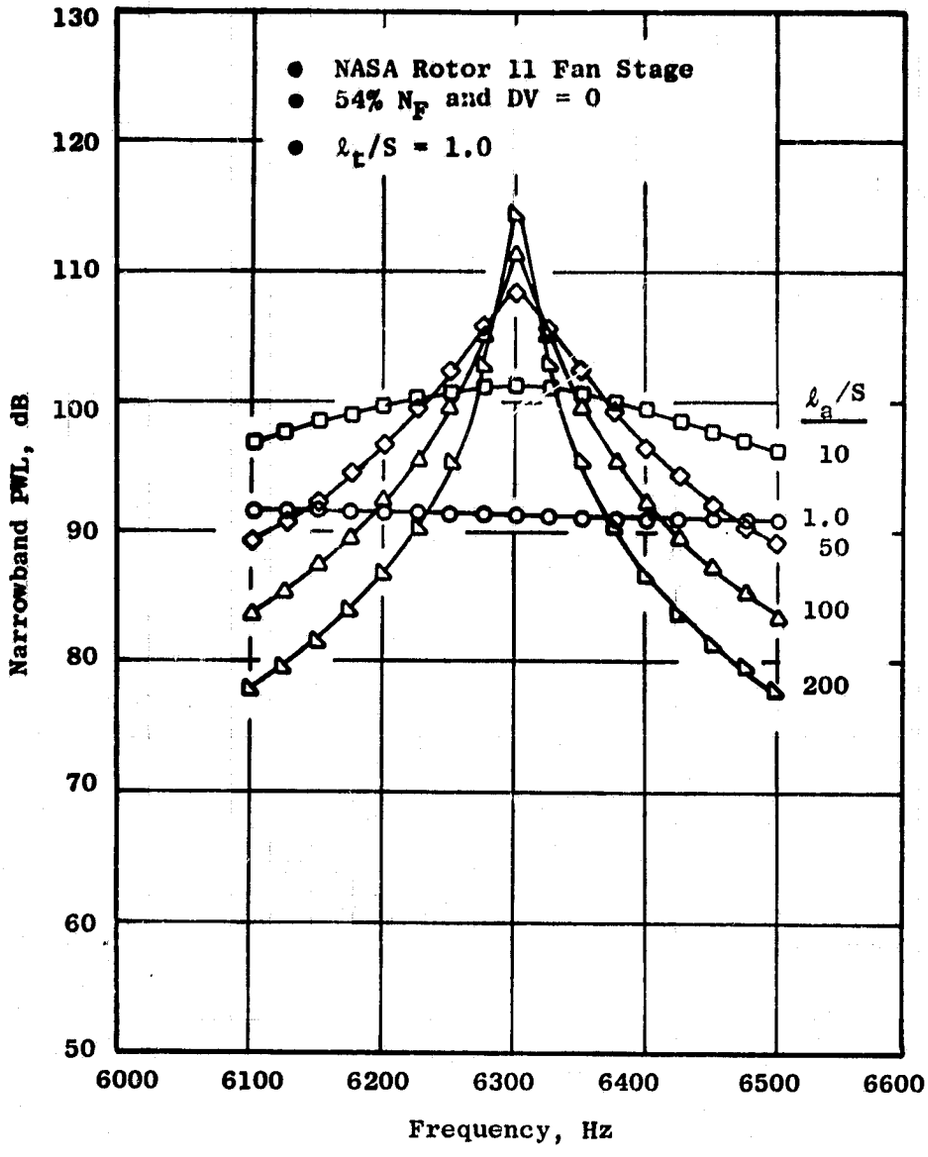

Figure 4. Narrowband Spectrum Around Blade Passing Frequency (6300 Hz) - Effect of Axial Length Scale with Axisymmetric Turbulence Spectrum Prediction.

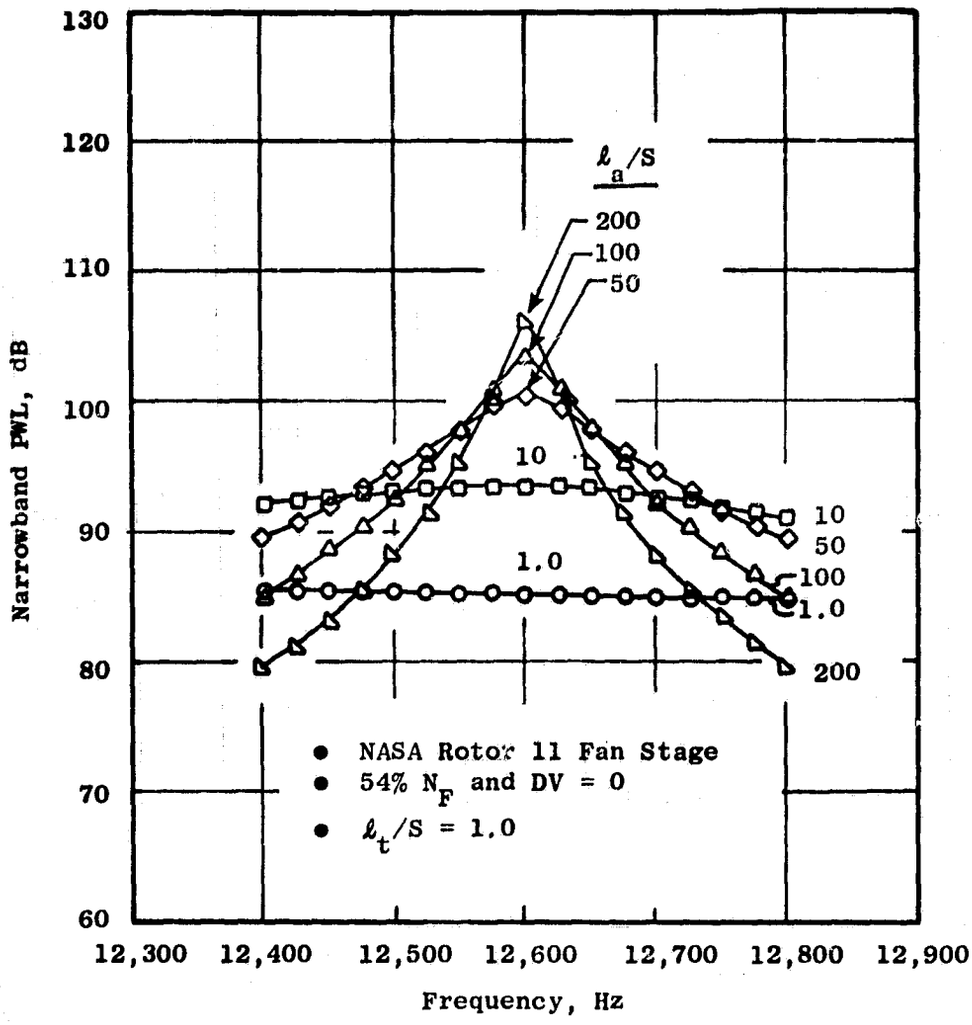

Figure 5. Narrowband Spectrum Around Second Harmonic of BPF (12,600 Hz) - Effect of Axial Length Scale with Axisymmetric Turbulence Spectrum Prediction.

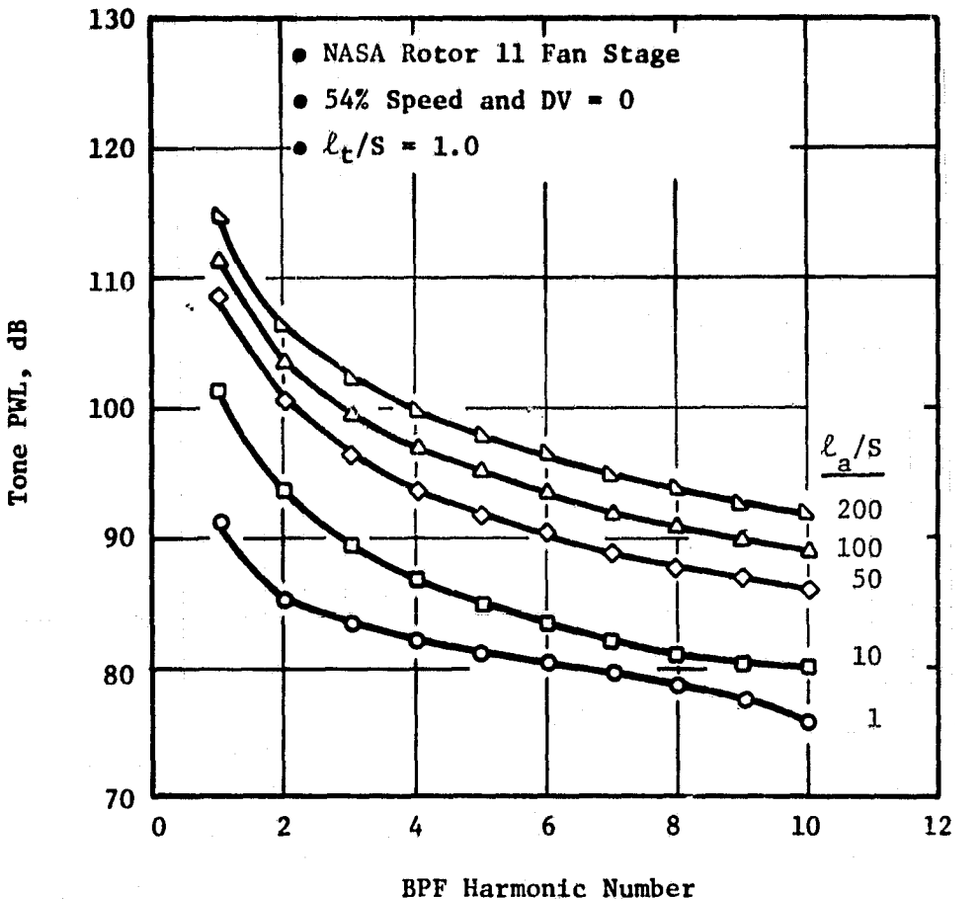

Figure 6. Effect of Axial Length Scale on Tone PWL Vs. Harmonic Number with Axisymmetric Turbulence Spectrum Prediction Model.

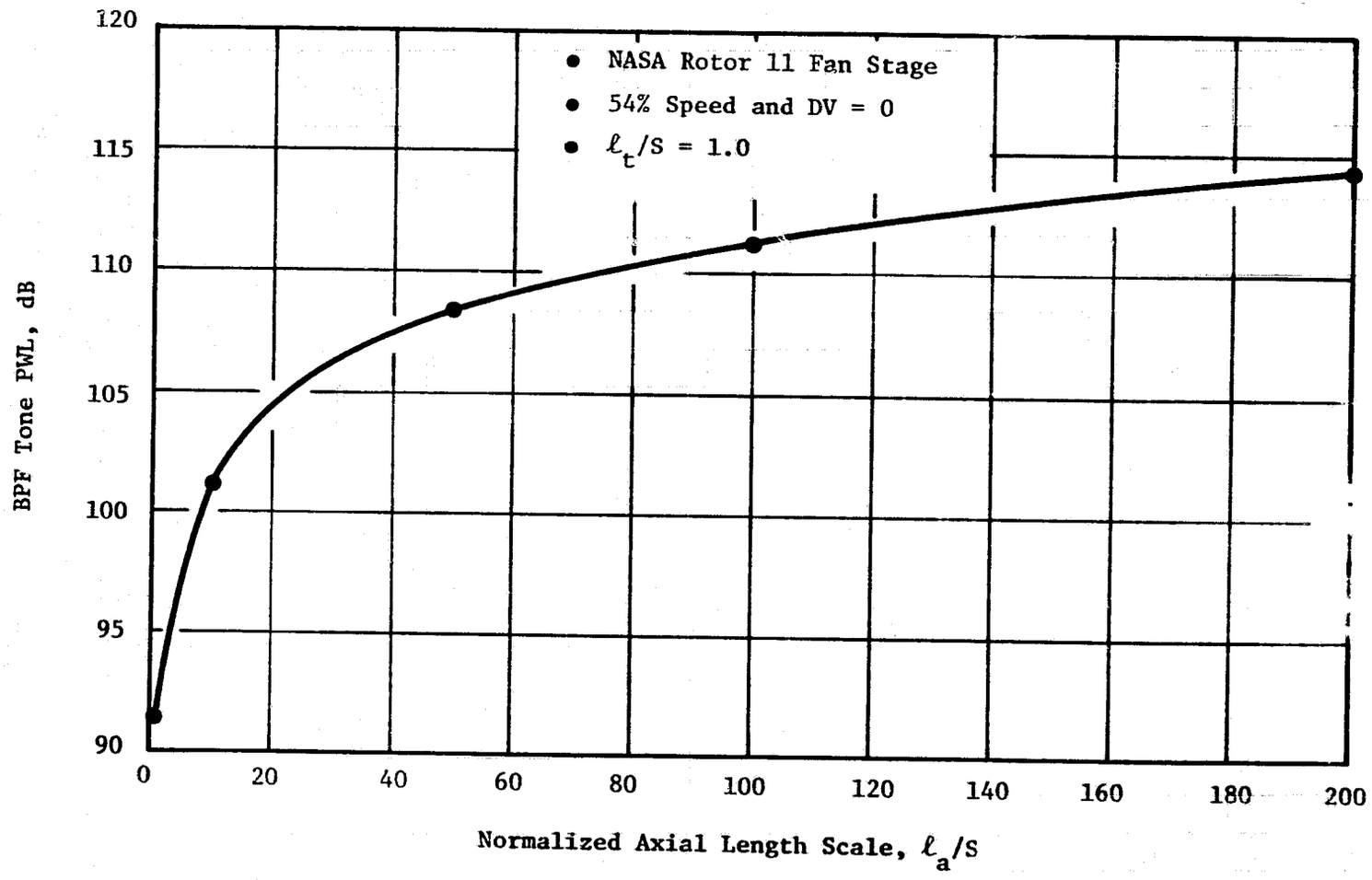

Figure 7. Effect of Axial Length Scale on BPF Tone PWL for Axisymmetric Turbulence Spectrum Model.

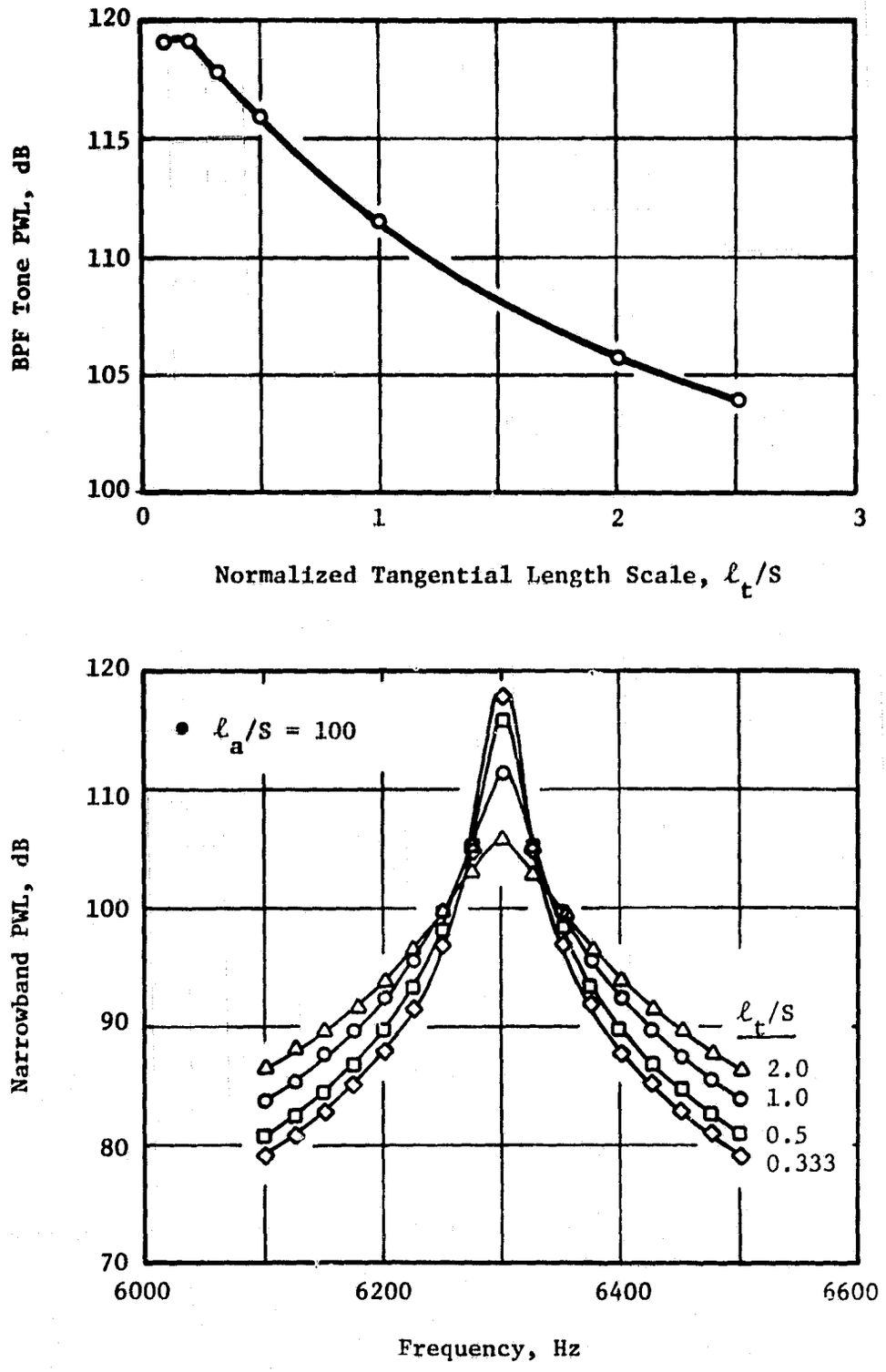

Figure 8. Effect of Tangential Length Scale on BPF Tone PWL and PWL Spectrum Around BPF (6300 Hz) - Axisymmetric Turbulence Spectrum Model Predictions.

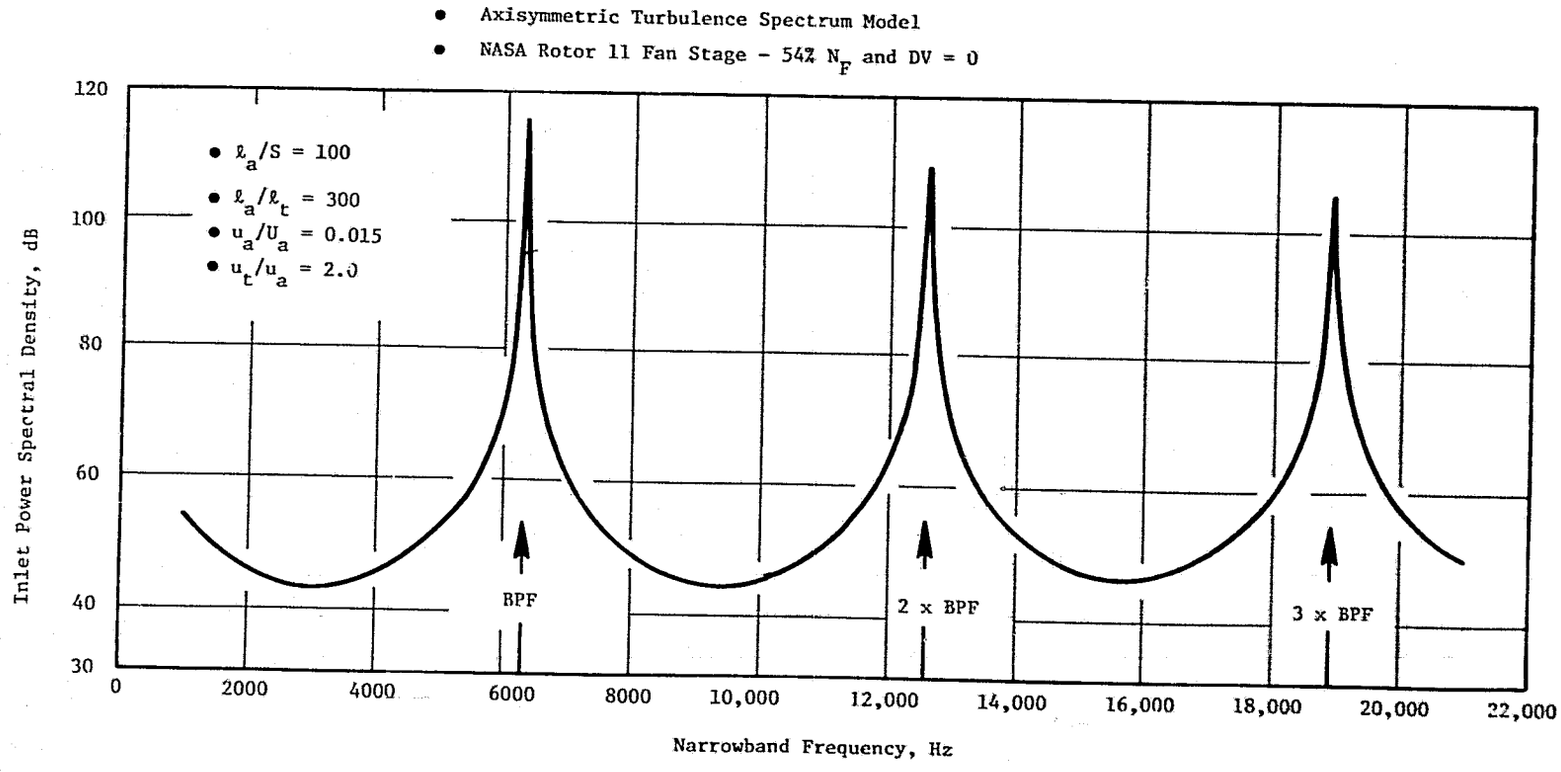

Figure 9. Prediction of Inlet Arc Power Spectral Density (1 Hz Narrowband PWL) Rotor/Turbulence Noise.

It was observed that the spectrum peaks at blade-passing frequency became higher but narrower as ℓ_a/s increased, Figure 4. It was postulated that the total tone PWL (integral over a prescribed bandwidth) might become constant above a certain value of ℓ_a/s and remain so with any further increases in ℓ_a/s. Numerical integrations were performed over a 100 Hz bandwidth around BPF and its harmonics for the results shown in Figures 4 through 8. The total PWL in a 100 Hz bandwidth does indeed level off with increasing ℓ_a/s, as the results in Figures 10 and 11 show.

Because the spectra can be so peaked for large length scales (see Figure 9), it is no longer sufficient to compute 1/3-octave levels by evaluating the center frequency level and multiplying by the appropriate bandwidth, as had been done in the past (e.g., Figure 3). The 1/3-octave levels must be evaluated by integrating the narrowband spectrum over the bandwidth. As Figure 9 shows, this involves computing many points within a given frequency band in order to obtain an accurate representation of the spectrum shape, since the spectrum drops off so rapidly on either side of the BPF harmonics. This procedure can be costly and time-consuming, and so alternate methods for evaluating 1/3-octave levels accurately were investigated.

A method was finally developed whereby the 1/3-octave levels are computed by evaluating the narrowband levels at selected points in the 1/3-octave band. The integration is performed by curve-fitting the computed points with simple mathematical functions whose integrals are available in closed form. This procedure is illustrated in Figure 12, where a BPF harmonic exists at some arbitrary location within the 1/3-octave band. Narrowband levels are computed at the peak and at both ends of the band, as shown in Figure 12a.

Considering one-half of the spectrum, e.g., $f \geq$ nxBPF, as shown in Figure 12b, the peak level is designated PWL_0 and sideband value as PWL_1. These have corresponding power values of P_0 and P_1, respectively. The sideband frequency is denoted by f_1. From the shapes of the curves shown in Figures 4 through 9, a logical choice for a curve shape is

$$P = P_0 e^{-a(f-f_0)}$$

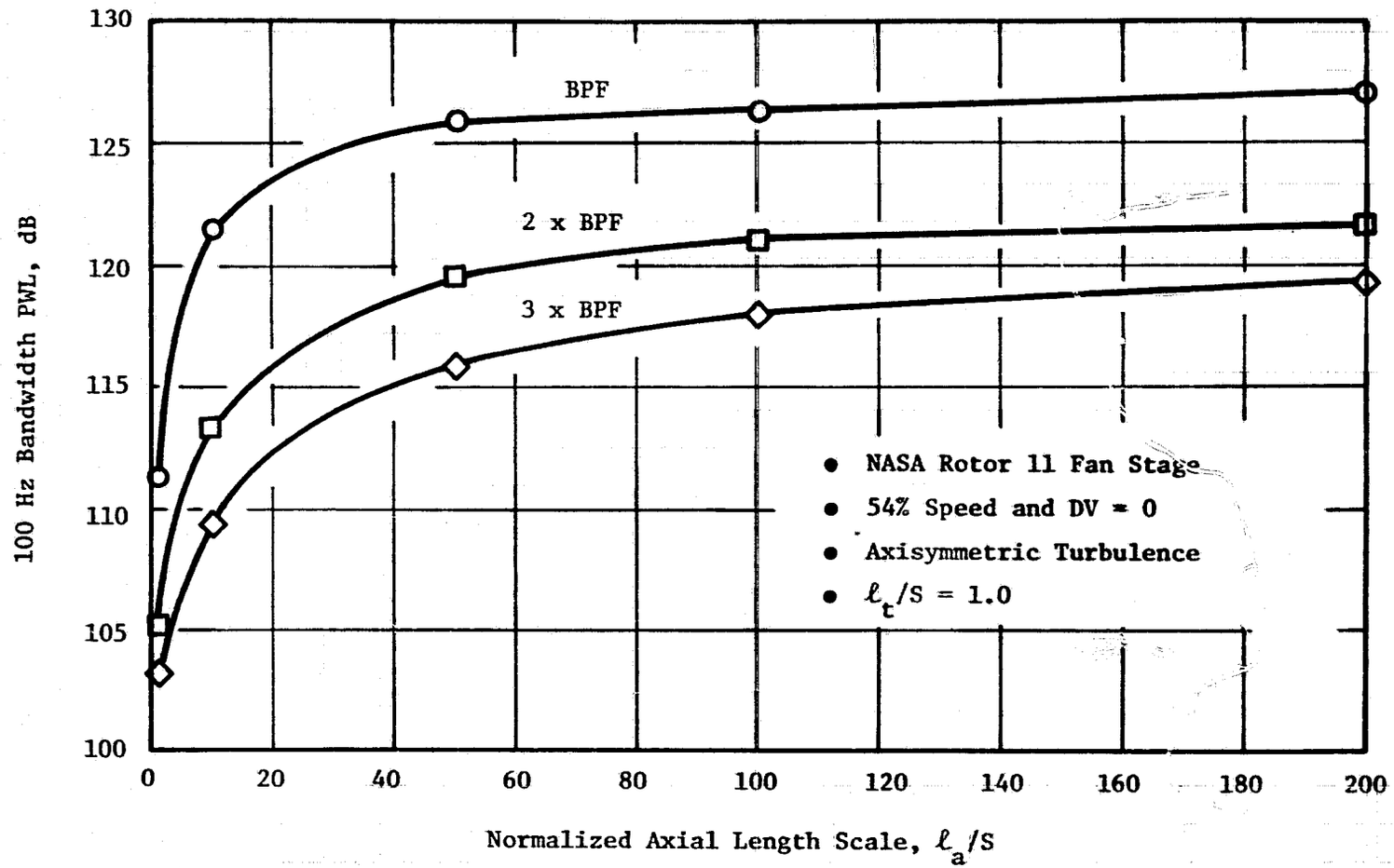

Figure 10. Predicted Effect of Axial Length Scale on Integrated 100 Hz Bandwidth Tone PWL.

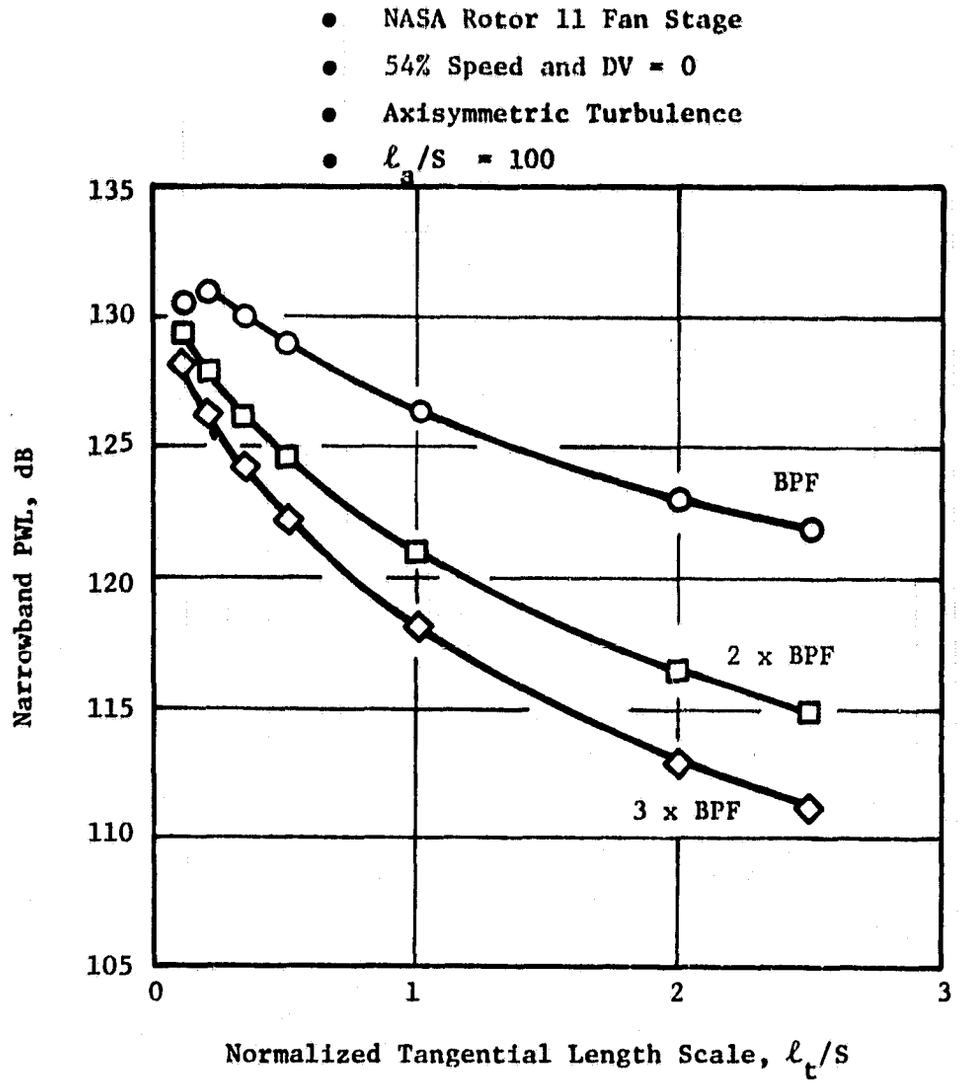

Figure 11. Predicted Effect of Tangential Length Scale on Integrated 100 Hz Bandwidth Tone PWL.

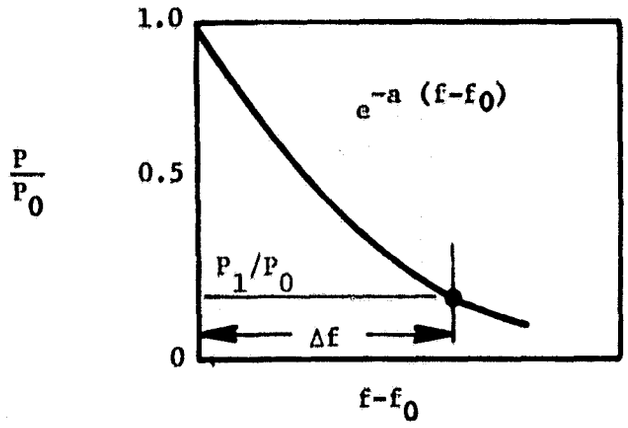

(b) Curve-Fit of Spectrum Peak

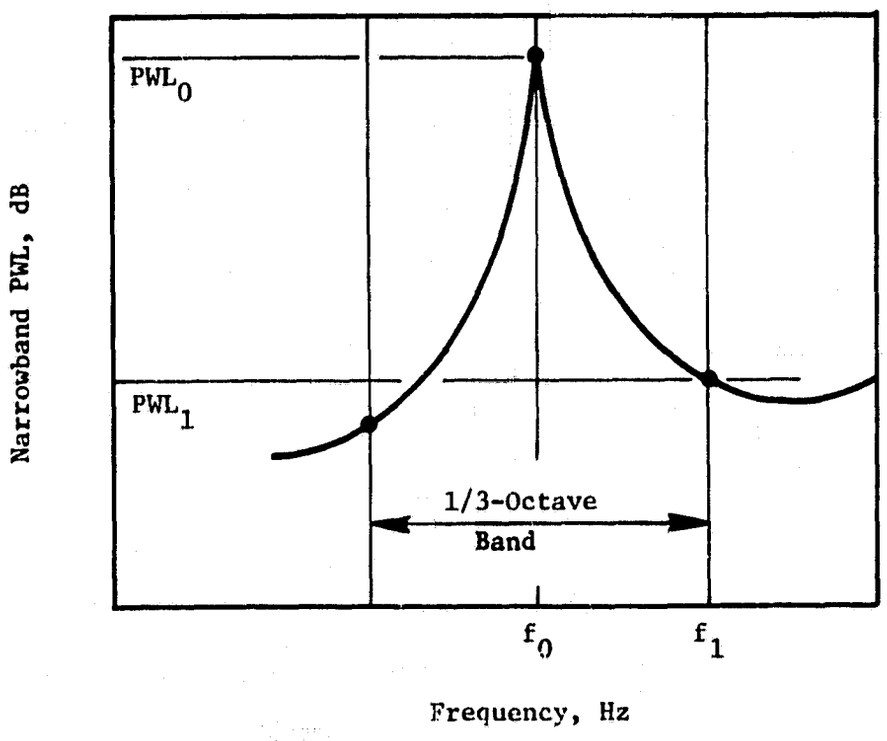

(a) Calculation Points for 1/3-Octave

Figure 12. Illustration of Method for Computing 1/3-Octave Level from Narrowband PSD.

This can be integrated over the range $\Delta f = (f_1 - f_o)$ to give

$$P_t = \frac{P_0 \, \Delta f}{\ell n(P_0/P_1)} \quad (1 - P_1/P_0) \tag{17}$$

where P_t is the total power in the interval $f_o \leq f \leq f_1$. Another logical choice for curve-fitting the spectra is

$$P = P_0/[1 + a^2(f-f_o)^2]$$

Again integrating over the interval $\Delta f = f_1 - f_o$ and evaluating the constant a from the sideband values of P and $f-f_o$, we obtain

$$P_t = \frac{P_0 \Delta f}{\sqrt{P_0/P_1 - 1}} \quad \tan^{-1} \left(\sqrt{P_o/P_1 - 1} \right) \tag{18}$$

These two expressions were compared with numerical evaluations over 100 Hz and 1/3-octave bands, and results showed that either of the above approximations 17 or 18 gave accurate results for $\Delta PWL = PWL_0 - PWL_1 < 20$-25 dB. For $\Delta PWL > 20$, it appears as though the average of 17 and 18 gives the best comparison with the precise numerical integrations. This is shown in Figure 13, where the decibel equivalents of 17 and 18 are plotted and compared with numerical integraton points. The average curve of Figure 13 is therefore used in the present computer code for evaluating 1/3-octave spectra.

The final formulations discussed above permit evaluation of rotor/turbulence interaction noise when the turbulence properties are known at the fan face (rotor leading edge plane). The turbulence properties u_a, u_t, ℓ_a, and ℓ_t can be specified independently, consistent with measured values. However, sometimes the properties may only be known upstream of the fan face at a location where the flow still undergoes a contraction prior to entering the rotor. A method for estimating the turbulence spectra for axisymmetric turbulence passing through a contraction is therefore required. The sudden contraction theory of Ribner and Tucker, Reference 5, is utilized herein.

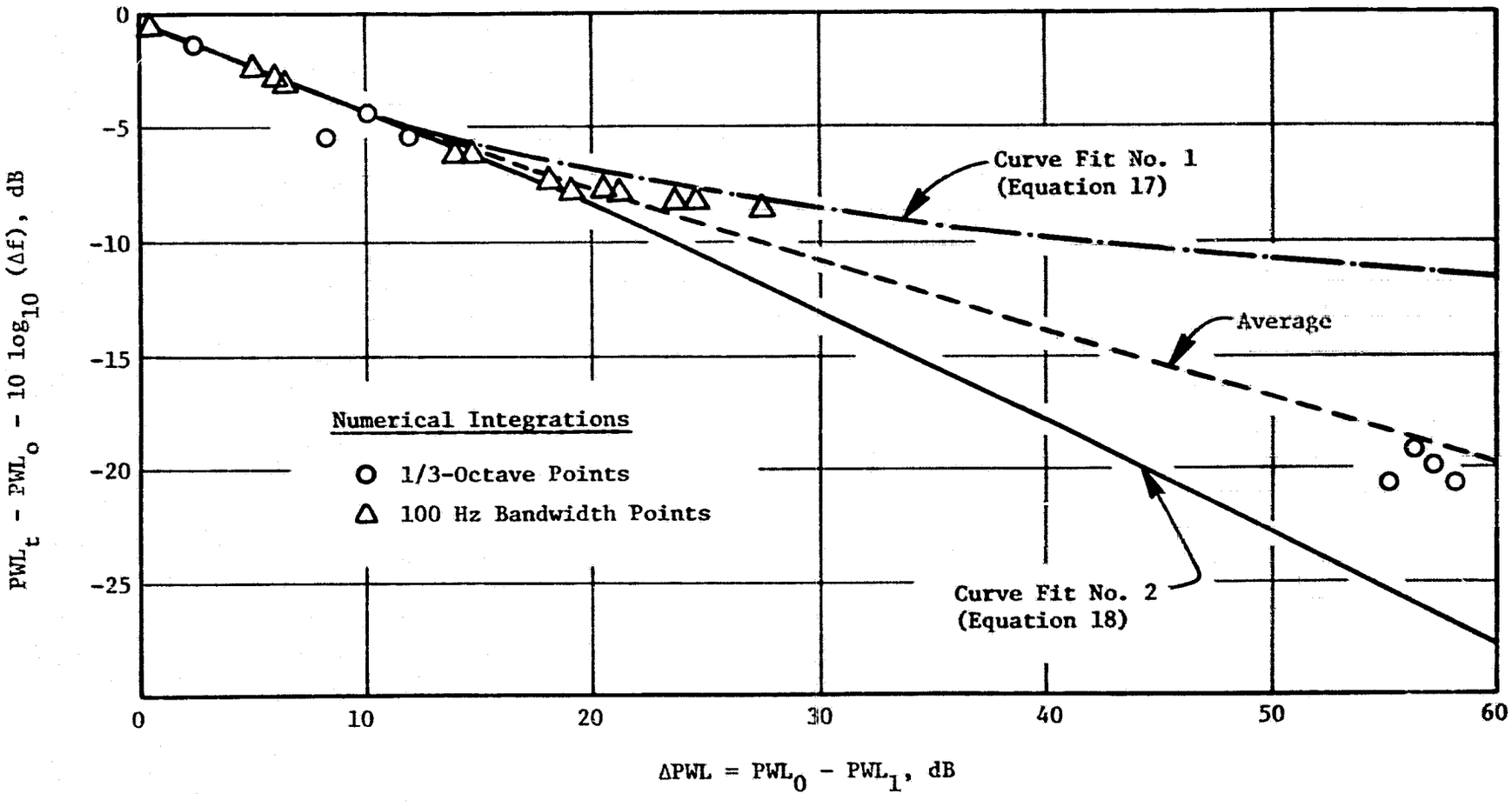

Figure 13. Comparison of Numerical Integration and Simple Curve Fit Methods for Computing 1/3-Octave PWL Spectra.

Let the postcontraction spectra and wave number be given by $\Phi_{ij}(\underline{\kappa})$, and the precontraction spectra and wave number be given by $\Phi_{ij}(\underline{k})$. Let C denote the contraction ratio, defined as the ratio of downstream-to-upstream flow velocity, and define $\epsilon = 1/C^3$. Given $\underline{\kappa} = (\kappa_1, \kappa_2, \kappa_3)$, the corresponding precontraction wave number is given by $\underline{k} = (k_1, k_2, k_3) = (C\kappa_1, \kappa_2/\sqrt{C}, \kappa_3/\sqrt{C})$. An axisymmetric contraction is assumed, as discussed in Reference 5.

Per Reference 5, the post contraction spectra are given by the following formulae, in terms of the precontraction spectra Φ_{ij}:

$$\Phi_{11}(\underline{\kappa}) = \frac{1}{C^2}\left\{ \Phi_{11}(\underline{k}) + \frac{2\Phi_{11}(\underline{k})\, k_1^2(1-\epsilon)}{\epsilon k_1^2 + k_2^2 + k_3^2} + \frac{\Phi_{11}(\underline{k})\, k_1^4 (1-\epsilon)^4}{(\epsilon k_1^2 + k_2^2 + k_3^2)^2} \right\} \tag{19}$$

$$\Phi_{12}(\underline{\kappa}) = \frac{1}{\sqrt{C}}\left\{ \Phi_{12}(\underline{k}) + \frac{[\Phi_{11}(\underline{k})\, k_2 + \Phi_{12}(\underline{k})\, k_1]\, k_1(1-\epsilon)}{\epsilon k_1^2 + k_2^2 + k_3^2} + \frac{\Phi_{11}(\underline{k})\, k_1^3\, k_2\, (1-\epsilon)^2}{(\epsilon k_1^2 + k_2^2 + k_3^2)^2} \right\} \tag{20}$$

$$\Phi_{22}(\underline{\kappa}) = C\left\{ \Phi_{22}(\underline{k}) + \frac{2\Phi_{12}(\underline{k})\, k_1 k_2(1-\epsilon)}{\epsilon k_1^2 + k_2^2 + k_3^2} + \frac{\Phi_{11}(\underline{k})\, k_1^2\, k_2^2 (1-\epsilon)^2}{(\epsilon k_1^2 + k_2^2 + k_3^2)^2} \right\} \tag{21}$$

The corresponding two-dimensional spectra, defined as the integral over κ_3 of the above three-dimensional spectra, are then given by

$$\tilde{\Phi}_{ij}(k_1,k_2) = 2\sqrt{C}\int_0^\infty \Phi_{ij}(\kappa_1,\kappa_2,\kappa_3)\,dk_3 \tag{22}$$

where $\Phi_{ij}(\underline{k})$ are assumed to be even functions of k_3 and the relation $d\kappa_3 = \sqrt{C}\,dk_3$ was used. The above integrations (Equation 22) are carried out numerically. Let

$$\ell_t k_3 = A_o \tan\theta \tag{23a}$$

$$A_o^2 = 1 + \ell_a^2 k_a^2 + \ell_t^2 k_2^2 \tag{23b}$$

then $\ell_t dk_3 = A_o \sec^2\theta d\theta$, and the factor A^{-6} in the expressions $\Phi_{ij}(\underline{k})$, Equations 12 and 14, can be written as

$$A^{-6} = \left(1 + \ell_a^2 k_1^2 + \ell_t^2 k_2^2 + \ell_t^2 k_3^2\right)^{-3}$$

$$= \left(A_o^2 + \ell_t^2 k_3^2\right)^{-3} = A_o^{-6}\sec^{-6}\theta$$

so that the integrals over k_3 can be written in the form

$$\frac{2\sqrt{C}}{\ell_t A_o^5}\int_0^{\pi/2} [\cdots\cdots]\cos^4\theta\,d\theta$$

The interval $0 \leq \theta \leq \pi/2$ is divided into 18 equal increments (5°), and Simpson's Rule is used to evaluate the interval. Equations 12 and 14 can be written in the more general form

$$\Phi_{ij}(\underline{k}) = \frac{2}{\pi^2}\,\frac{\ell_a \ell_t^2 u_a^2}{A_o^6}\,\Gamma_{ij}\cos^6\theta \tag{24}$$

where

$$\Gamma_{11} = k_2^2 \ell_t^2 + k_3^2 \ell_t^2 \tag{25a}$$

$$\Gamma_{12} = -(k_1 \ell_a)(k_2 \ell_t)/\lambda \tag{25b}$$

$$\Gamma_{22} = (k_1 \ell_a)^2/\lambda^2 + (k_3 \ell_t)^2 (2\mu^2 - 1/\lambda^2) \tag{25c}$$

Equations 19 through 25 provide all the necessary relations needed to compute the postcontraction, axisymmetric turbulence spectra.

5.0 SURVEY OF INLET TURBULENCE PROPERTIES

A literature survey of published data on fan inlet turbulence properties was carried out. A summary chart of the data reviewed is given in Table 1. The table lists the reference, vehicle, environment (test stand, chamber, wind tunnel, etc.), the approximate values (or range of values) of turbulence properties measured, and some of the important fan geometric parameters. From a review of the references listed in Table 1, an "expected ensemble average" set of turbulence properties was deduced for a typical anechoic chamber, a typical outdoor test stand, and the NASA-Ames 40x80 wind tunnel. Expected average values for in-flight conditions were derived from the results of flight test correlations of atmospheric turbulence summarized by Houbolt in Reference 25.

A table of typical expected values of inlet turbulence velocities and scales are given in Table 2. The chamber values rely heavily on the information in Reference 6, since all four quantities were measured, as well as the fan noise characteristics. Additionally, some of the earlier data was associated with peculiar facility configurations and/or had inadequate instrumentation and data acquisition equipment for measuring long length scales (see Reference 6). The outdoor test stand expected values in Table 2 are weighted heavily by the data of Hanson (References 1 and 16), as well as previously unpublished data taken on a fan engine at the General Electric Company Peebles, Ohio, test facility.

For the flight case, no fan inlet measurements of turbulence were available. However, the atmospheric turbulence properties can be used (Reference 25) along with contraction ratio corrections as outlined in the previous section. The contraction ratio is assumed to be equal to the fan face axial velocity divided by flight velocity, i.e., $C = U_a/V_o$.

The NASA-Ames 40x80 wind tunnel properties are taken from Reference 20. The measurements were made 20 feet upstream of the fan inlet, and no fan face measurements were available. In order to utilize the upstream measurements, several steps must be taken. First, both tangential and axial turbulence

Table 1. Summary of Fan Inlet Published Data.

Reference No.	Reference Principle Authors	Vehicle	Environment	ℓ_a	ℓ_t	u_a/U	u_t/U	M_a	M_t	N_B	D_t	r_h/r_t
13	Chandrashekhara	Free-running Isolated Rotor	Anechoic Chamber		1.1-1.4in. (2.8-3.6 cm)	~0.01	N/A	N/A	0.21	8,10	17 in. (43.2 cm)	0.5
14	Chandrashekhara	Free-running Isolated Rotor	Anechoic Chamber	2.5 in. (6.35 cm)	1.1 in. (2.8 cm)	~0.01	N/A	N/A	0.2-0.3	8,10	17 in. (43.2 cm)	0.5
15	Robbins and Lakshminarayana	Fan Rotor	Anechoic Chamber (Grid-Generated Turbulence)	0.21-0.4 in. (0.53-1.02 cm)	N/A N/A N/A N/A	0.005-0.02 0.02-0.035 0.025-0.035 0.03-0.038	0.02-0.03 0.045-0.08 0.050-0.09 0.075-0.095	0.13-0.18	0.11-0.15	17	6.90 in. (17.53 cm)	0.482
1, 16	Hanson	21 in. (53.34 cm) Dia. Inlet Cowl (No Rotor)	Outdoor Test Stand	34-143 ft (10.36-43.59 meters)	4-5 in. (10-13 cm)	~0.01-0.017	0.03-0.046	~0.2	N/A	--	21 in. (53.3 cm)	0.428
17, 18	Lakshminarayana	Rotor (Fan)	Anechoic Chamber	26.8-46 in. (68-117 cm) and 1.9-4.7 in. (5-12 cm)	1.4-9.17 in. (3.6-23.3 cm) and 0.02-0.07 in. (0.05-0.17 cm)	~0.025	~0.007	~0.11	~0.15	10,17	6.90 in. (17.53 cm)	0.482
19	Hodder	Scale Model Fan Rotor	Anechoic Chamber CL = "Clean" HC = "Honeycomb"	68 in. (CL) (172 cm) 1.4 in. (HC) (3.7 cm)	N/A	0.0074 (CL) 0.0170 (HC)	N/A	~0.2	~0.34	15	11.9 in. (30 cm)	0.48
20	Hodder	JT15D-1 (P&W) Engine	NASA-Ames 40-80 ft Wind Tunnel (Measurements Made 20 ft Upstream of Engine Inlet)	0.7-4.2 ft (0.21-1.28m)	N/A	0.0015-0.002	0.005-0.006	N/A	N/A	N/A	N/A	N/A

Table 1. Summary of Fan Inlet Published Data (Concluded).

Reference		Vechicle	Environment	ℓ_a	ℓ_t	u_a/U	u_t/U	M_a	M_t	N_B	D_t	r_h/r_t
No.	Principle Authors											
21	Shaw, Woodward Glaser, Dastoli	Scale Model Fan Stage	NASA-Lewis 9x15 Anechoic Wind Tunnel Static - $V_\infty = 0$ Flight - V_∞ = 41 m/s	5-7 m st 3-5 m flt	N/A	.005 st .010 flt	0.05 st 0.01 flt.	N/A	0.38-0.72	15	20 in. (50.8 cm)	0.46
22	Woodward, et al.	Scale Model Fan Stage	NASA - Lewis Anechoic Chamber, with and without Turb. Control Device	1-3 m (w) 3.5-9 m (w/o)	N/A	0.005 (w) 0.005 (w/o)	0.002 (w) 0.015 (w/o)	N/A	0.99	53	20 in. (50.8 cm)	N/A
23	Bekofske, Shaw and Wang	Scale Model Fan Stage	GE-CRD Anechoic Chamber	23-49 ft (7-15 m)	~2 ft (~0.6 m)	0.022-0.026	0.01-0.02	0.35	0.87	44	20 in. (50.8 cm)	0.5
6	Kantola and Warren	Scale Model Fan Stage	GE-CRD Anechoic Chamber	3-18 ft (1-6 m)	0.47 in. (.0.012 m)			0.28	0.68	44	20 in. (50.8 cm)	0.5
24	Hodder	Scale Model Fan Stage	NASA Ames 7x10 Wind Tunnel	0.8-3 m	---	---	0.0044	N/A	0.3	15	0.3 m	0.48

Table 2. Summary of Average Expected Inlet Turbulence Properties for Turbofan Engine Test Facilities.

Parameter	Anechoic Chamber (Static)	Outdoor Test Stand (Static)	Wind Tunnel (NASA-Ames 40 ft x 80 ft)		Aircraft Installation (V_o = 300 fps)	
			V_o = 66 fps	V_o = 265 fps	h = 200 ft	1000 ft
u_a/U_a, %	1.0 - 1.5	0.5 - 1.7	0.1 - 0.2	0.1 - 0.2	1.0 - 1.3	1.0 - 1.3
u_t/U_a, %	3.0 - 6.0	3.0 - 5.0	0.5 - 0.6	0.5 - 0.6	1.0 - 1.3	1.0 - 1.3
ℓ_a, ft.	5 - 20	85 - 250	∿1.0	∿4.0	∿300	∿700
ℓ_t, ft.	∿0.04	∿0.4	N/A	N/A	∿300	∿700
CR*	1.0	1.0	∿5.0	∿1.25	1.0	1.0

* CR = Contraction ratio from location of turbulence measurements to fan face for an average fan-face velocity of 300 ft/sec.

velocities are given, but only axial length scale was measured. Hence, the transverse length scale must be deduced from the ratio of tangential to axial turbulence velocity and the sudden contraction theory of Reference 5. This amounts to assuming that somewhere upstream of the measurement point the turbulence was isotropic, and that the eddy elongation and cross section contraction correspond to the measured velocity ratio. Second, the turbulence at the measuring point is assumed to undergo another "sudden" contraction from the measuring point to the fan face, and the relations developed in the previous section are used to compute the fan face spectra from the measuring point spectra. The contraction ratio in this case is assumed to be the ratio of fan face velocity to tunnel velocity, i.e., $C = U_a/V_o$.

6.0 DATA/THEORY COMPARISONS

Having developed an axisymmetric turbulence spectrum model, extensive data/theory comparisons were carried out to verify that the new prediction model gave reasonably accurate predictions of rotor/turbulence interaction noise. The data of Reference 6 were first compared, since it contained measurements of both turbulence properties and farfield acoustic spectra. The fan stage, a 0.508 m (20 in.) diameter fan with 44 rotor blades and 86 stator vanes, was tested with and without a honeycomb/screen turbulence control structure around the fan inlet. The purpose of the control structure was to suppress the incoming turbulence and eliminate the rotor/turbulence noise. For the purpose of this study, however, the control structure produced a different type of turbulence at the fan face and hence a different rotor/turbulence interaction. It is of interest to see if the prediction model correctly predicts the effects of the control structure.

The noise predictions were made using the rotor blade geometric properties and mean flow conditions at the root-mean-square radius of the inlet annulus, i.e., at a "pitchline" radius given by

$$r_p = \sqrt{(r_t^2 + r_h^2)/2}$$

The lift coefficient (used to determine the quadrupole strength) was evaluated based on incidence angle at the pitchline r_p, rather than from pressure ratio (Reference 3), since it was felt that leading edge loading was the primary influence on forward-radiated noise. The quadrupole portion of the prediction model has a singularity at $M_r = 1$, where M_r is the rotor inlet relative Mach number,

$$M_r = \sqrt{M_a^2 + M_t^2}$$

Therefore, predictions had to be limited to those speeds for which $M_r < 1$. The design tip speed for this fan is $U_t = 427$ m/s (1400 fps), so comparisons were limited to speeds less than 86% of design. Actually, the quadrupole prediction model is based on linear flow theory which is not valid in the transonic regime, so accurate results should not be expected for $M_r > 0.9$, which corresponds to 78-80% speed.

Computed and measured 1/3-octave spectra are shown in Figures 14 through 18 for the NASA Rotor 11 fan stage described above, without the turbulence control structure (TCS) in place. Corresponding spectra with the control structure in place are shown in Figures 19 through 22. A summary of the data/theory comparisons made is listed in Table 3. Only inlet quadrant PWL spectra are shown.

Considering first Figure 14a, which is the same case shown in Figure 3 (using the isotropic turbulence model), it can be seen that the prediction of blade-passing frequency tones and harmonics is in good agreement with the data for the new axisymmetric turbulence formulation. The results are a tremendous improvement over the isotropic predictions of Figure 3. Note also that the broadband rotor/turbulence levels are substantially below the measured levels, as would be expected from the narrowband prediction shown in Figure 9.

The blade-passing frequency for the case shown in Figure 14a is approximately 6300 Hz, and a BPF harmonic is predicted to occur in every 1/3-octave band above 20,000 Hz. The predicted levels above 20,000 Hz are in good agreement with the measured levels, although the predictions do not contain air attenuation effects. This would tend to lower the predictions at the high frequencies, by as much as 11 dB at 80 KHz. Examination of narrowband measured spectra (e.g., Figure 48a of Reference 6) shows that the BPF harmonic tones dominate their 1/3-octave band up to the 5th harmonic. Beyond n=5, the broadband noise dominates the 1/3-octave band, and this is consistent with the predicted curve of Figure 14a if air attenuation effects were to be accounted for. Similar remarks apply to the other speeds and discharge valve (DV) settings shown in Figures 14 through 18.

It is observed that the theory overpredicts the noise at high frequencies at 74% speed, where the relative Mach number is rather high, $M_r \approx 0.85$ at the pitchline. At 80% speed, the overprediction worsens, and $M_r \geq 0.9$ for this speed.

Considering now the cases with the TCS in place, Figures 19 through 22, a comparison of the measured average fan face turbulence properties with and without the TCS is shown in Table 4. These values represent approximate

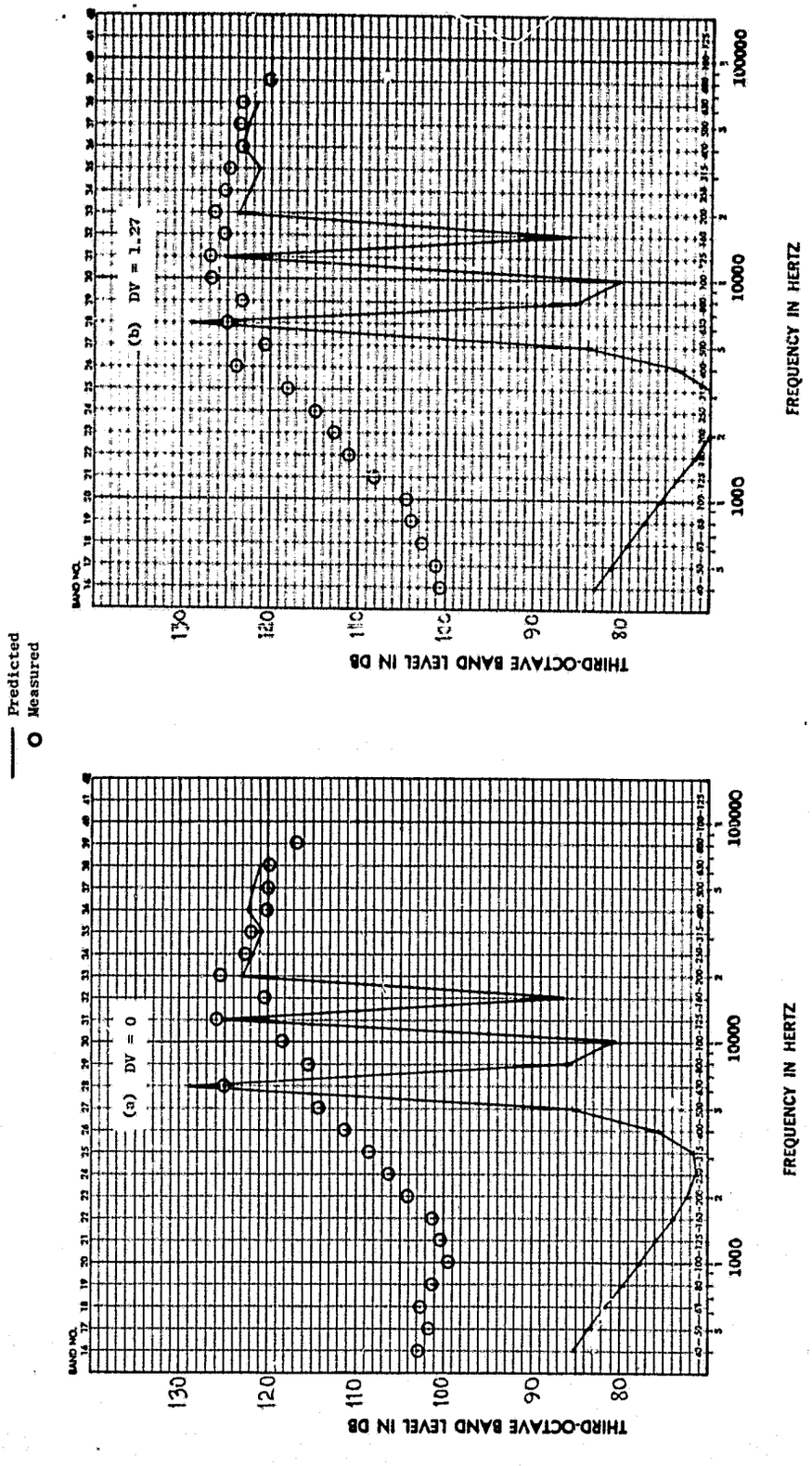

Figure 14. Comparison of Predicted and Measured Inlet PWL Spectra for Rotor 11 Fan Stage without TCS at 54% Speed.

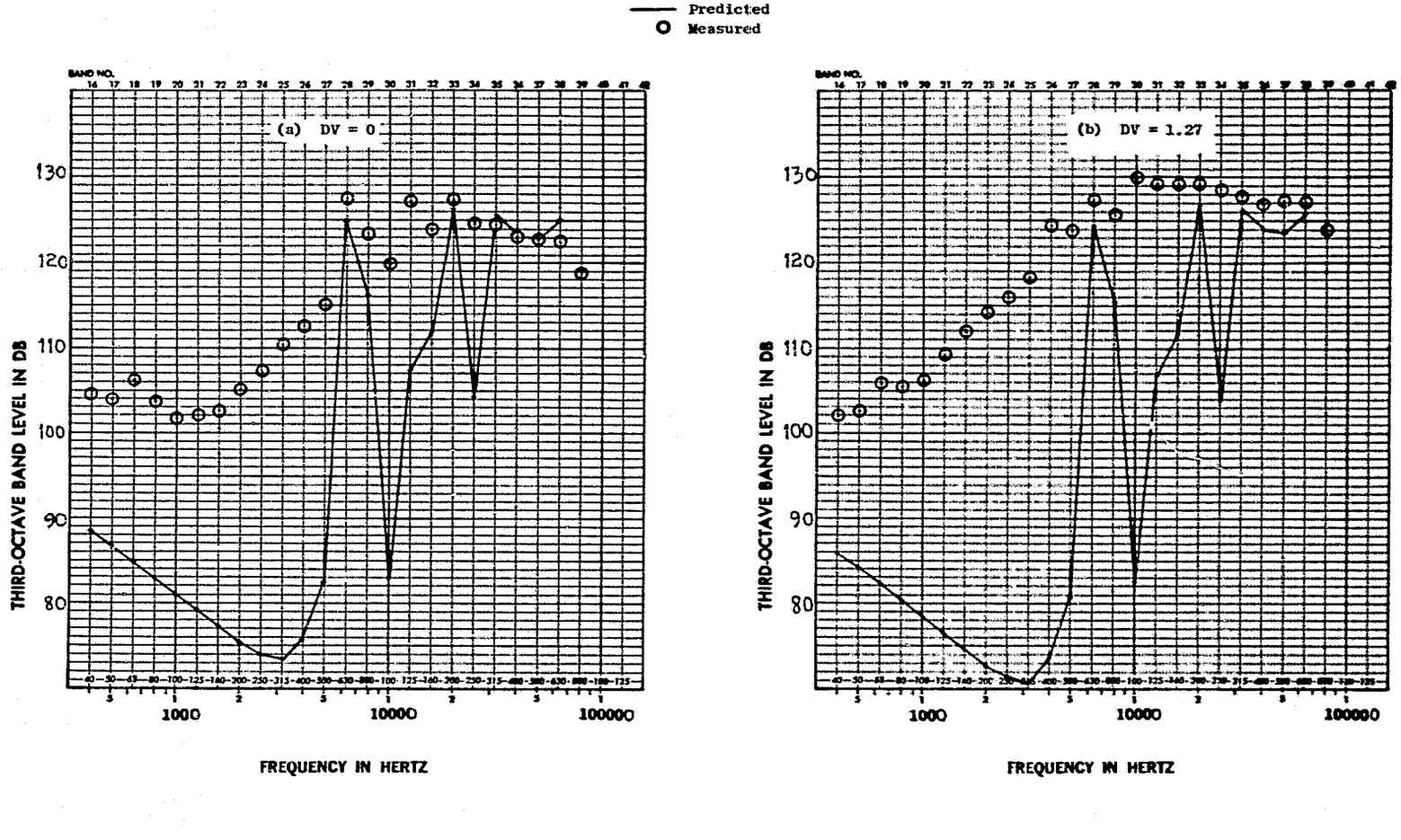

Figure 15. Comparison of Predicted and Measured Inlet PWL Spectra for Rotor 11 Fan Stage without TCS at 60% Speed.

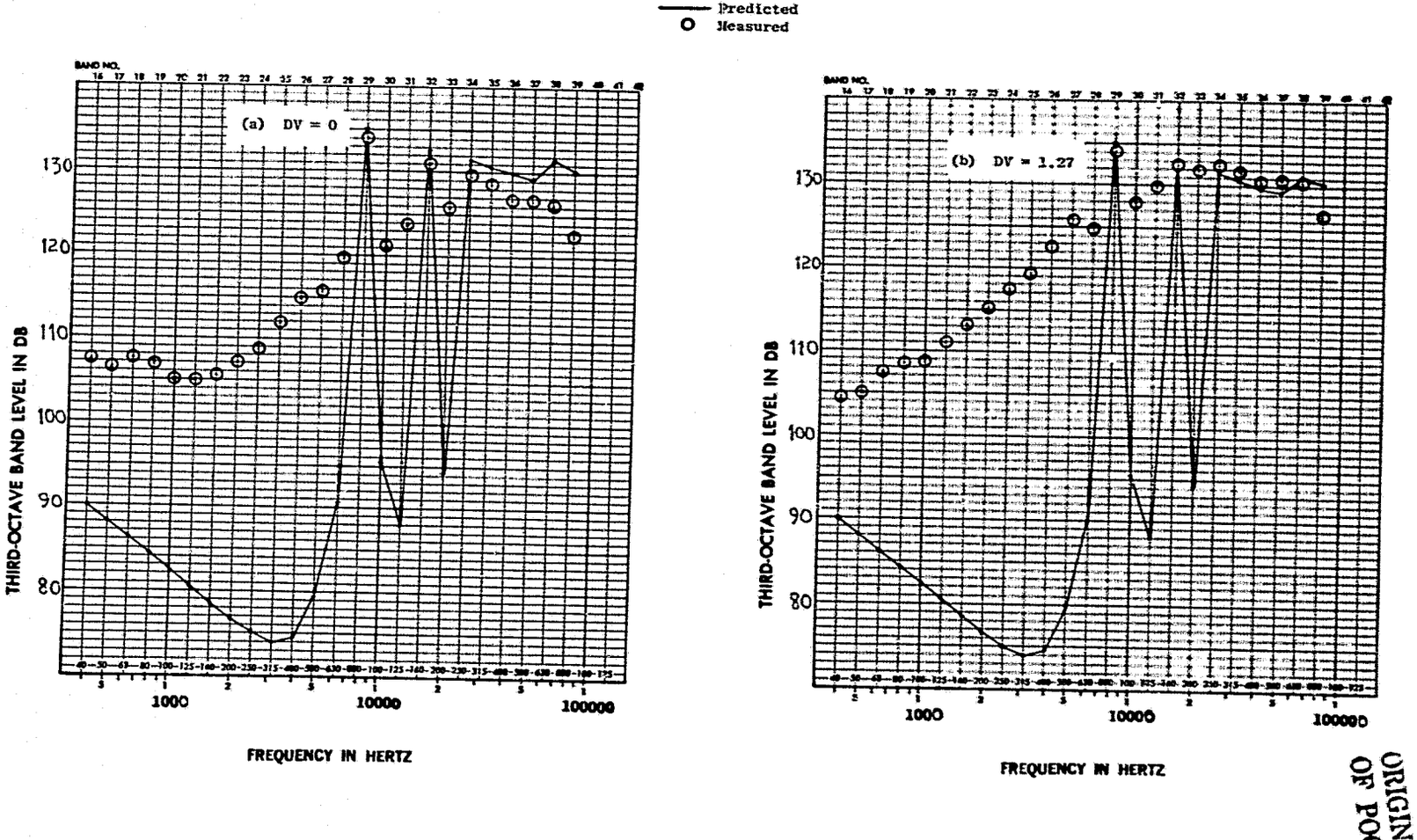

Figure 16. Comparison of Predicted and Measured Inlet PWL Spectra for Rotor 11 Fan Stage without TCS at 69% Speed.

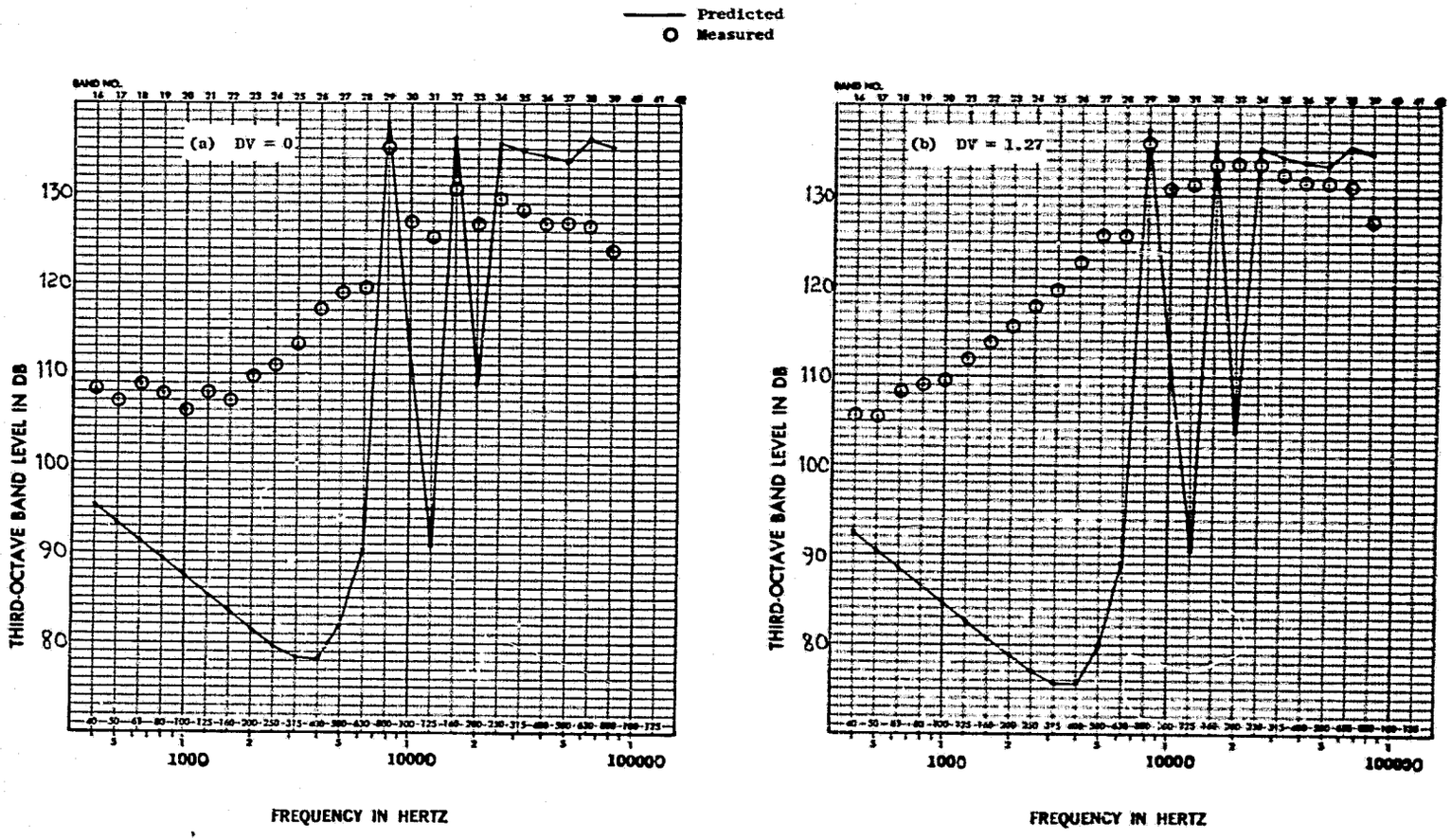

Figure 17. Comparison of Predicted and Measured Inlet PWL Spectra for NASA Rotor 11 Fan Stage without TCS at 74% Speed.

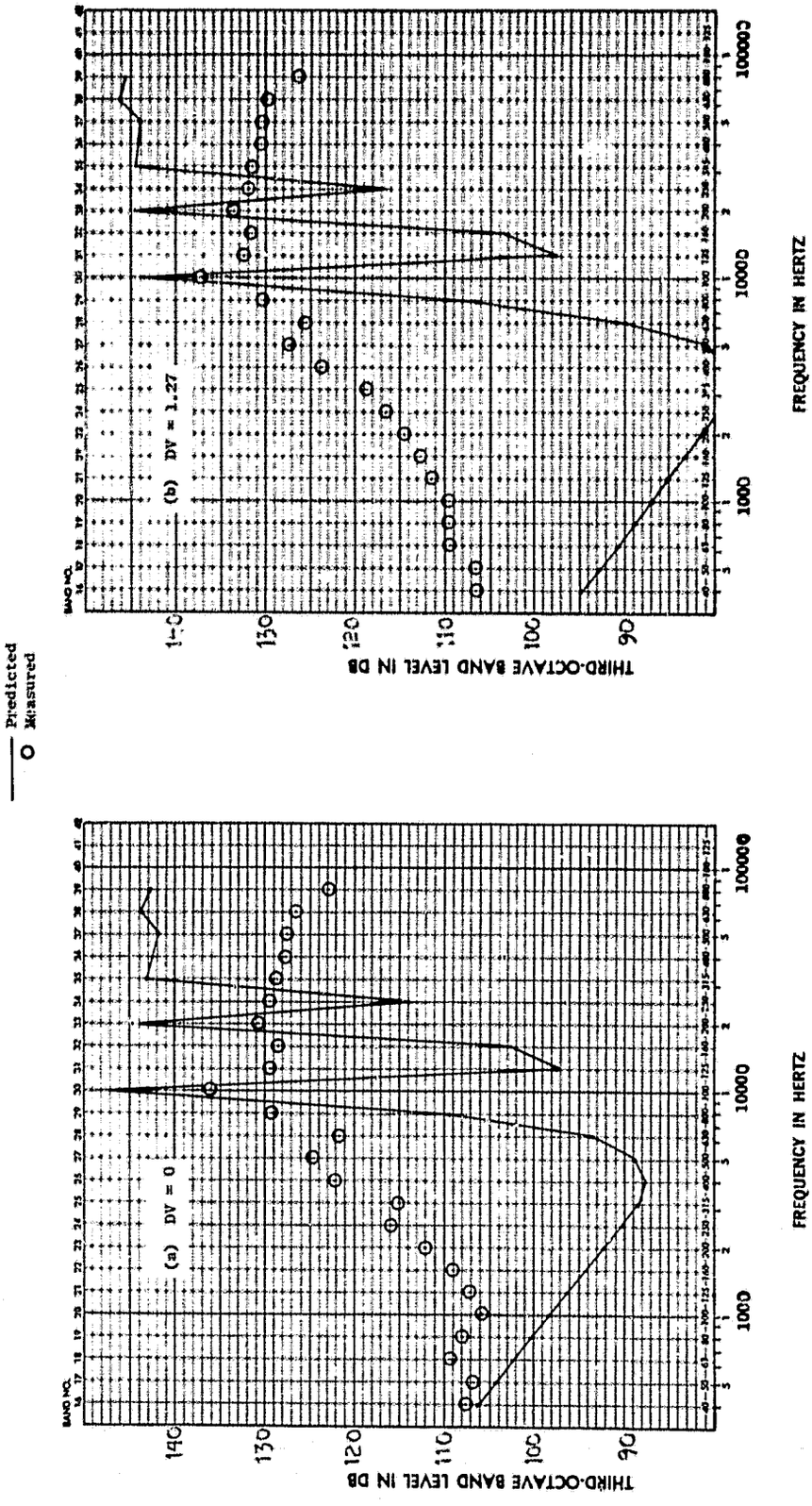

Figure 18. Comparison of Predicted and Measured Inlet PWL Spectra for NASA Rotor 11 Fan Stage without TCS at 80% Speed.

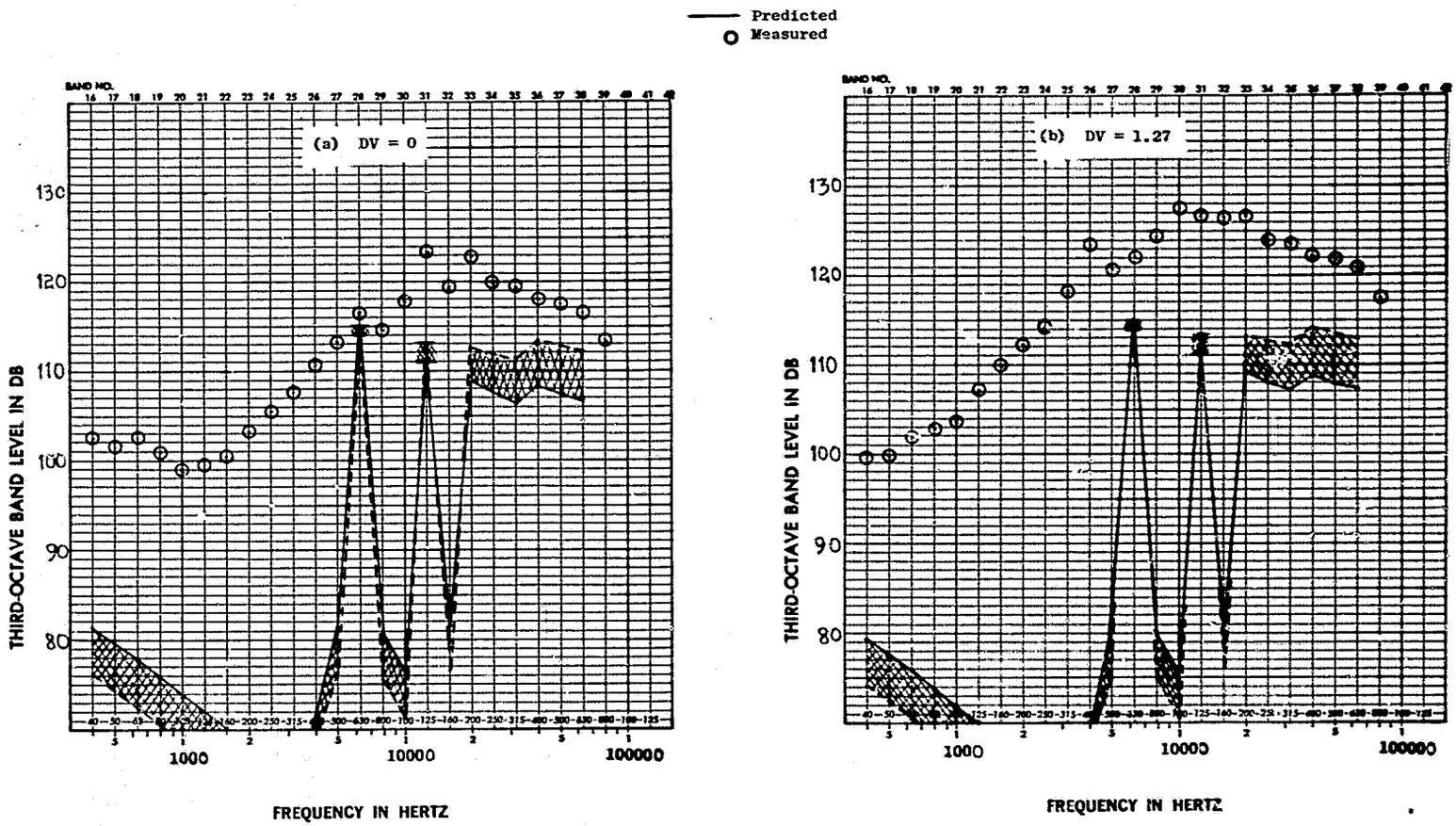

Figure 19. Comparison of Predicted and Measured Inlet PWL Spectra for NASA Rotor 11 Fan Stage with TCS at 54% Speed.

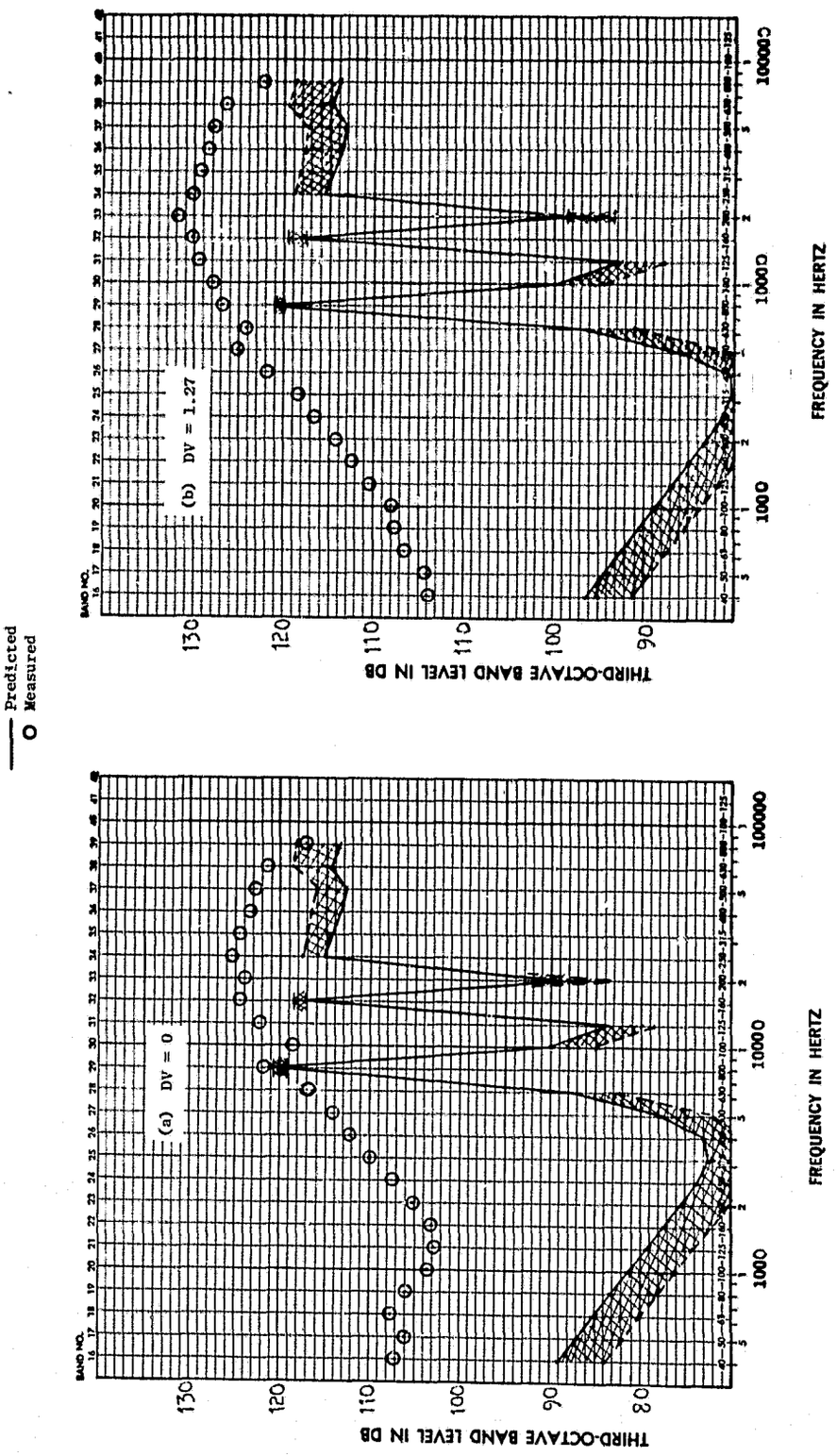

Figure 20. Comparison of Predicted and Measured Inlet PWL Spectra for NASA Rotor 11 Fan Stage with TCS at 69% Speed.

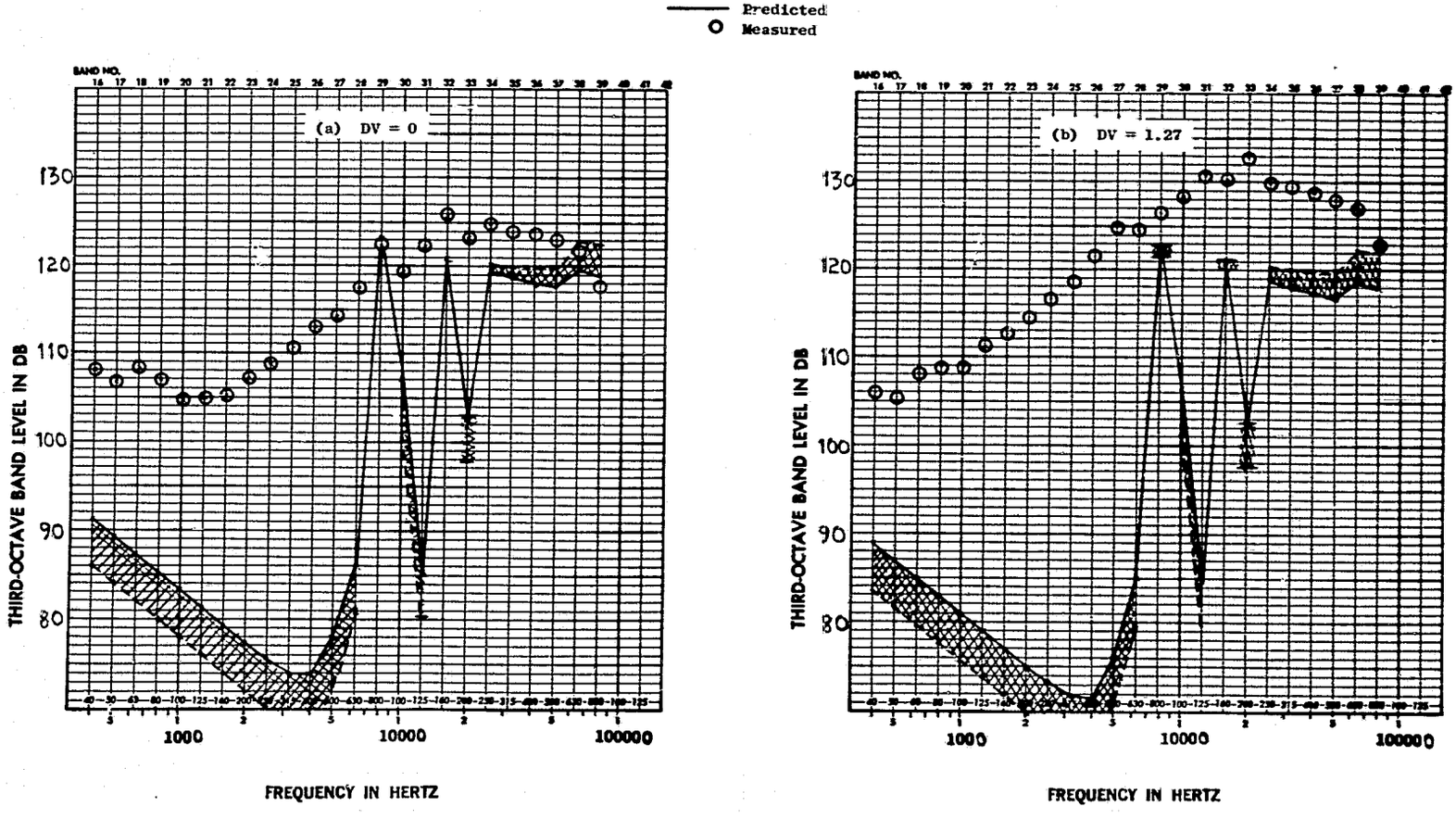

Figure 21. Comparison of Predicted and Measured Inlet PWL Spectra for NASA Rotor 11 Fan Stage with TCS at 74% Speed.

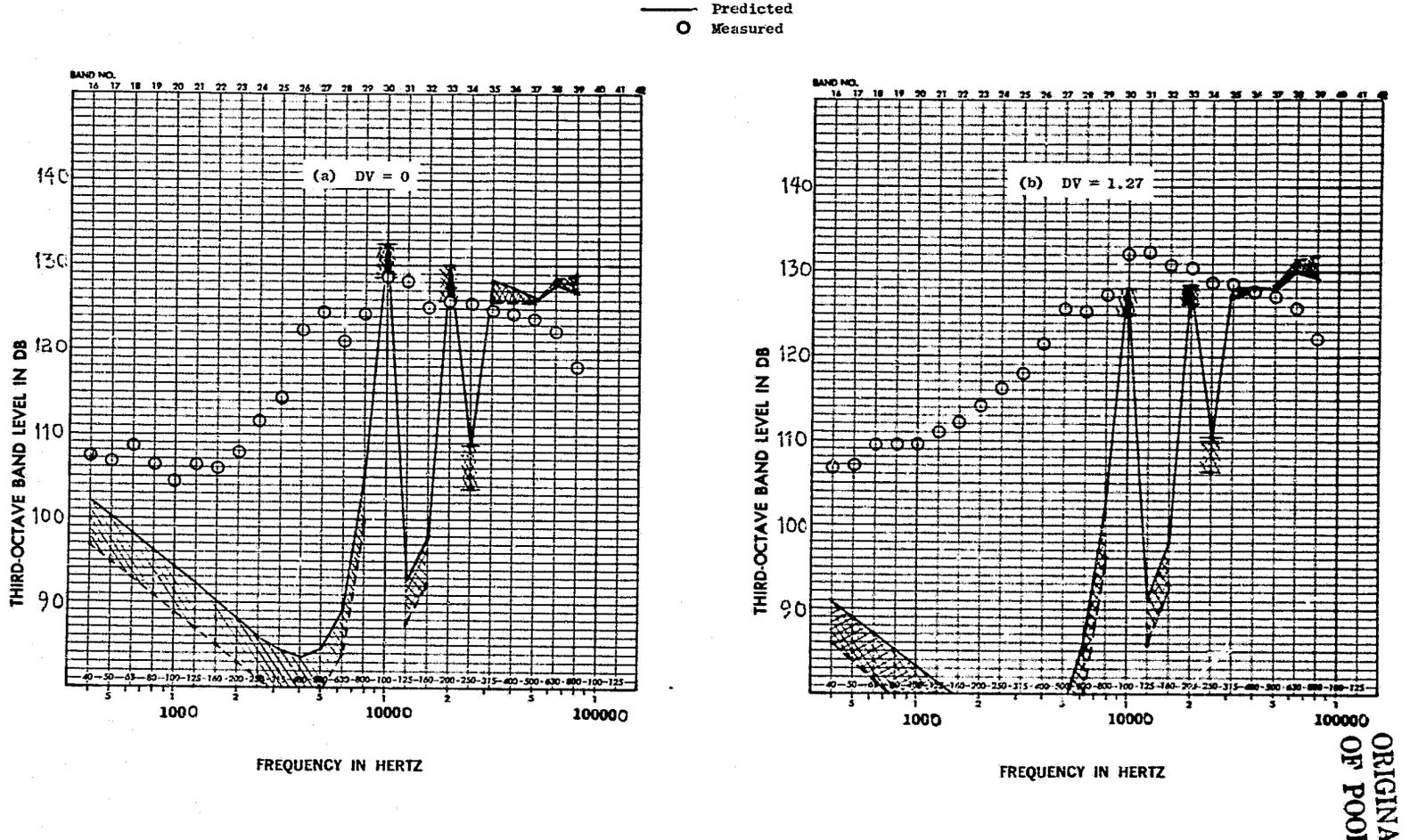

Figure 22. Comparison of Predicted and Measured Inlet PWL Spectra for NASA Rotor 11 Fan Stage with TCS at 80% Speed.

Table 3. NASA Rotor 11 Fan Stage Data/Theory Comparison Summary Chart.

Case No.	% N_F	DV	TCS	$(M_r)_{tip}$	$(M_r)_{pitch}$	Figure
1	54	0	No	0.736	0.605	14a
2	54	1.27	No	0.723	0.593	14b
3	60	0	No	0.823	0.676	15a
4	60	1.27	No	0.805	0.659	15b
5	69	0	No	0.955	0.785	16a
6	69	1.27	No	0.932	0.761	16b
7	74	0	No	1.028	0.846	17a
8	74	1.27	No	1.005	0.820	17b
9	80	0	No	1.115	0.922	18a
10	80	1.27	No	1.093	0.896	18b
11	54	0	Yes	0.736	0.605	19a
12	54	1.27	Yes	0.723	0.593	19b
13	69	0	Yes	0.955	0.785	20a
14	69	1.27	Yes	0.932	0.761	20b
15	74	0	Yes	1.028	0.846	21a
16	74	1.27	Yes	1.005	0.820	21b
17	80	0	Yes	1.005	0.922	22a
18	80	1.27	Yes	1.093	0.896	22b

averages of all the data taken in Reference 6. A range of length scale ratios is shown in Table 4 with the TCS in place, because the tangential length scale was found to be smaller than was measurable with the instrumentation employed by the authors of Reference 6. The low limit corresponds to assuming that ℓ_t is the same with the TCS as without, while the high limit corresponds to assuming that the scale ratio $\lambda = \ell_a/\ell_t$ is the same with TCS as without. The actual scale is probably somewhere in between the two limits.

The data/theory comparisons for the cases with TCS are shown in Figures 19 through 22. The shaded band for the predictions corresponds to the range of length scales assumed, $90 \leq \ell_a/\ell_t \leq 300$. In general, the case $\ell_a/\ell_t = 300$ corresponds to the high limit of the shaded band for frequencies below 3 x BPF, and the case $\ell_a/\ell_t = 90$ corresponds to the high limit for frequencies above 3 x BPF. The general observation to be made about the results shown in Figures 19 through 22 is that the predicted noise reduction due to addition of the TCS is at least as much as was measured, if not more. The predicted spectra indicate that residual rotor/turbulence interaction noise still exists at BPF for the DV = 0 (open throttle) cases, whereas the DV = 1.27 (closed throttle) cases do not appear to have any appreciable rotor/turbulence noise contribution.

A comparison of measured and predicted BPF tone levels, i.e., the 1/3-octave band level containing the tone, is shown in Figure 23. The underprediction at 60% speed without TCS (see Figure 15) is due to the BPF being right at the edge of the band. The agreement is good except at high speeds where transonic conditions exist and the theory is not really expected to be accurate.

Data/theory comparisons were also carried out for a scale model variable-pitch fan tested in the same anechoic chamber (General Electric Research and Development Center, Schenectady, New York) as was the NASA Rotor 11 fan stage reported in Reference 6. Inlet arc 1/3-octave PWL spectrum comparisons are shown in Figures 24a-f, the data being taken from Reference 26. This fan has 18 blades and 33 vanes, and has a design tip speed of 306 m/s (1000 fps). It is a variable-pitch design and consequently has a radially constant solidity (chord/spacing), as opposed to conventional fixed blade fans which usually are designed to have radially constant chord and variable solidity. It also has significantly fewer rotor blades than the NASA Rotor 11 fan stage (18 versus 44), and has a subsonic design tip speed.

Table 4. Summary of Assumed Turbulence Quantities for GE Schenectady Anechoic Chamber Fan Noise Facility.

Parameter	No TCS	With TCS
u_a/U_a	0.015	0.0045
u_t/u_a	2.0	0.75
ℓ_a, m	2.9	0.86
ℓ_a/ℓ_t	300	90-300

Table 5. QCSEE Scale Model Variable Pitch Fan Data/Theory Comparison Summary Chart.

Case No.	% N_F	DV	TCS	$(M_r)_{tip}$	$(M_r)_{pitch}$	Figure
1	60.2	7.75	No	0.620	0.514	24a
2	70.4	7.75	No	0.731	0.607	24b
3	80.4	7.75	No	0.845	0.706	24c
4	90.5	7.75	No	0.968	0.811	24d
5	95.5	7.75	No	1.063	0.866	24e
6	99.2	7.75	No	1.074	0.903	24f

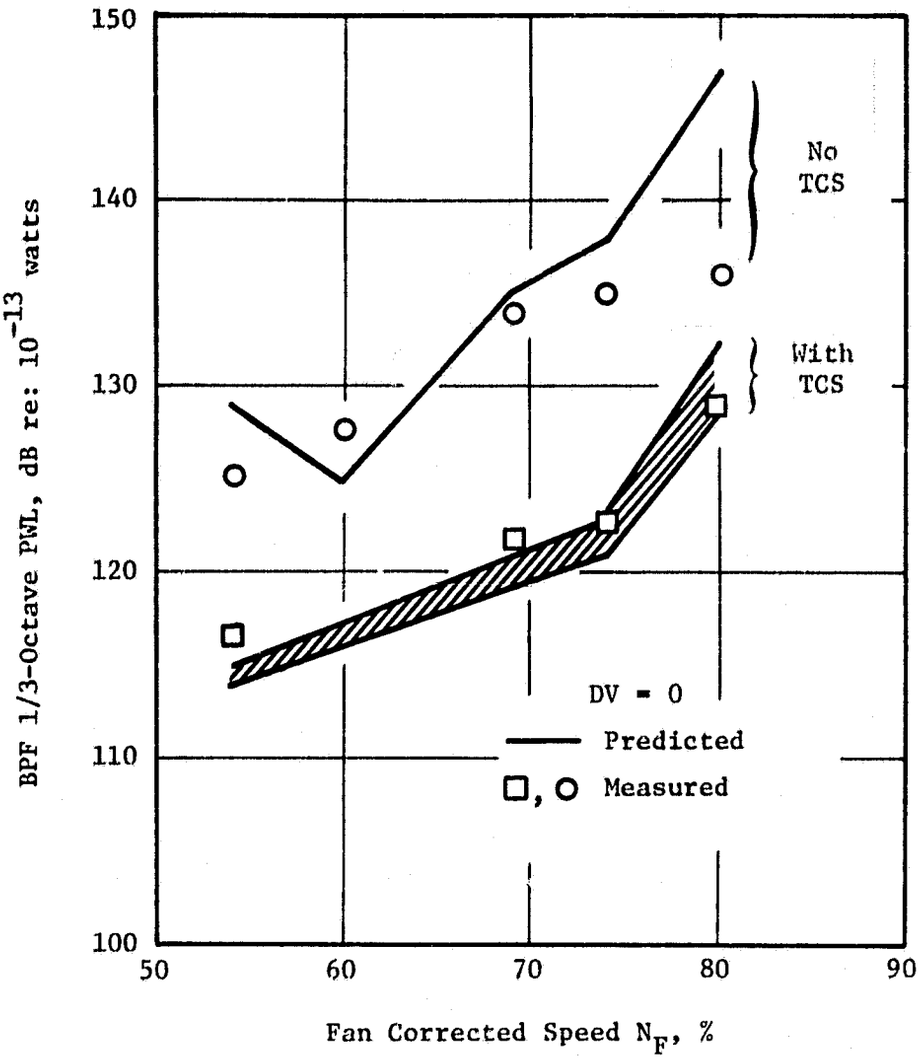

Figure 23. Comparison of Predicted and Measured Inlet BPF PWL for NASA Rotor 11 Fan Stage at DV = 0 With and Without TCS.

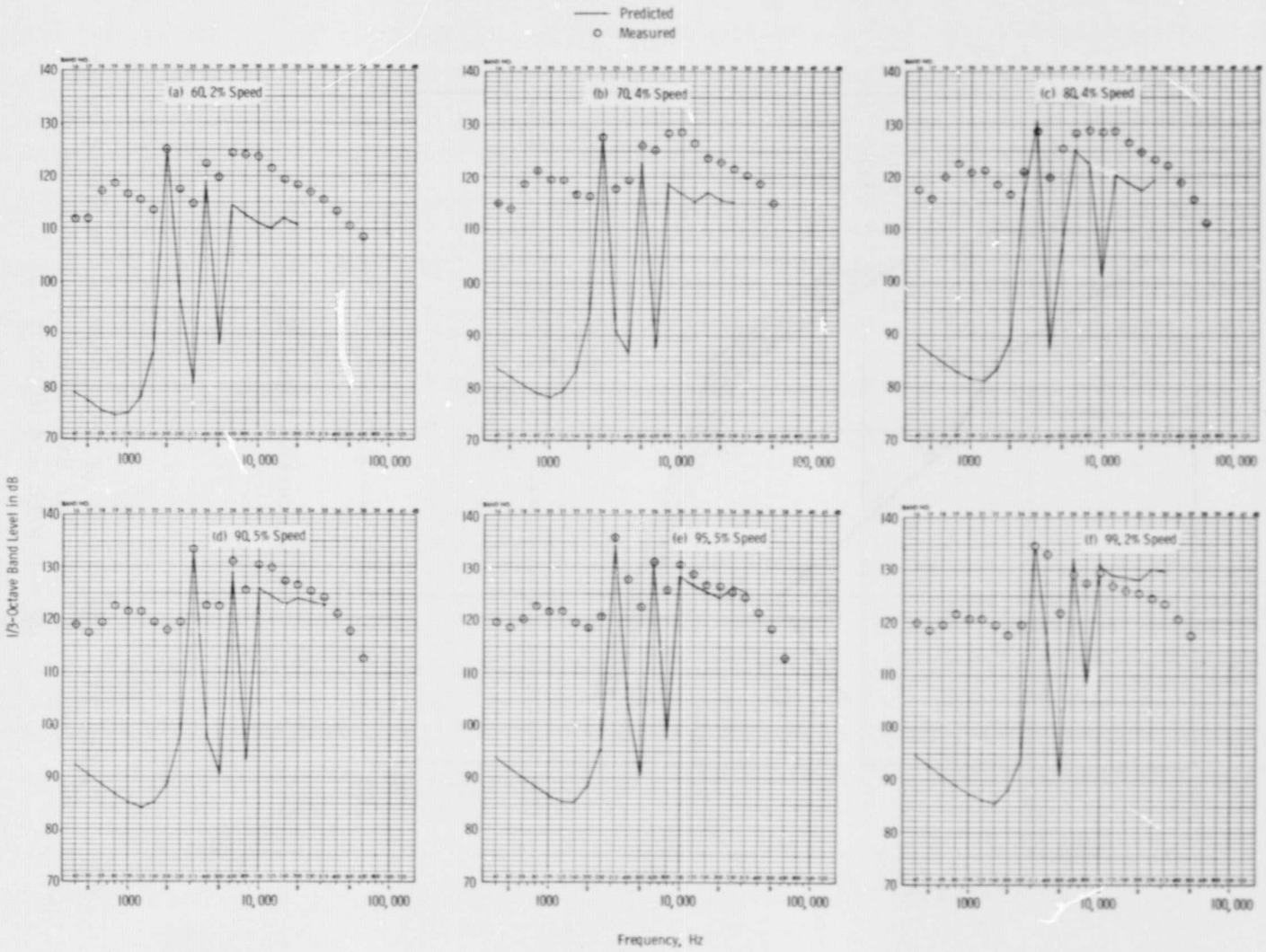

Figure 24. Comparison of Predicted and Measured Inlet PWL Spectra for QCSEE Variable-Pitch Scale Model Fan Stage.

The predictions shown in Figures 24a-f were done in the same fashion as was done for the NASA Rotor 11 fan, i.e., section properties at the rms pitchline radius were used. The turbulence properties of Table 4 were used as input, since the same facility was used. The data was taken without a TCS, and only along the QCSEE engine sea level operating line. The data shown in Figures 24a-f were taken with a hardwall, low Mach number inlet installed. Again, input lift coefficients for the predictions were based on pitchline incidence angles rather than rotor pressure ratio. A summary of comparison points is given in Table 5.

The same observations made previously for the Rotor 11 data/theory comparisons apply for the QCSEE Variable Pitch fan also. The BPF tones are predicted quite well, the rotor/turbulence broadband noise contributes nothing to the observed broadband levels, and the theory overpredicts at transonic relative Mach numbers. A summary of the QCSEE fan stage data/theory comparisons for BPF harmonics is shown in Figure 25.

It can be seen from Figures 24 and 25 that the predictions indicate only a small contribution of rotor/turbulence noise at 3 x BPF and higher, especially at the lower speeds. The progresively larger contributions at higher speeds is consistent with the change in measured spectrum shape with speed, i.e., the BPF higher harmonic peaks progressively stand out more above the broadband levels as speed increases. It is possible that the input lift coefficients based on incidence angle are too low, and this would yield lower predicted levels at frequencies of 2 x BPF and higher. The few narrowband samples given in Reference 25 do show, however, that the tones do not contribute significantly to the 1/3-octave levels above the third harmonic, supporting the predicted trends of Figure 24.

An attempt was made to predict the blade passing frequency tones for the Pratt & Whitney JT15D engine, and compare the predictions with the experimental results recently obtained* in the NASA-Ames 40x80 ft wind tunnel. Turbulence measurements were made previously, reported in Reference 20, approximately 20 ft upstream of the engine inlet, but no data was available on the

*Contract NAS2-8675 in progress, unpublished data.

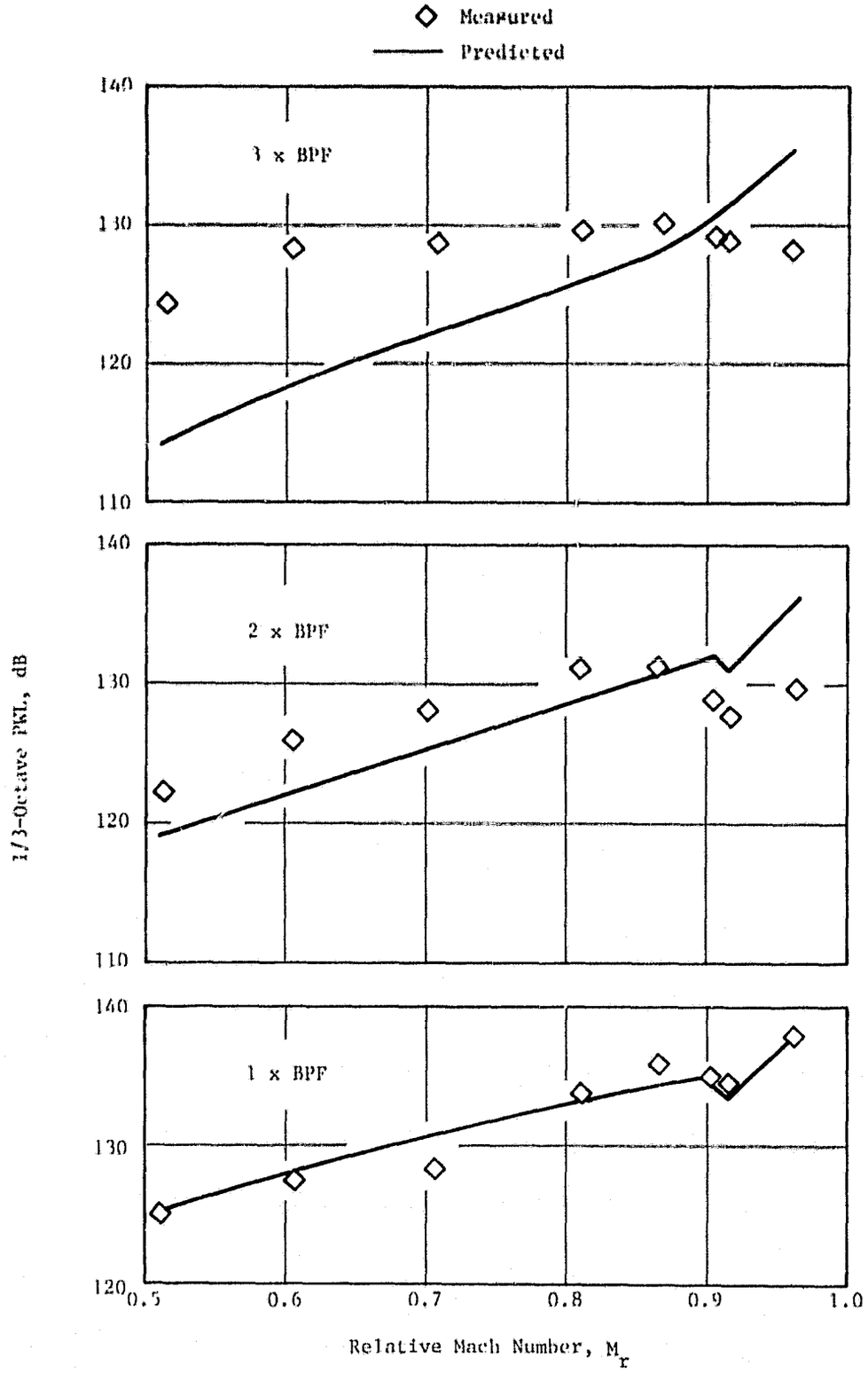

Figure 25. Comparison of Measured and Predicted n x BPF Tone PWL for QCSEE Scale Model Fan Stage.

turbulence at the fan face. Linear sudden contraction theory, Reference 5, was therefore employed to infer the turbulence properties at the fan face, based on the reported measurements upstream of the inlet. The measurements in Reference 20 showed the axial turbulence intensity in the tunnel test section to be ~0.2%, independent of tunnel speed. Likewise, the transverse turbulence intensity was found to be ~0.55%, also independent of tunnel speed.

Using an engine test condition corresponding to a fan tip speed of 1020 fps (the lowest tip speed for which data was taken in this series*), the fan face velocity is approximately 394 fps. For tunnel speeds of 11 knots and 80 knots, this implies a turbulence contraction ratio (or speed ratio) of 21 and 3, respectively. Applying the theory of Reference 5, the turbulence properties computed at the fan face are as follows:

Turbulence Component	V_o = 11 kts.	V_o = 80 kts.
Axial intensity	0.00084%	0.032%
Transverse intensity	0.12%	0.32%
Axial length scale	7.56 ft	3.97 ft
Transverse length scale	0.015 ft	0.15 ft

It can be seen from the above tabulation that the estimated turbulence intensities are extemely small; the corresponding blade passing tone PWL levels were predicted to be 99.0 dB and 107.3 dB, for 11 knots and 80 knots, respectively. The corresponding measured values were 123.8 dB and 117.5 dB, for 11 knots and 80 knots, respectively.

The above results would seem to imply that rotor/turbulence noise in the 40x80 ft wind tunnel is not a significant contribution. However, the fact that the measured noise decreases by 6.3 dB from a wind velocity of 11 knots to 80 knots indicates some sort of flight "clean-up" effect is taking place. In fact, examination of 20 Hz narrowband spectra of the far field microphone data shows that the 11 knot wind data exhibits skirted peaks at blade passing frequency typical of a turbulence-modulated tone. The 80 knot data, however, shows much narrower peaks.

*Ibid.

One possible explanation for the above inconsistencies is that the sudden contraction theory may not be an adequate representation of what happens to the turbulence in a wind tunnel as it contracts in passing through the engine inlet. There is some evidence, reported in Reference 24, that the transverse intensity does not change at all from upstream to the fan face. Further, there is also some evidence* that axial intensity does not change appreciably from the tunnel test section to the fan face.

Examination of the experimental measurements of wind tunnel contraction on free stream turbulence made by Uberoi, Reference 27, shows that the reduction in axial turbulence intensity across a contraction is not nearly as great as the theory of Reference 5 would predict for large contractions. The corresponding change in transverse turbulence intensity is overestimated by the theory, but the error is not nearly as great as that for the axial intensity. A summary of these trends are shown in Figure 26.

The differences shown in Figure 26 would affect the 11 knot predictions but would have no significant impact on the 80 knot predictions, since the contraction ratio U_a/V_o (fan axial velocity/tunnel velocity) is only about 3:1 for the 80 knot case. The 11 knot condition, however, was experimentally obtained by turning off the tunnel fans and allowing the engine to pump the tunnel naturally. This condition could therefore produce turbulence characteristics which are significantly different from those measured in Reference 20 with the tunnel fans in operation. Extrapolating the turbulence data of Reference 20 to 11 knots (the minimum tunnel speed for which data were taken was ~40 knots) could therefore yield an incorrect assessment of the turbulence properties for the 11 knot case, contributing to the poor agreement between experiment and prediction.

Another source of the differences obtained between predicted and measured BPF tone levels is that the predictions were originally made utilizing only the dipole source contribution, and the quadrupole source contribution was omitted. This was done because there was insufficient information available to

*Personal communication, C. Feiler and L. Shaw of NASA Lewis Research Center. Results obtained in Lewis 9x15 wind tunnel.

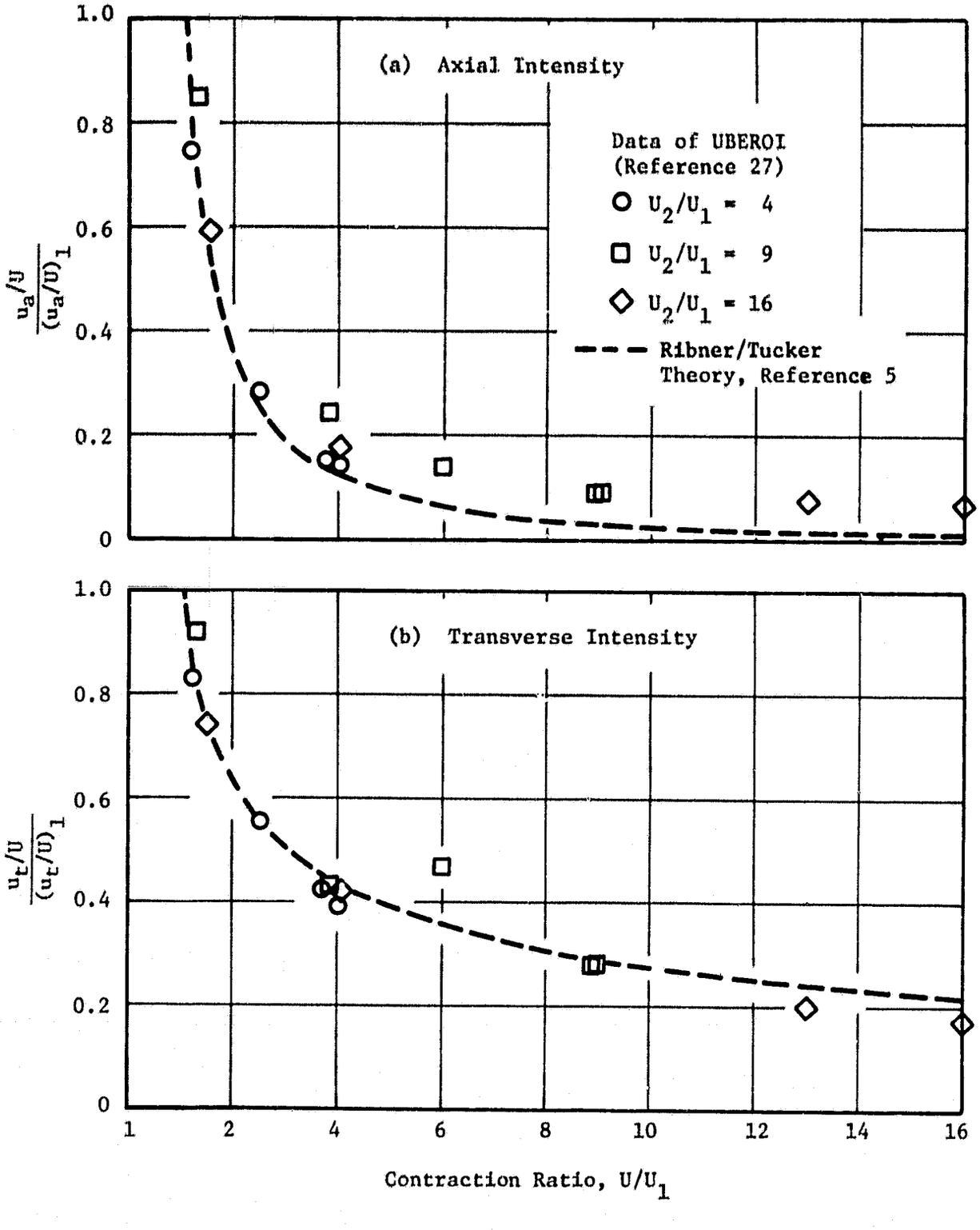

Figure 26. Effect of Wind Tunnel Contraction on Free-Stream Turbulence Intensity (From References 5 and 27).

GE on the aerodynamic characteristics of the JT15D fan rotor. If, however, it is assumed that its loading characteristics are similar to current high speed fan designs in the GE family of engines, a reasonable estimate of the blade loading (or lift) coefficient can be made, and this is required to predict the quadrupole contribution to the BPF tone level. Assuming a typical lift coefficient of $C_\ell = 0.45$, the quadrupole contribution at $V_o = 80$ knots was found to be equal to the dipole contribution, thus increasing the predicted level to 110.3 dB, within ~7 dB of the measured level of 117.5 dB.

Another prediction was also made for the 80 knot case where the length scales were assumed to obey the sudden-contraction theory behavior as far as elongation of the axial length scale and contraction of the transverse length scale is concerned. The turbulence intensities, however, were assumed to be the same at the fan face as was measured upstream, as was observed by Hodder in Reference 24. This prediction yielded a BPF tone level of 116.0 dB, within 1.5 dB of the measured value of 117.5 dB. It is recognized that Hodder's results may not apply to the 40x80 wind tunnel/JT15D engine application, since they were obtained in a much smaller tunnel on a low speed fan. Nevertheless, the majority of the evidence collected thus far indicates that the sudden-contraction theory is inadequate for estimating fan face turbulence intensities from measurements made far upstream of the inlet. The empirical adjustments of the sort described above seem warranted and do yield reasonable agreement between measured and predicted noise levels.

To test the ability of the prediction model to evaluate wind tunnel turbulence noise for a fan, predictions were made of the BPF tone PWL (inlet arc) for the 15-blade fan tested in the NASA-Lewis 9x15 wind tunnel, the results of which are given in Reference 21. In this case, turbulence measurements were made inside the fan duct close to the rotor, so the question of the inadequacy of the sudden-contraction theory for predicting turbulence intensity changes is not an issue. For the static ($V_o \tilde{} 0$) case, the measured transverse and axial intensities were used to estimate the effective contraction ratio, using the sudden-contraction theory, and this contraction ratio was used to estimate the transverse length scale only, based on the measured axial length scale. For the wind-on case, V_o = 80 knots, the actual contraction U_a/V_o was used to estimate the transverse length scale.

The resulting predictions of BPF tone PWL versus fan speed for both static and wind-on conditions is shown in Figure 27 along with the measured values. It can be seen that the agreement is, on the average, reasonably good, considering the approximations and assumptions made, lending further support to the validity of the basic rotor/turbulence interaction prediction model.

Based on the analysis and review of existing data described above, it is concluded that the current rotor/turbulence interaction noise model is adequate for predicting wind-tunnel turbulence/rotor interaction noise when the fan face turbulence properties are known. When only upstream turbulence properties are given, the sudden-contraction portion of the turbulence prediction may be inadequate for large contraction ratios. For tunnel velocities of 80 kts. or less, this could imply an underprediction of the BPF tone PWL by about 7-8 dB, if the prediction model is used as-is. With the use of an empirical correction to maintain constant fan face turbulence intensity independent of tunnel speed or fan speed, the prediction will be fairly accurate. Whenever contraction ratio is close to unity, i.e., $V_o \approx U_a$, either method of prediction will yield adequate results.

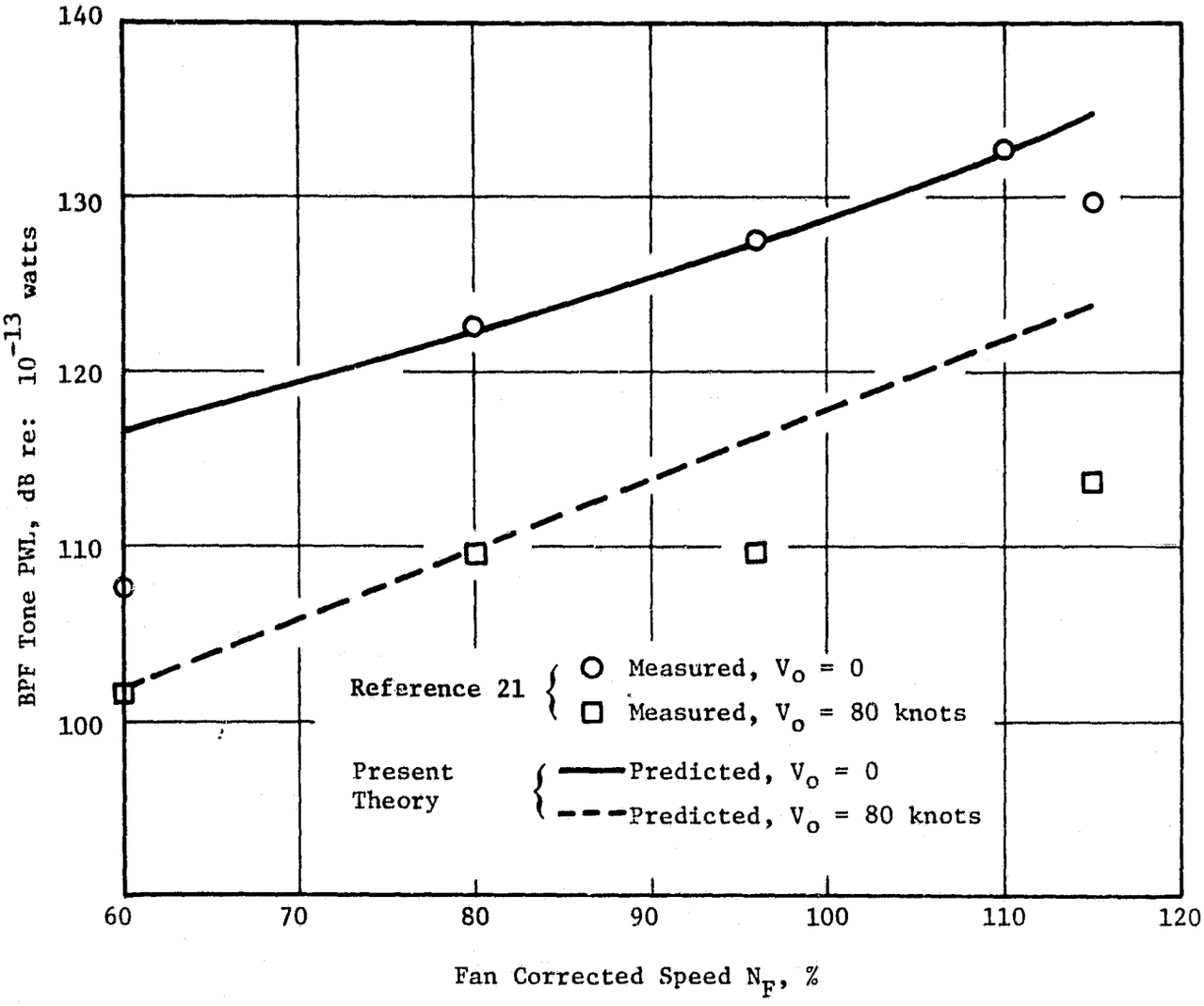

Figure 27. Predicted Vs. Measured BPF Tone PWL for Rotor 55 in NASA-Lewis 9 x 15 Wind Tunnel (Reference 21).

7.0 PARAMETRIC STUDY

Having established that the present rotor/turbulence interaction theory adequately predicts rotor/turbulence noise (for subsonic relative Mach numbers) over a wide range of fan operating conditions, fan geometries, and inlet turbulence conditions, a parametric study of rotor turbulence noise characteristics was carried out. It was shown in the previous section that rotor/turbulence noise is characterized by strong, narrow peaks at blade passing frequency (BPF) and its harmonics, and contributes an insignificant amount of broadband noise to the total fan noise spectrum. Therefore in the present parametric study, predictions are made only at blade-passing frequency and its harmonics.

When only the BPF tones and harmonics are of interest, a considerable simplification of the prediction equations can be made when $\ell_a/S \gg 1$. This simplification is described in detail in Appendix A, and permits calculation of the total sound power in the vicinity of BPF, and for each harmonic thereof. This method was found to be quite accurate when compared to 1/3-octave calculations, over a wide range of fan operating conditons, inlet turbulence conditions, and fan geometries. The parametric study to be described in the following sections utilizes the simplified theory outlined in Appendix A.

The prediction program requires as input the fan rotor inlet axial and rotational Mach numbers and rotor total pressure ratio. A composite plot of these fan parameters was made for several fan stages, including those discussed in the previous section. Figures 28 and 29 show plots of axial Mach number M_a and fan pressure ratio PR versus tip speed Mach number M_t, respectively. It can be seen that many of the fans have a common flow versus speed (M_a versus M_t) characteristic, and a common work versus speed (PR versus M_t) characteristic.

A common operating characteristic of M_a and PR versus M_t was therefore selected for the parametric study, and these are shown as the solid lines in Figures 28 and 29. This is henceforth referred to as the low-flow (LF) transonic fan operating line. The QCSEE fan and NASA Rotor 55 fans, however, have

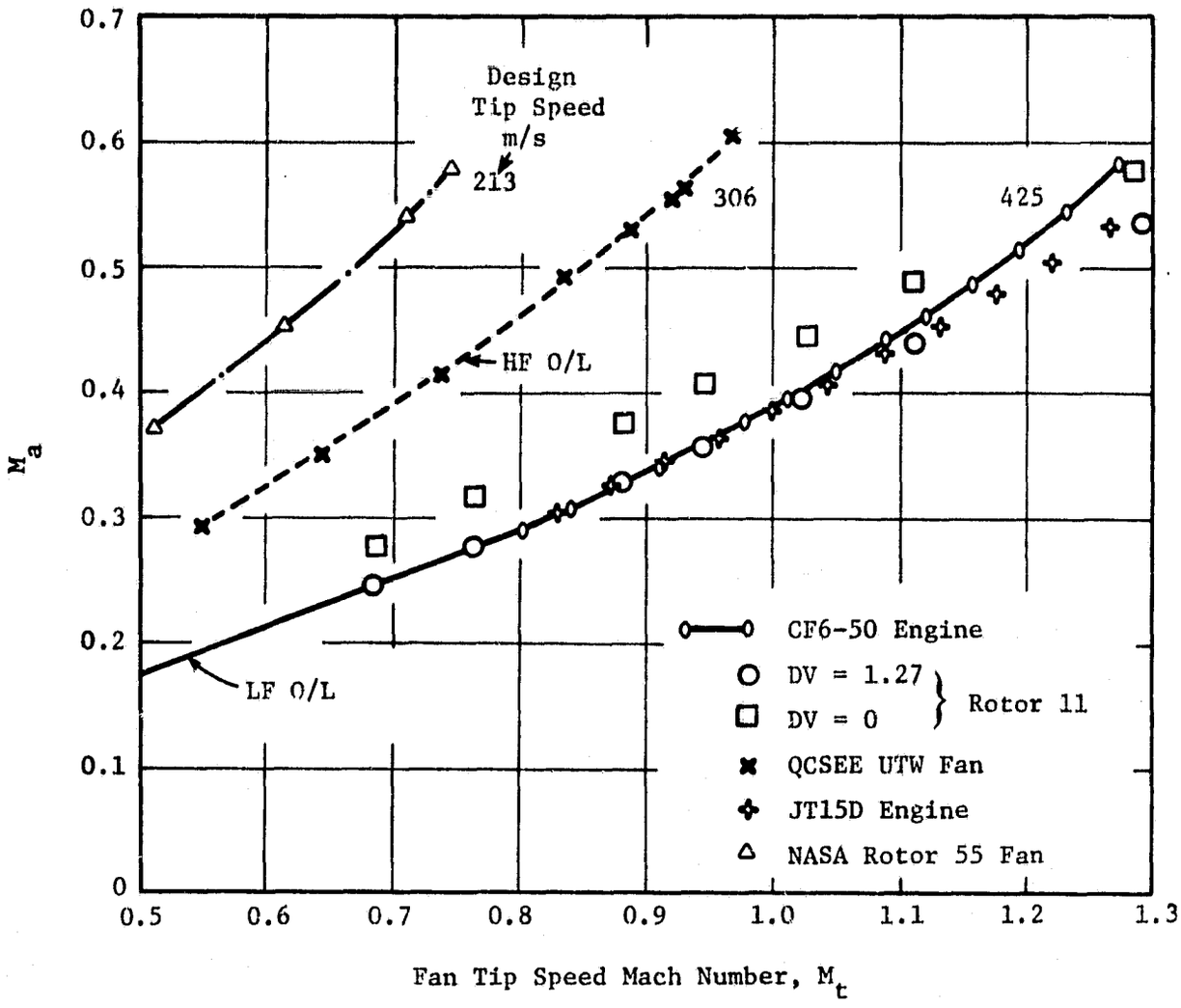

Figure 28. Axial Mach Number Vs. Tip Speed Mach Number (M_a Vs. M_t) Characteristics for Several Fan Stages.

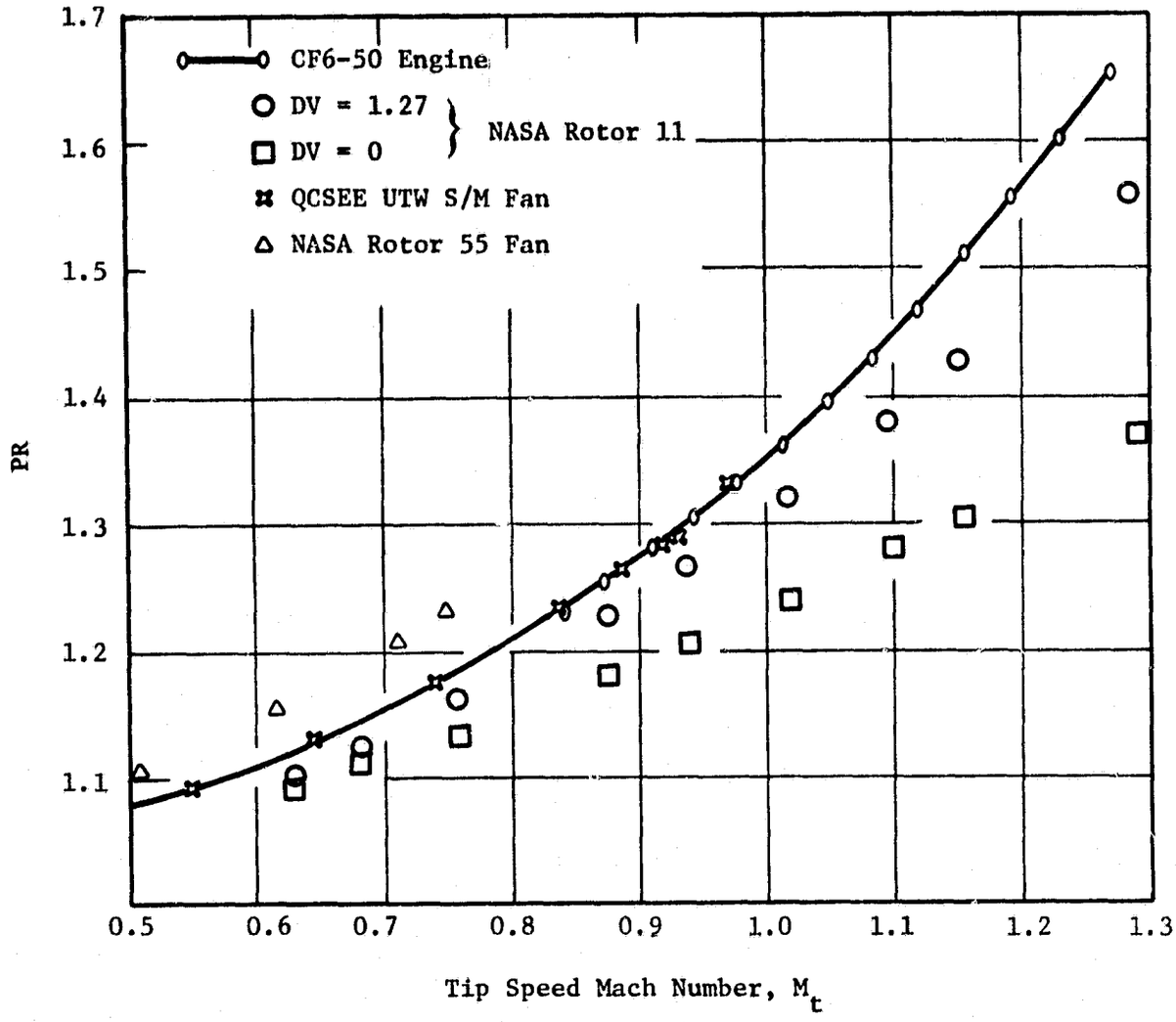

Figure 29. Pressure Ratio Vs. Tip Speed Mach Number (PR Vs. M_t) Characteristics for Several Fan Stages.

higher M_a versus M_t characteristics (Figure 28), and this is related to their design tip speeds, which are subsonic. A limited number of calculations were therefore performed using the QCSEE flow characteristic (M_a versus M_t), and this operating line is henceforth referred to as the high-flow (HF) subsonic fan characteristic.

Several fan sizes were selected for study because it is known from theoretical considerations that the turbulence scale-to-blade spacing ratio is important. Hence different fan sizes operating in the same turbulence environment may give different noise levels when the levels are corrected to a common fan inlet area. Fan diameters of 2.13 m (84 inches), 1.07 m (42 inches), and 0.53 m (21 inches) were selected for study. They are henceforth referred to as full-scale (FS), half-scale (HS), and quarter-scale (QS), respectively.

Blade number was also varied, values of N_B = 38, 28, and 18 being selected for study. These values represent the range of fan types currently in use. For example the diameter/blade number combination 2.13 m/38 is close to the GE CF6 engine fan, and the combination 0.53 m/28 is the same as the P&W JT15D engine fan.

Blade tip solidity was held constant at $(c/s)_{tip}$ = 1.3 for all LF transonic fan cases and 1.0 for all HF subsonic fan cases, as it is usual design practice to set rotor tip solidity approximtely equal to design tip relative Mach number. A list of the fan geometry parametric variations investigated is shown in Table 6.

Calculations of rotor/turbulence noise were made for each of the configurations listed in Table 6, over the tip speed Mach number range $0.5 \leq M_t \leq 1.0$. The calculations were performed for several turbulence conditions, as follows:

- Outdoor Test Stand (OTS)
- AMES 40x80 Wind Tunnel, V_o = 80 kts (AWT1)
- AMES 40x80 Wind Tunnel, V_o = 180 kts (AWT2)
- In-Flight, V_o = 180 kts (FLT)

Table 6. Summary of Fan Geometries for Parametric Study.

Fan Designation	D_t	N_B	$(c/s)_{tip}$	Operating Line	Aspect Ratio
QS 38 LF	0.53 m	38	1.3	LF	2.3
HS 38 LF	1.07 m	38	1.3	LF	2.3
FS 38 LF	2.13 m	38	1.3	LF	2.3
QS 28 LF	0.53 m	28	1.3	LF	1.7
FS 28 LF	2.13 m	28	1.3	LF	1.7
QS 18 LF	0.53 m	18	1.3	LF	1.1
FS 18 LF	2.13 m	18	1.3	LF	1.1
FS 18 HF	2.13 m	18	1.0	HF	1.9

Additional calculations were made for the quarter-scale fans in the Schenectady Anechoic Chamber (SAC). Noise levels were obtained at blade-passing harmonics n=1 through 8 for all cases. Some parametric studies were also made of the effect of length scale and flight speed.

A question was raised in the preceding section about the adequacy of using the sudden contraction theory (Reference 5) for estimating the fan face turbulence characteristics based on measured turbulence properties far upstream. In the present study, sudden contraction theory was used without alteration; however, estimates were made of the range or uncertainty band in predicted noise levels for the wind tunnel cases, and the uncertainty band was found to be less than 7 dB for the worst cases. A more detailed discussion of this topic is covered in the next section, NASA-AMES 40 x 80 WIND TUNNEL EVALUATION, but it is noted here that the 7 dB uncertainty band is not large at all compared to the uncertainties associated with turbulence variability, tone unsteadiness and day-to-day weather changes which affect the Outdoor Test Stand and Flight rotor/turbulence noise levels.

7.1 COMPONENT SOURCE CONTRIBUTIONS

The relative contributions of the dipole (unsteady lift) and quadrupole (steady loading/turbulence interaction) sources to the total predicted rotor/turbulence noise was examined first. Figure 30 shows the contributions for the quarter-scale fans on the Low-Flow operating line, in the Schenectady Anechoic Chamber (SAC) environment. Note that the dipole source dominates the BPF tone for the 38-blade rotor, whereas the quadrupole source dominates for all but the lowest tip speeds ($M_t > 0.6$), for the 18-blade rotor. This is because the rotor blade aspect ratio is smaller for the 18-blade rotor, and the unsteady lift response function decreases as aspect ratio is reduced. The lift coefficient, which determines the quadrupole level, is the same for the two blade numbers, since rotor solidity was held constant. For this parametric study, input lift coefficient was $C_\ell = 0.45$, based on the low-flow operating line pressure ratio and flow versus speed. For this parametric study, using leading edge loading or incidence angle for computing C_ℓ was not feasible

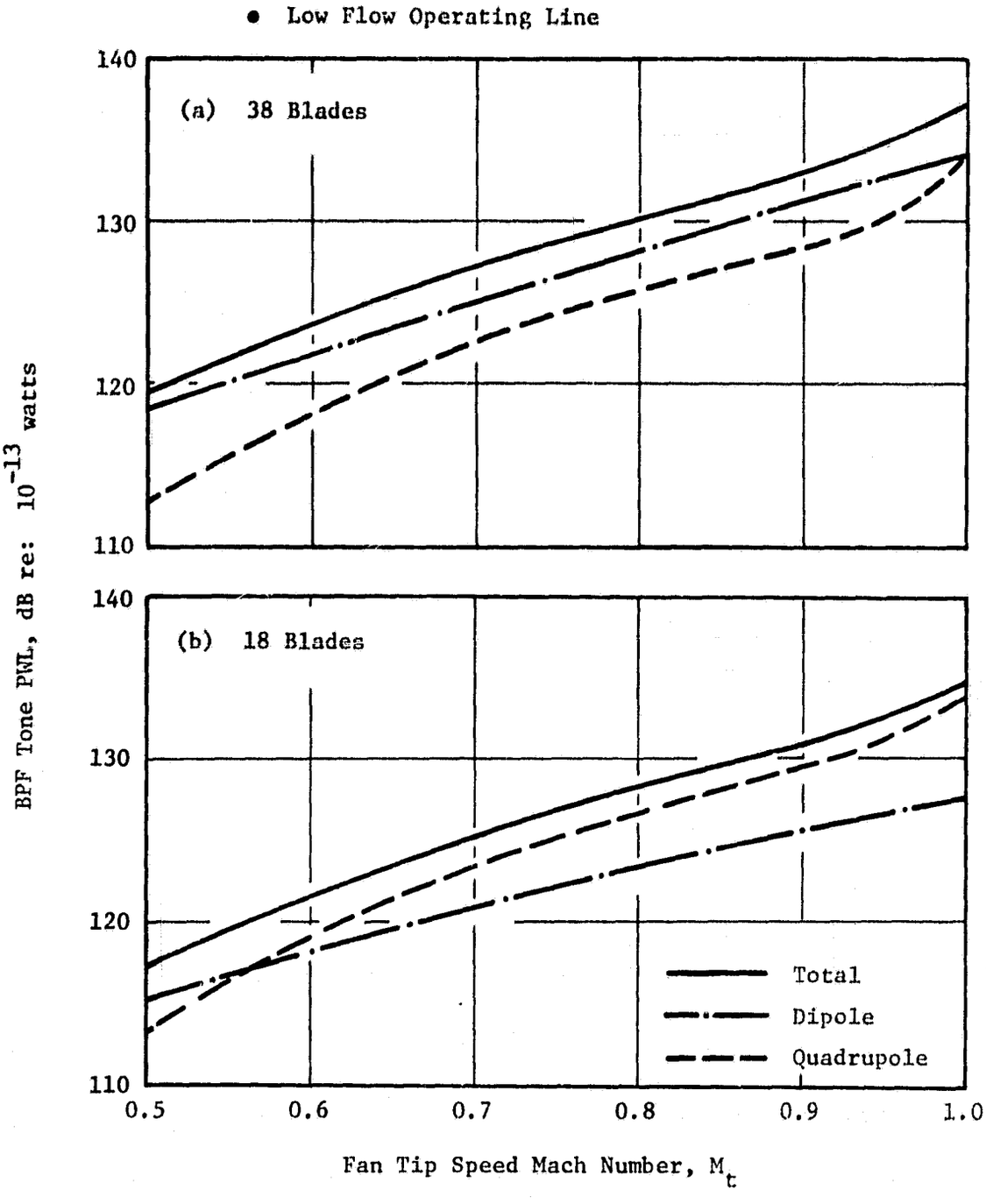

Figure 30. Component Source Contributions to BPF Tone PWL for Quarter-Scale Fans in Schenectady Anechoic Chamber.

since the actual running incidence angle is an unknown function of aerodynamic design criteria and effectiveness of the design process, and accounting for this was beyond the scope of the present study.

Figure 31 shows the component source contribution breakdown as a function of BPF harmonic number for the quarter-scale fans in the SAC turbulence environment. These results indicate that the higher harmonics of BPF are dominated by the quadrupole source, even for the high blade number $N_B = 38$. The fall-off with harmonic number n is very large for the dipole source compared to that for the quadrupole source.

Similar trends are shown for the Outdoor Test Stand (OTS) turbulence environment (Figure 32), the Ames 40 x 80 Wind Tunnel (AWT) environment (Figures 33 and 34), and the Flight (FLT) environment (Figure 35). The above calculations were repeated for the full-scale fan in the OTS, AWT and FLT turbulence environment, and these results are shown in Figures 36 through 39. Sample spectra, i.e., BPF tone PWL versus n, are given for both quarter- and full-scale fans, for each turbulence environment, in Figures 40 through 43.

It can be seen from the results shown in Figures 30 through 39 that the trends of BPF tone PWL with Mach number M_t are similar for SAC, OTS, and AWT, but the FLT condition yields a flatter curve. Also, the quadrupole contribution for the FLT condition is not as great as in the other test site conditions. Even though the BPF tone levels in the AWT are similar at $V_o = 80$ knots and 180 knots, the higher harmonics of BPf are 2-5 dB lower at 180 knots relative to levels at 80 knots, the larger differences occurring at the higher tip speed Mach numbers.

7.2 EFFECT OF BLADE NUMBER

The spectra in Figures 40 through 43 also show that the higher harmonics of BPF decrease with increasing blade number, even though the effect of blade number is very small at BPF. The effect of blade number is shown explicitly in Figures 44 and 45. Figure 44 shows the sensitivity of BPF tone levels to N_B for the three test conditions, for the full-scale fan with low-flow operating line. Figure 45 shows the corresponding BPF harmonic spectra.

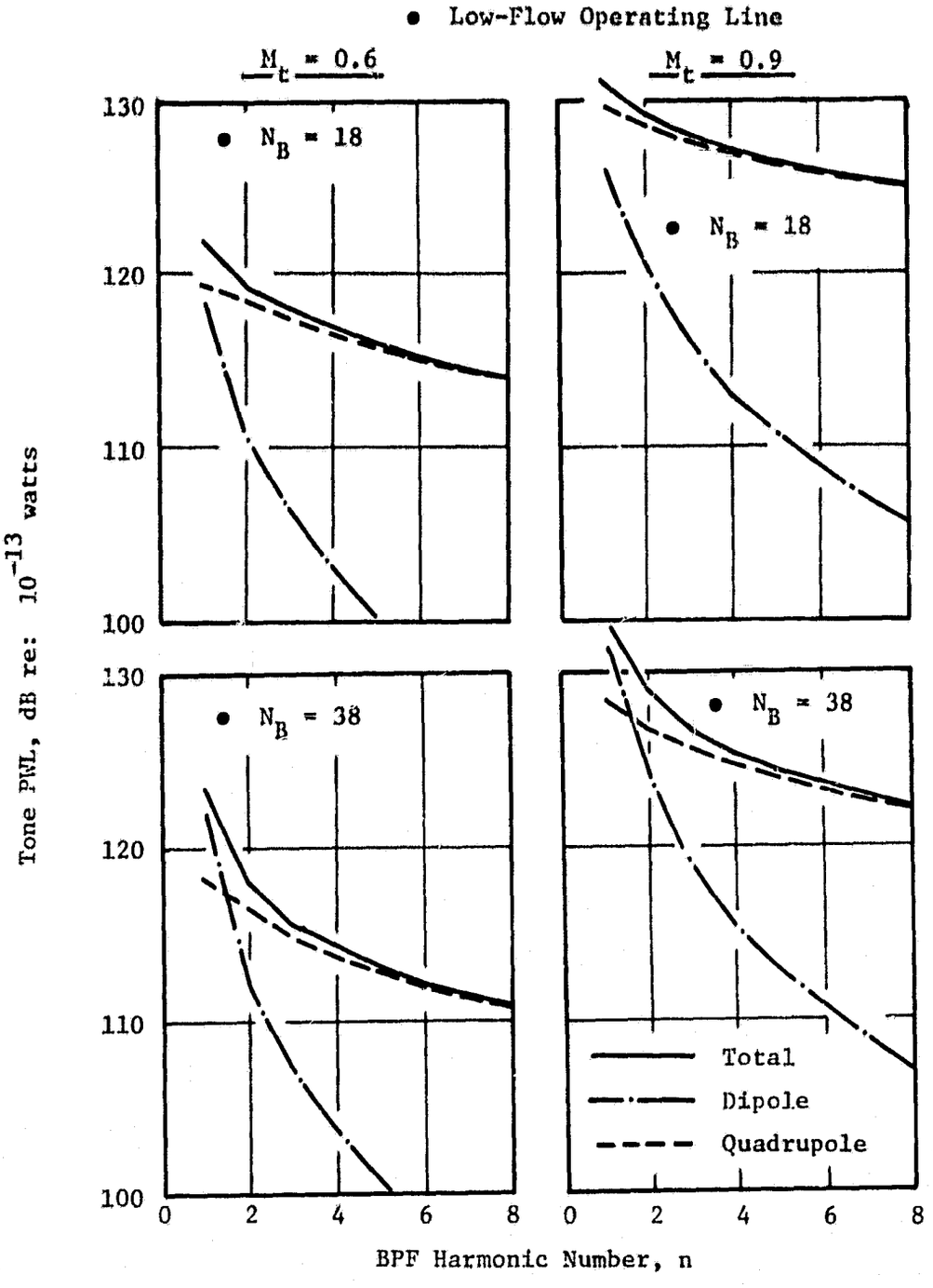

Figure 31. Component Source Contributions to Tone PWL Spectra for Quarter-Scale Fans in Schenectady Anechoic Chamber.

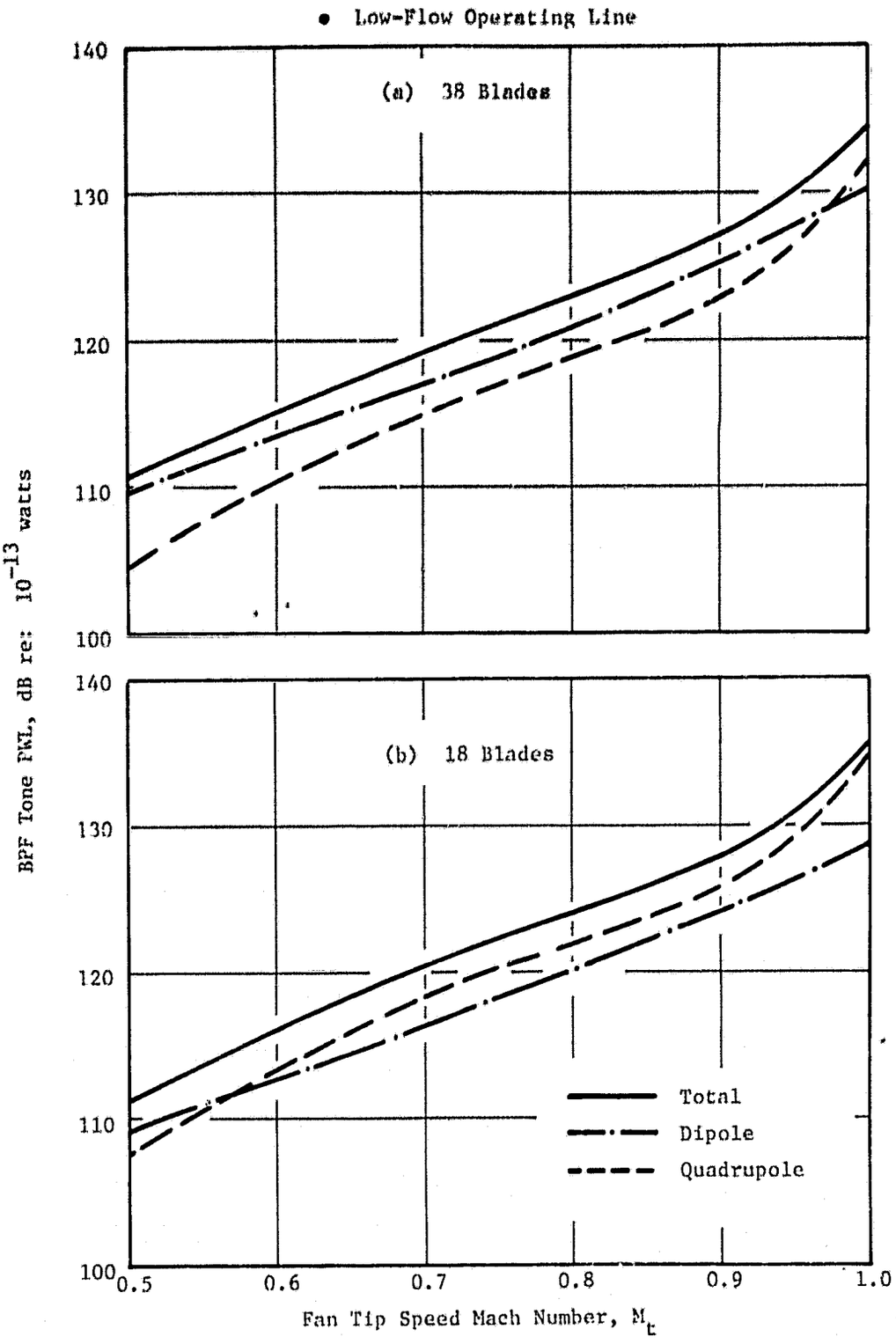

Figure 32. Component Source Contributions to BPF Tone PWL for Quarter-Scale Fans in Outdoor Test Stand Environment.

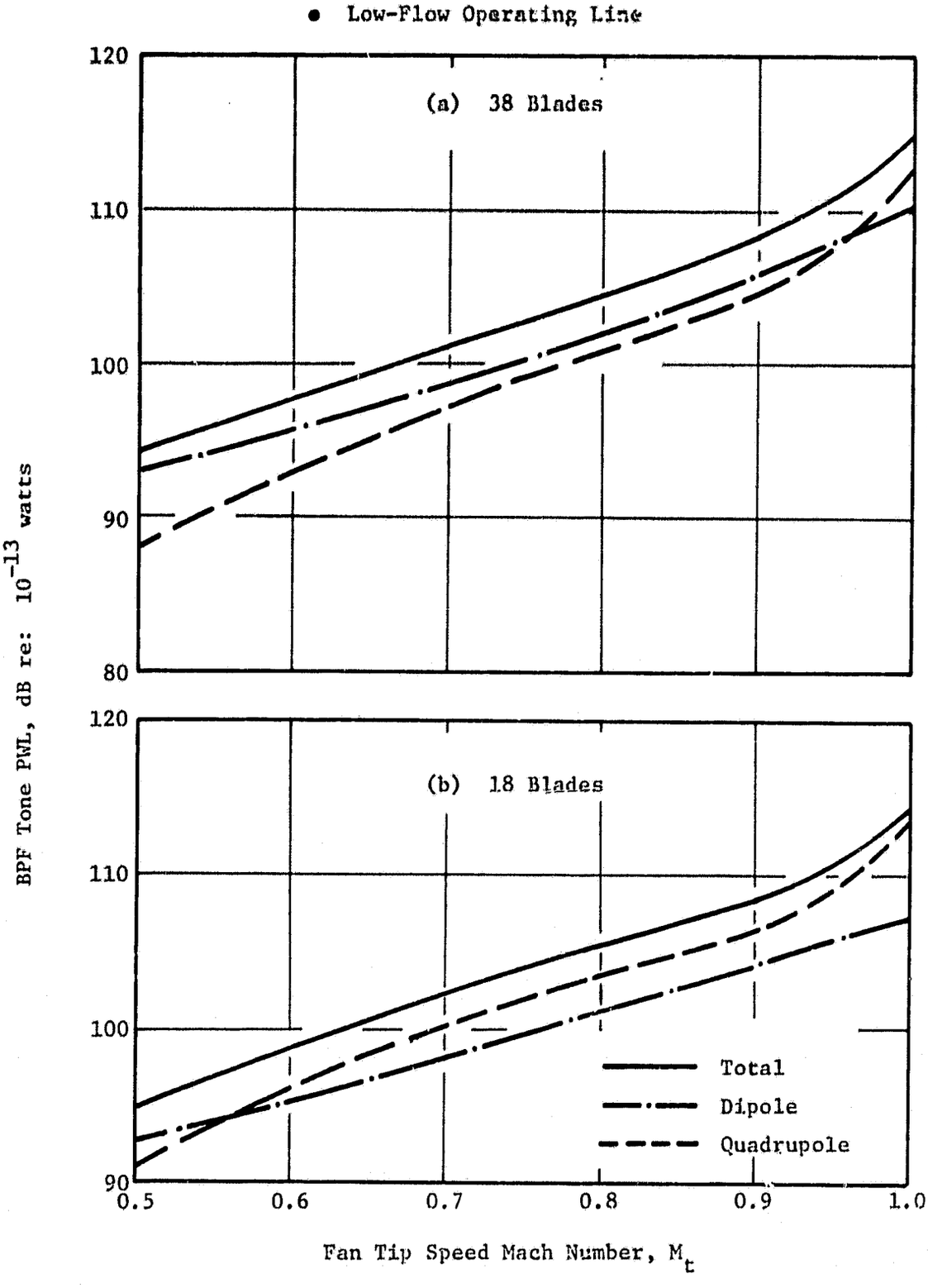

Figure 33. Component Source Contributions to BPF Tone PWL for Quarter-Scale Fans in NASA-Ames 40 x 80 Wind Tunnel at 80 Knots.

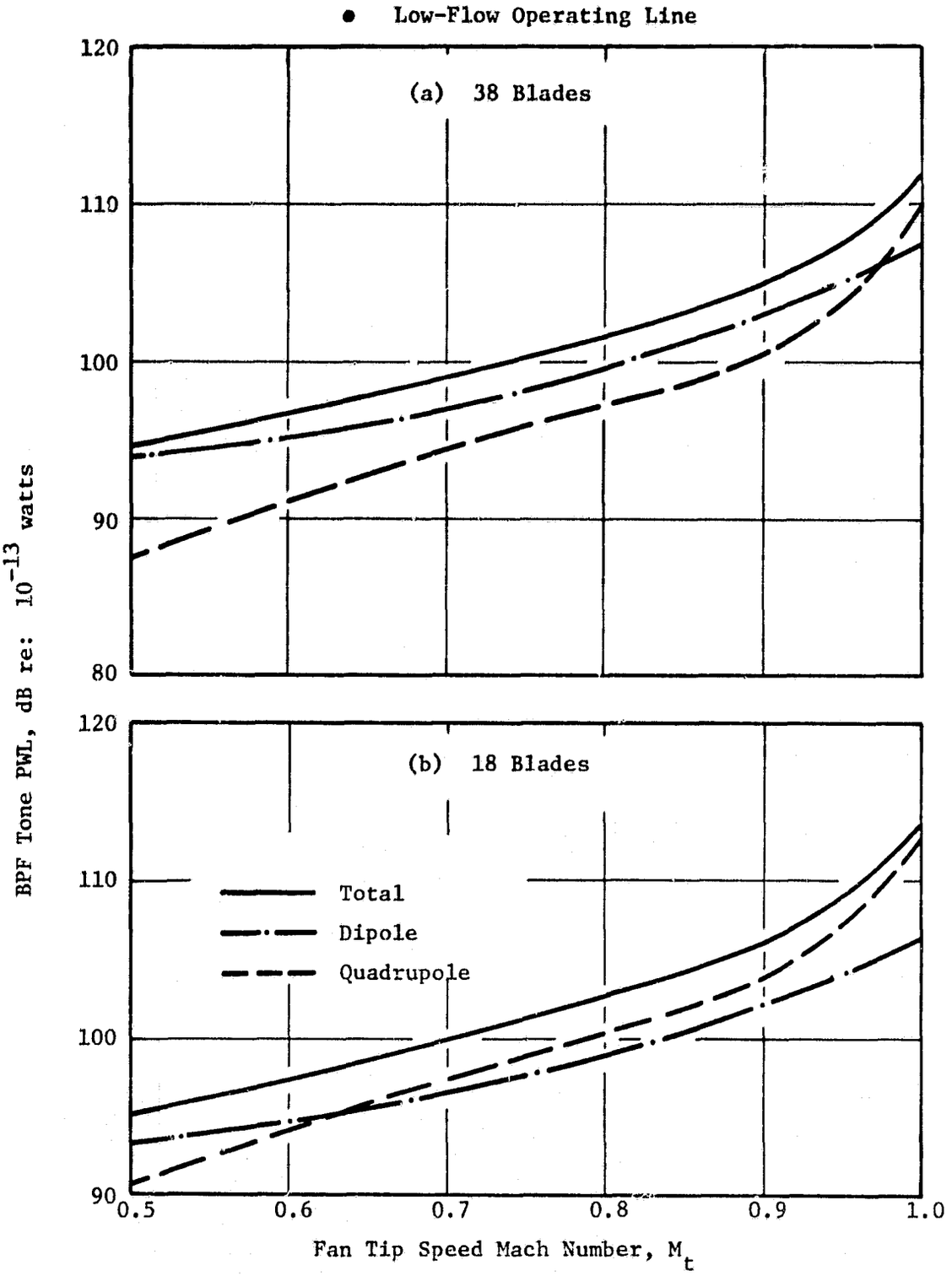

Figure 34. Component Source Contributions to BPF Tone PWL for Quarter-Scale Fans in NASA-Ames 40 x 80 Wind Tunnel at 180 Knots.

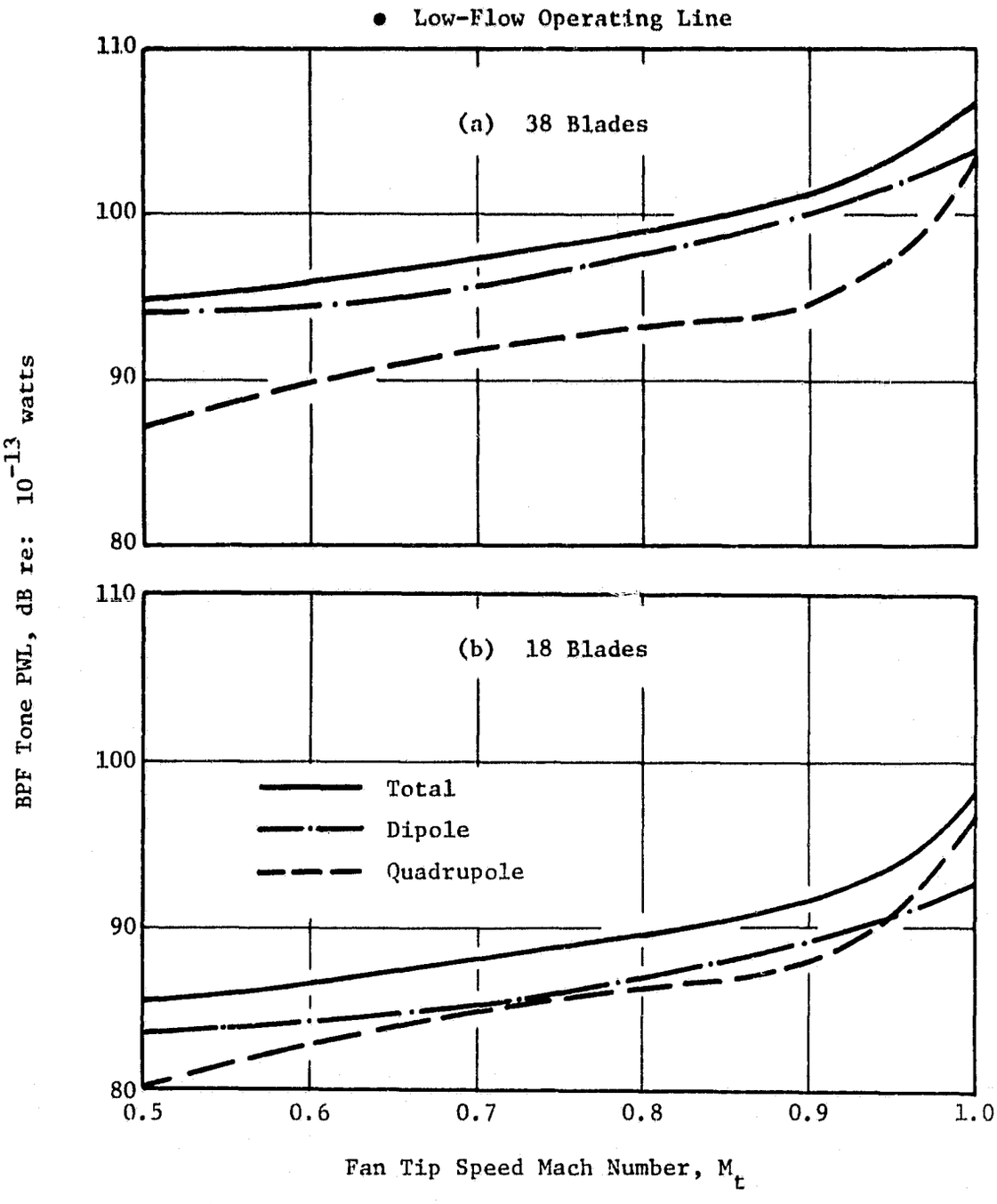

Figure 35. Component Source Contributions to BPF Tone PWL for Quarter-Scale Fans in Flight Environment at 180 Knots.

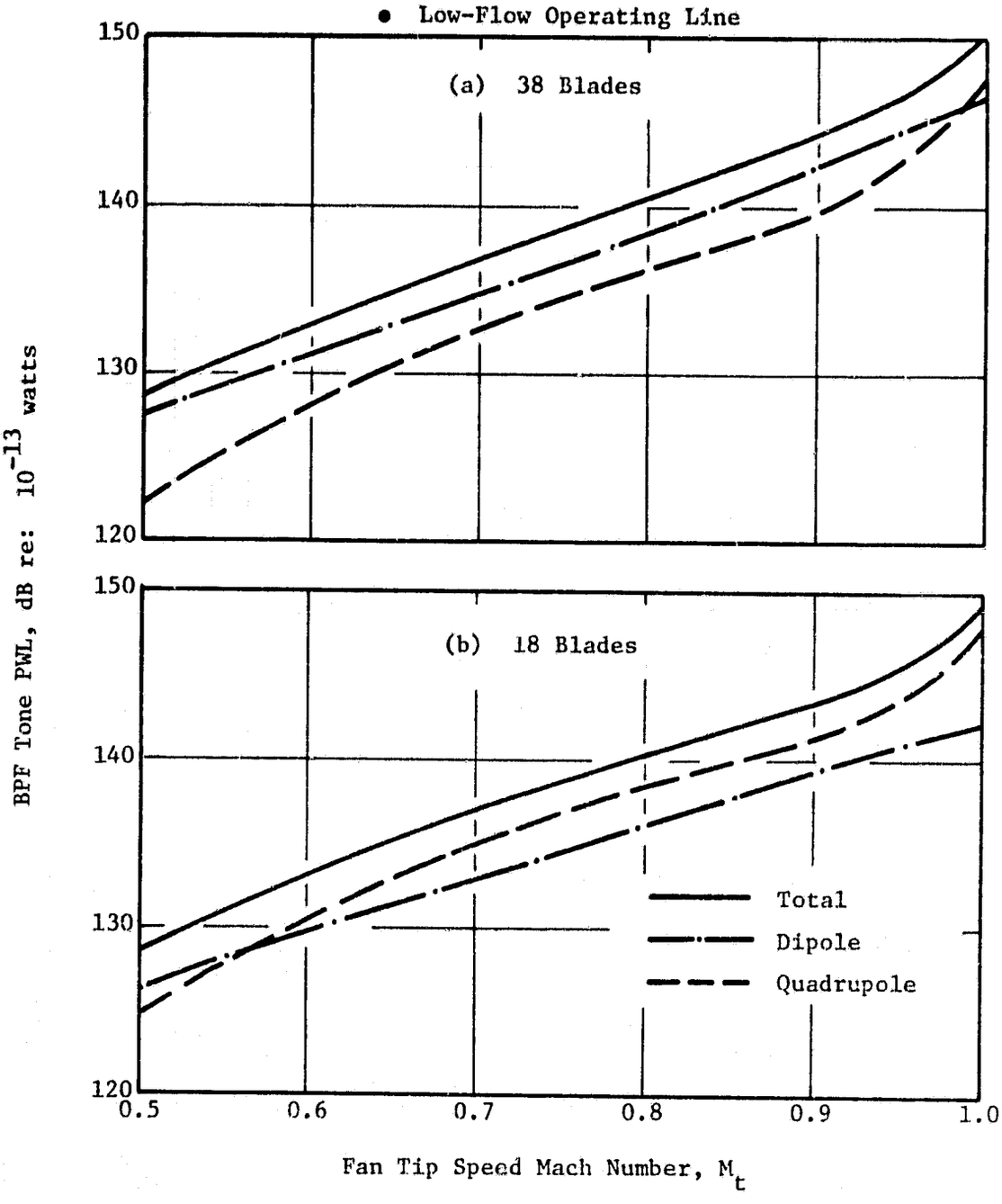

Figure 36. Component Source Contributions to BPF Tone PWL for Full-Scale Fans in Outdoor Test Stand Environment.

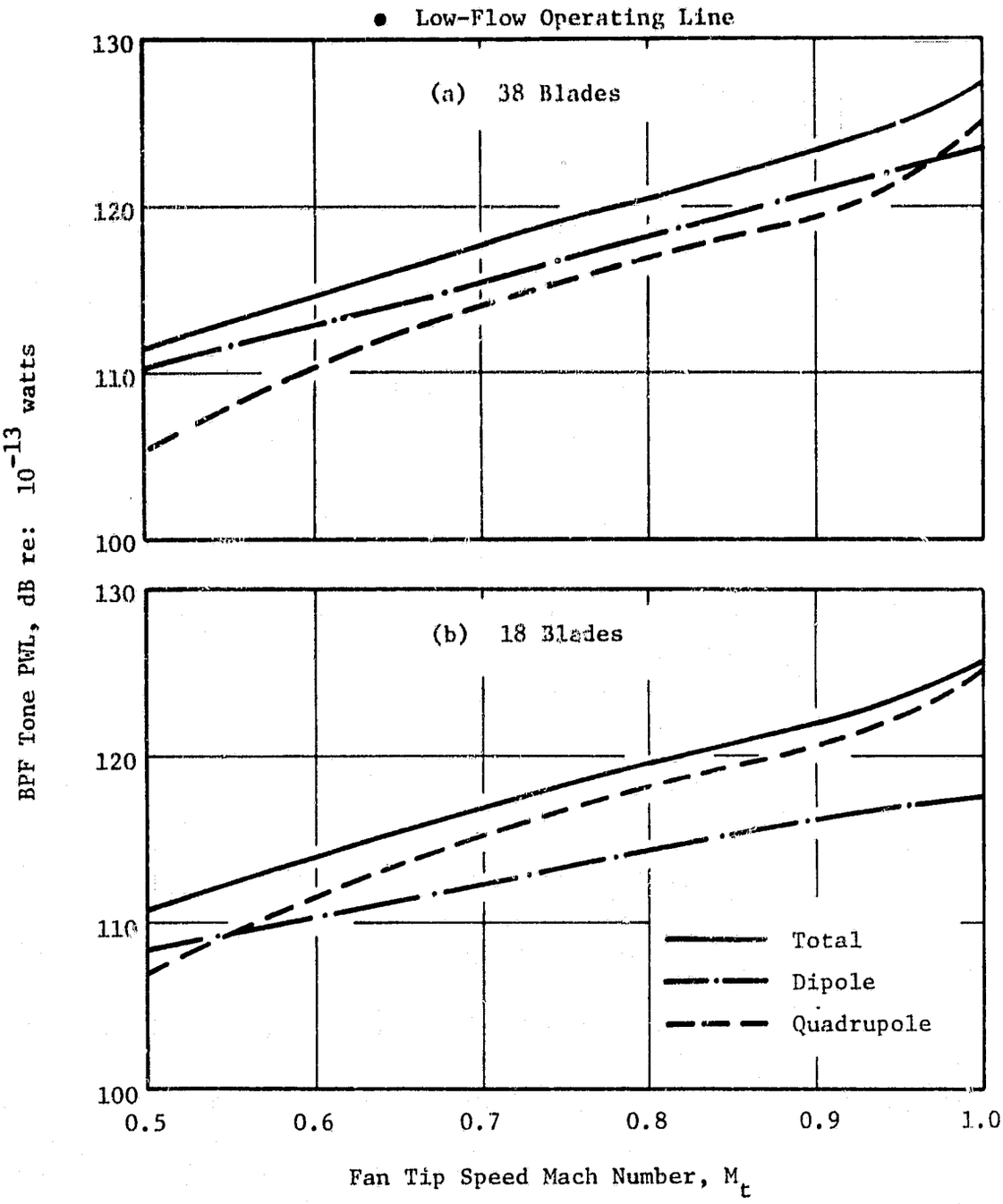

Figure 37. Component Source Contributions to BPF Tone PWL for Full-Scale Fans in NASA-Ames 40 x 80 Wind Tunnel at 80 Knots.

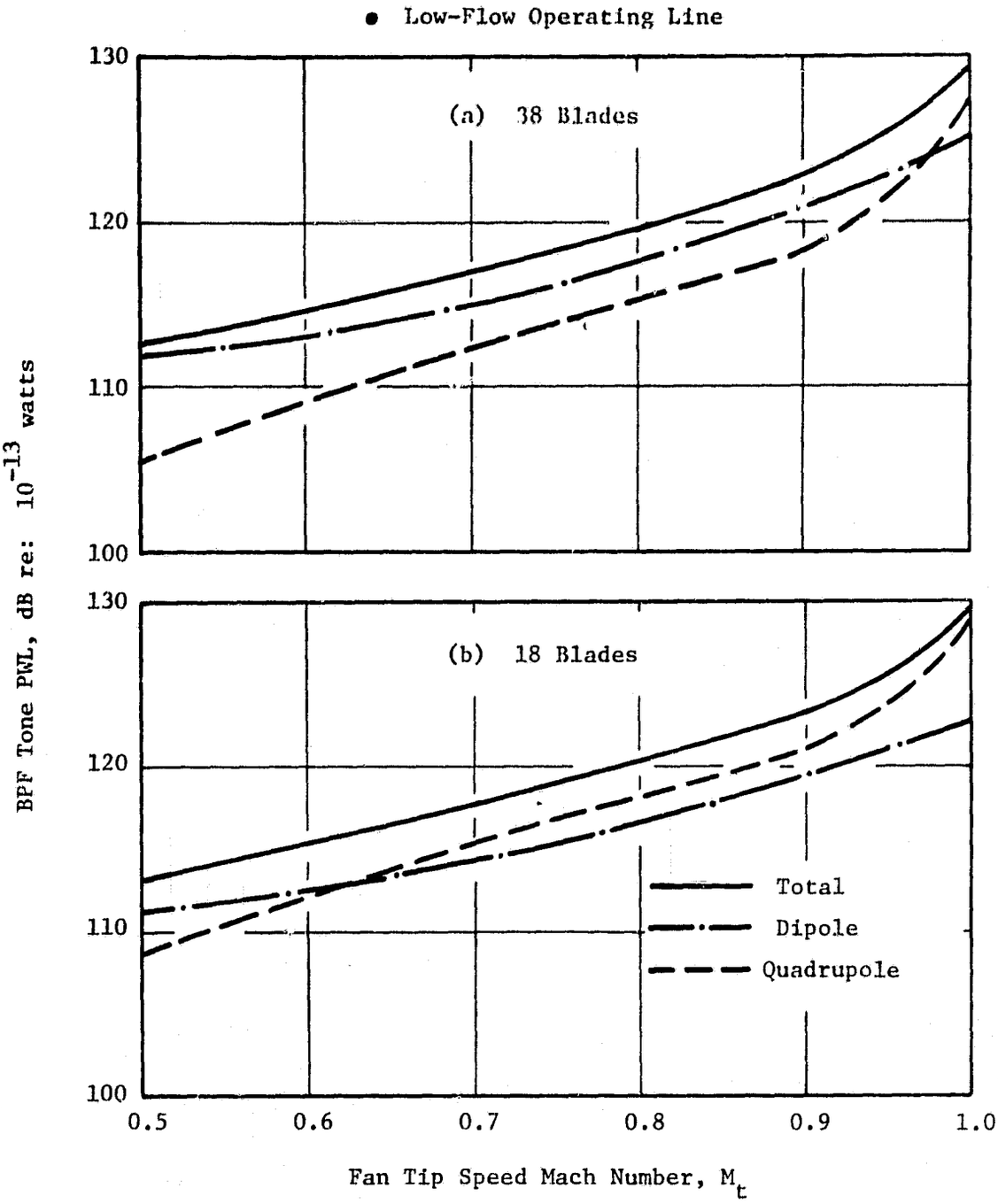

Figure 38. Component Source Contributions to BPF Tone PWL for Full-Scale Fans in NASA-Ames 40 x 80 Wind Tunnel at 180 Knots.

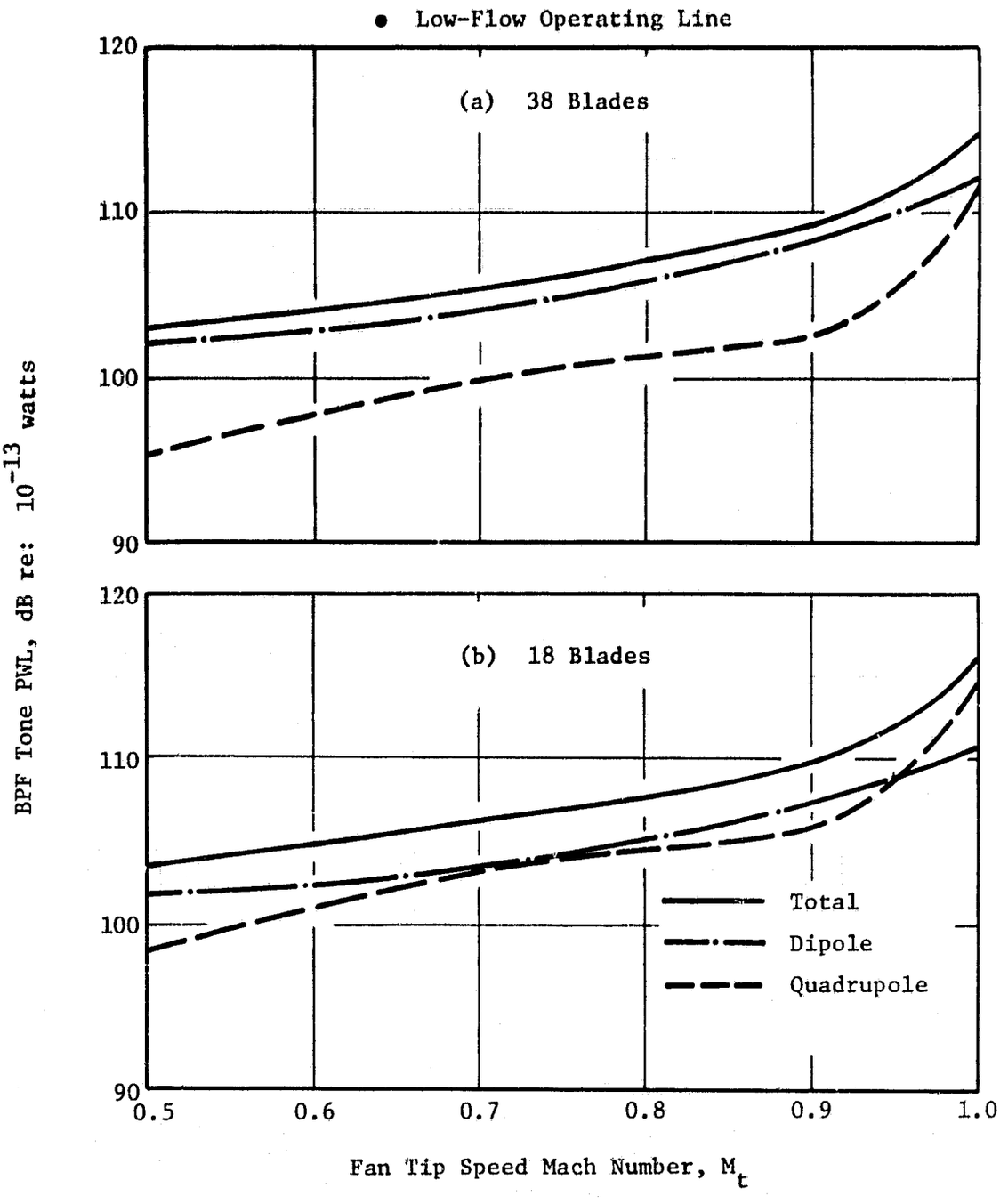

Figure 39. Component Source Contributions to BPF Tone PWL for Full-Scale Fans in Flignt Environment at 180 Knots.

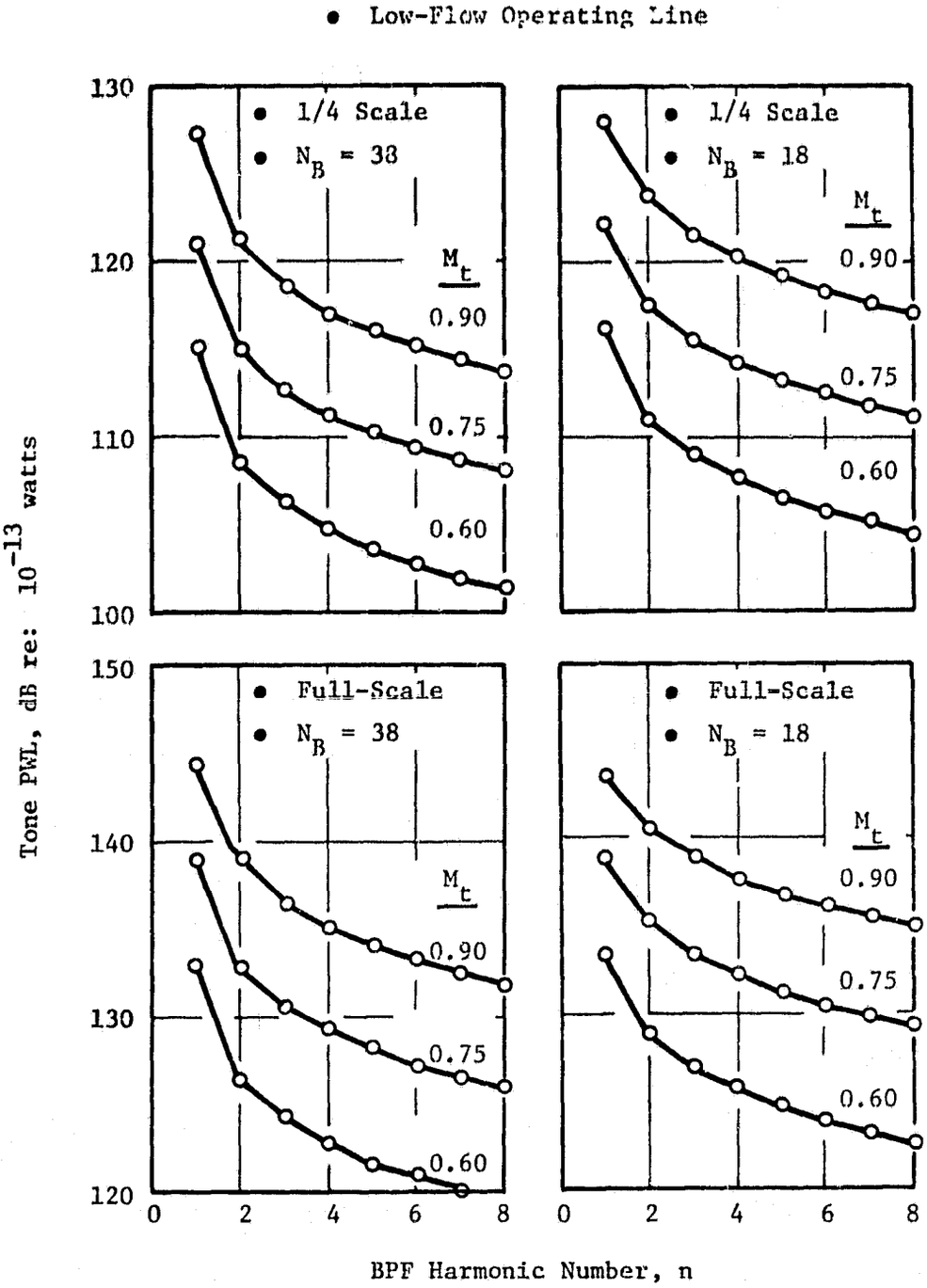

Figure 40. Tone PWL Spectra for Several Fans in Outdoor Test Stand Environment.

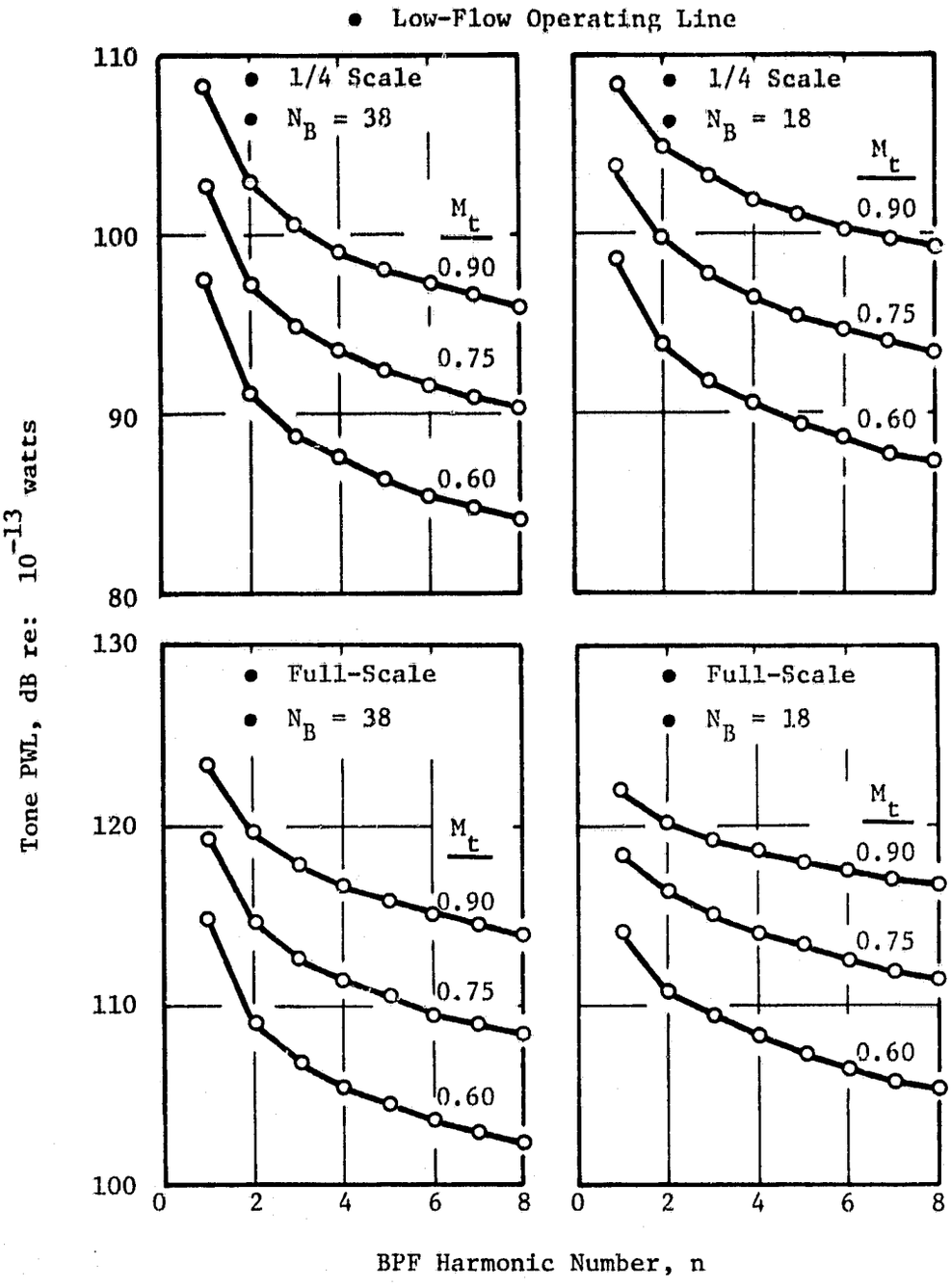

Figure 41. Tone PWL Spectra for Several Fans in NASA-Ames 40 x 80 Wind Tunnel at 80 Knots.

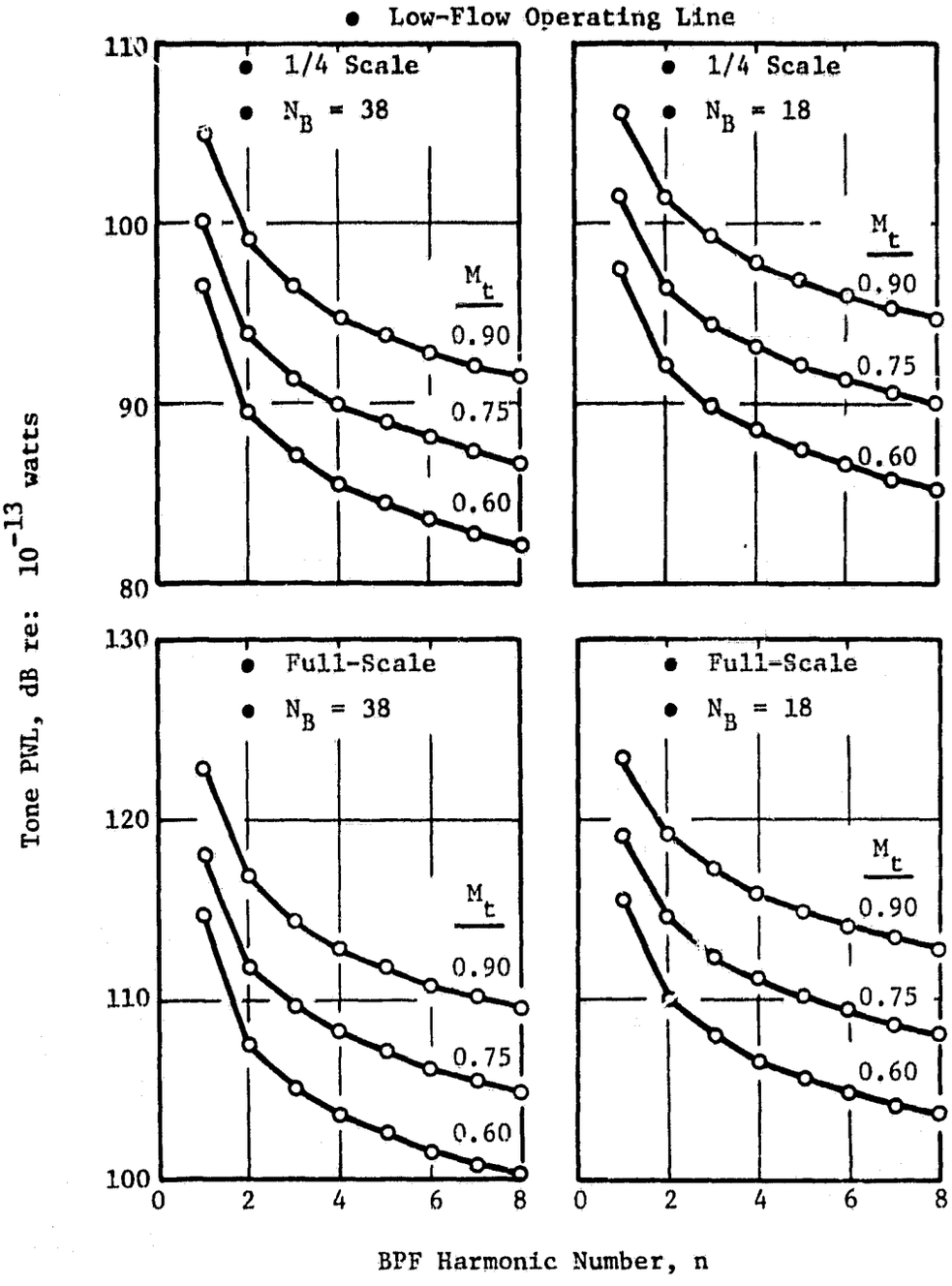

Figure 42. Tone PWL Spectra for Several Fans in NASA-Ames 40 x 80 Wind Tunnel at 180 Knots.

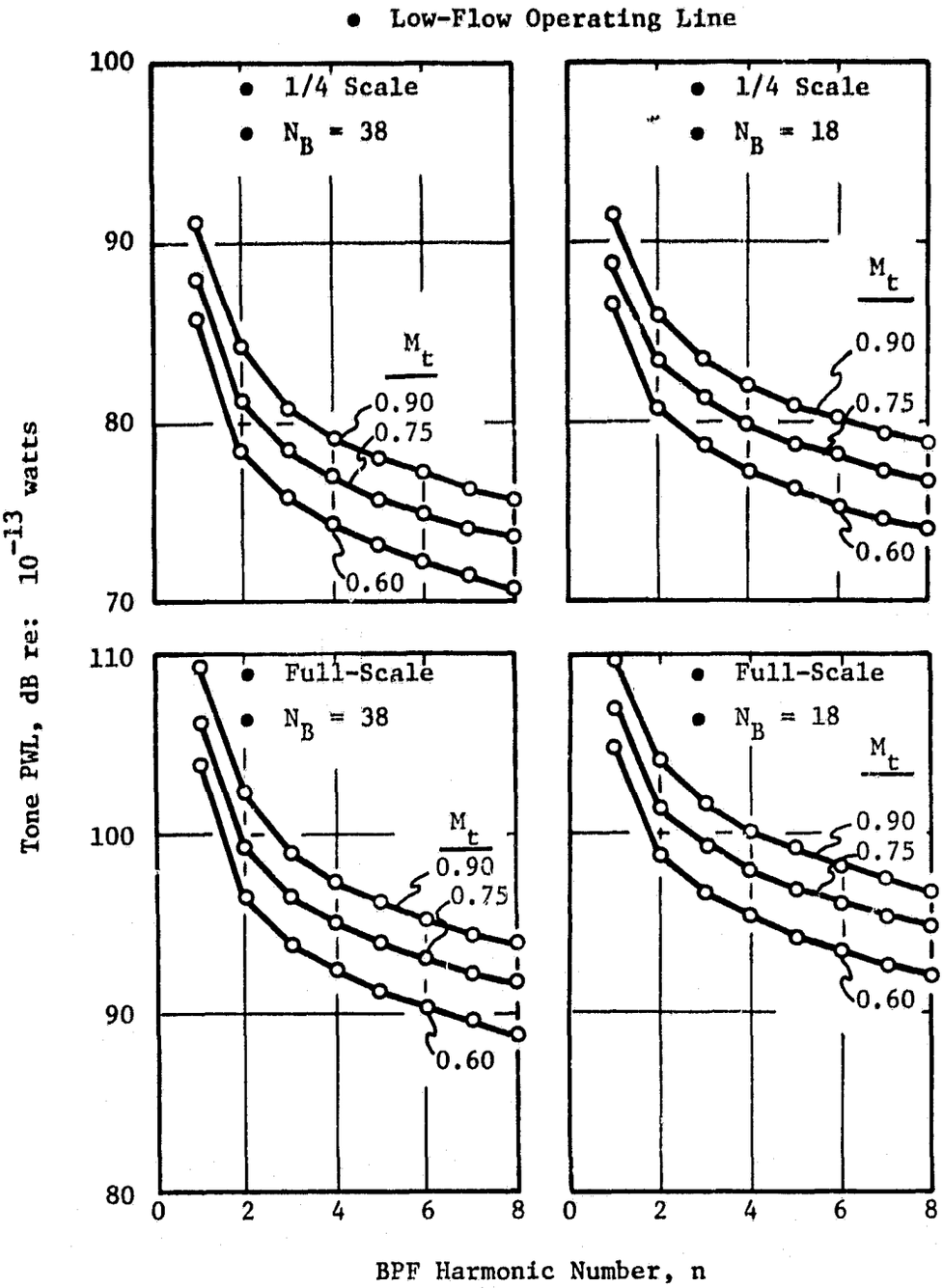

Figure 43. Tone PWL Spectra for Several Fans in Flight Environment at 180 Knots.

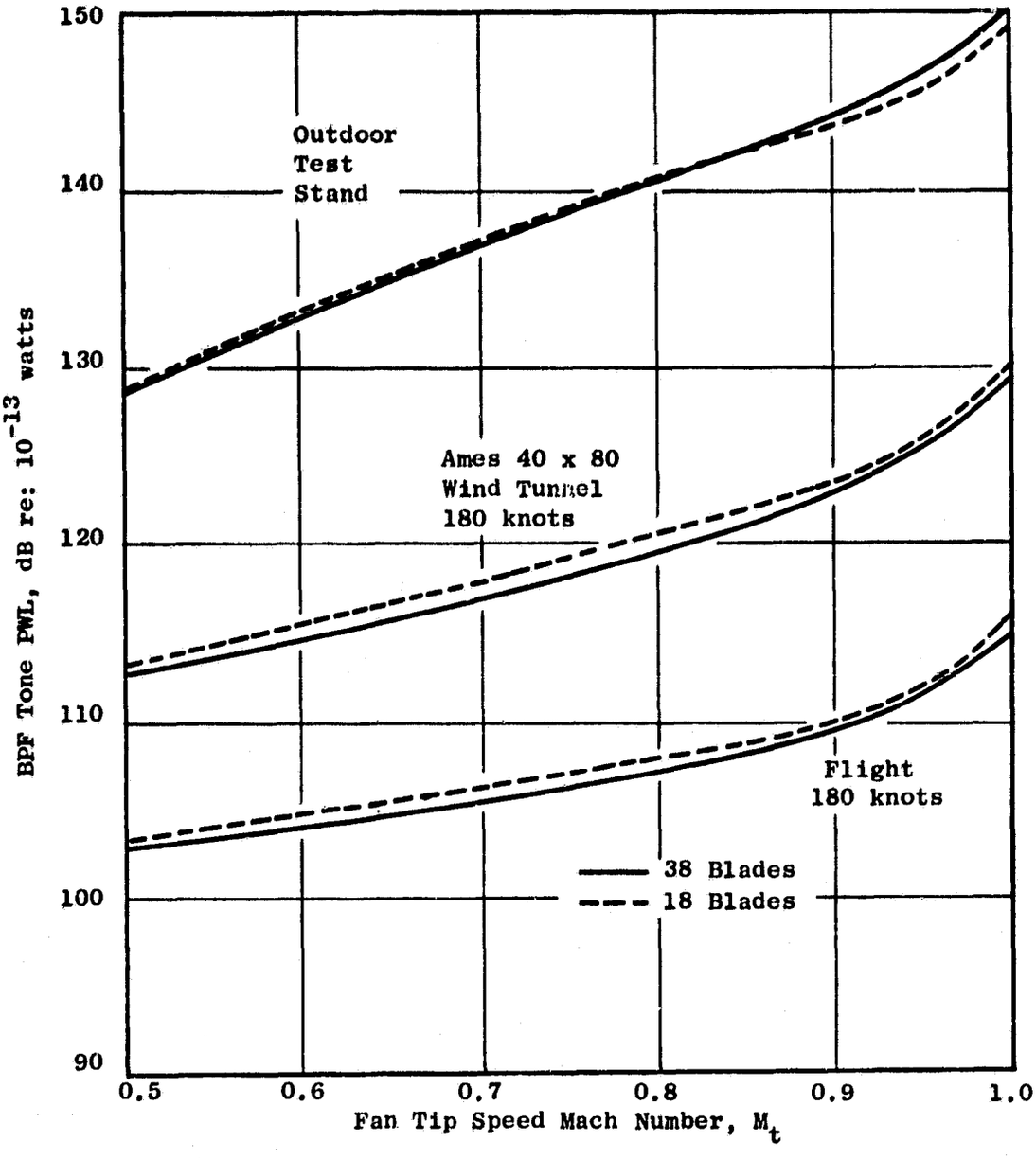

Figure 44. Effect of Blade Number on BPF Tone PWL for Full-Scale Fan on Low-Flow Operating Line.

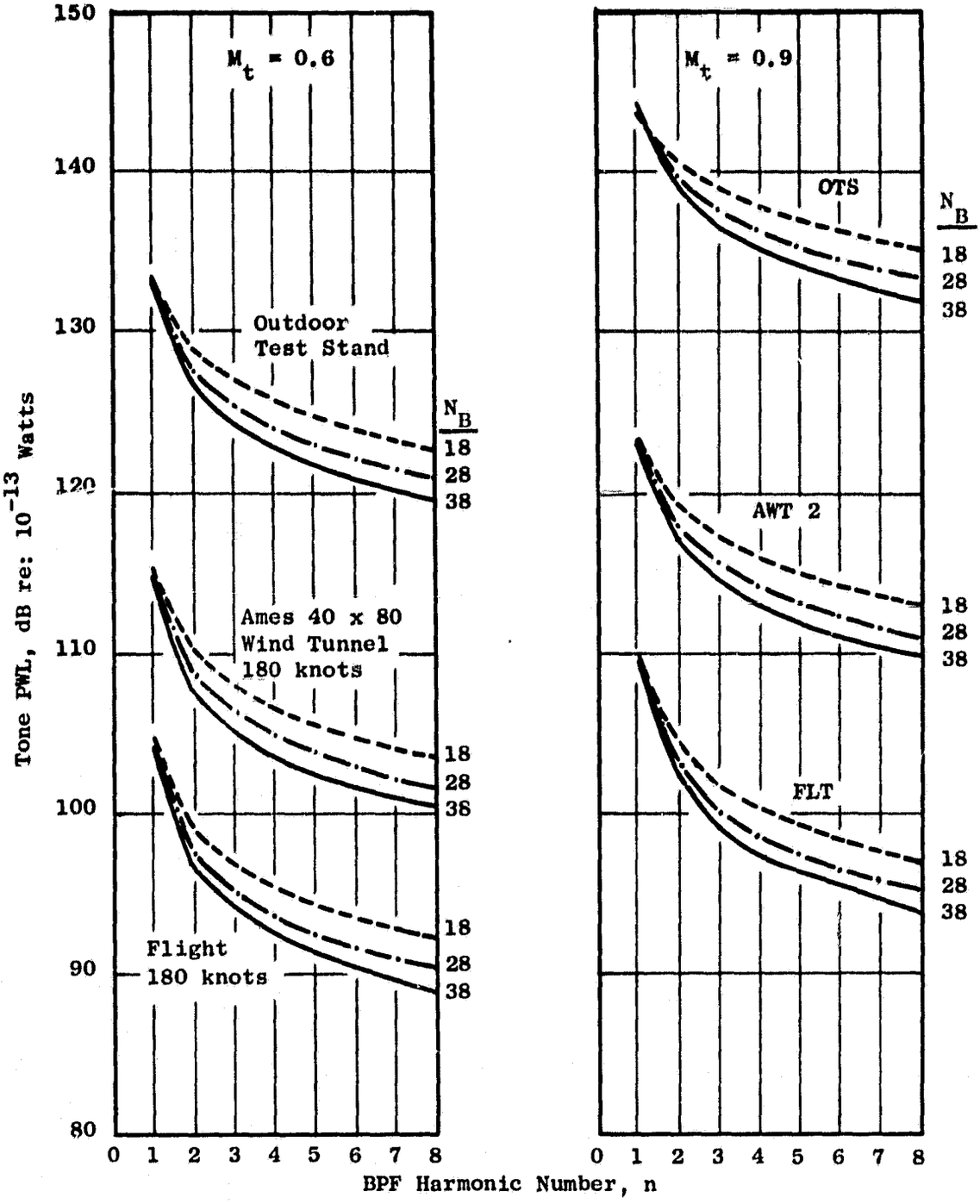

Figure 45. Effect of Blade Number on BPF Harmonic Spectrum for Full-Scale Fan on Low-Flow Operating Line.

Increasing the number of blades for a given solidity decreases the blade spacing and hence increases the tangential length scale-to-blade spacing parameter ℓ_t/s. This results in a noise reduction, as shown in Figure 11. However, increasing the number of blades N_B also increases rotor blade aspect ratio h/c, resulting in a higher unsteady lift amplitude. The dipole noise source will therefore increase, off-setting the decrease due to increasing ℓ_t/s. But the dipole source only dominates at BPF (Figure 31), so the net result is little or no change in noise with N_B at BPF but decreasing noise with increasing N_B at second harmonic (n=2) and higher frequencies.

7.3 EFFECT OF FAN SIZE

To show explicitly the effect of fan size, some of the predictions were normalized with respect to fan rotor inlet area by subtracting 10 $\log_{10}$ (A/A_{ref}) from predicted noise levels, where A_{ref} is a reference area, taken arbitrarily to be 1 m^2. The BPF tone PWL results normalized in this fashion are shown in Figure 46. The corresponding spectra are shown in Figure 47. The major observation to be made is that size does make a difference, i.e., rotor/turbulence noise does not scale with fan area unless the turbulence scales are changed in proportion to the fan diameter change.

The results shown in Figures 46 and 47 show that the smaller fans yield less noise than the area reduction effect can account for, by 5-10 dB. This again is related to the difference in ℓ_t/s which occurs because the turbulence scales (ℓ_t) remain the same while the geometric scales (s) decrease with decreasing fan size.

7.4 EFFECT OF OPERATING LINE

Comparisons were made of rotor/turbulence noise of full-scale fans with 18 blades for two operating lines: (1) the low-flow (LF) line of Figure 28 for typical high tip speed fans, and (2) the high-flow (HF) operating line of Figure 28 for typical subsonic tip speed fans such as the QCSEE fan. The BPF tone PWL comparisons are shown in Figure 48, while the spectral comparisons are shown in Figure 49. It is seen from these results that, at a given tip speed Mach number, the HF fan is noisier than the LF fan.

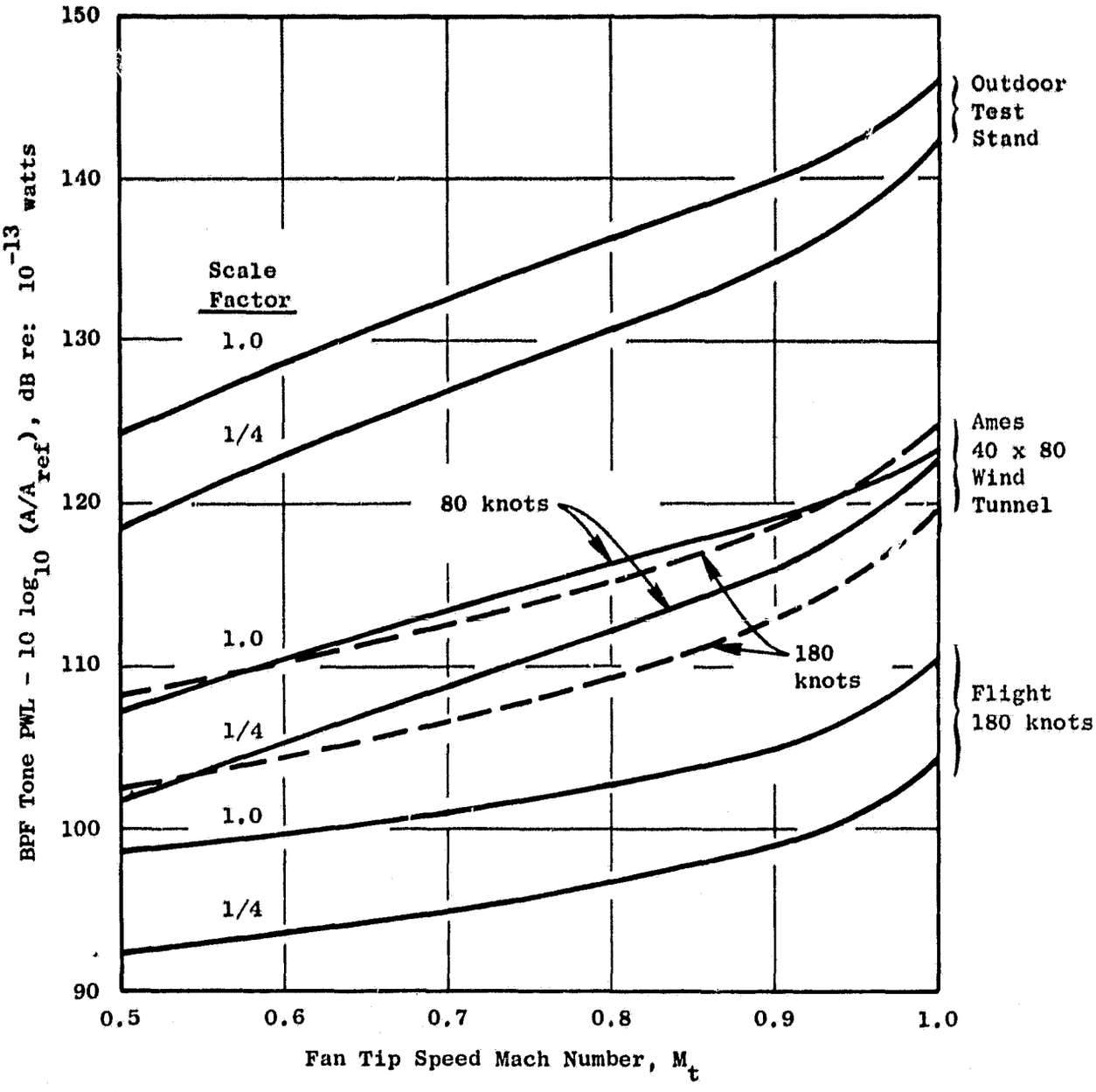

Figure 46. Effect of Fan Size on BPF Tone PWL for 38-Blade Fans on Low-Flow Operating Line.

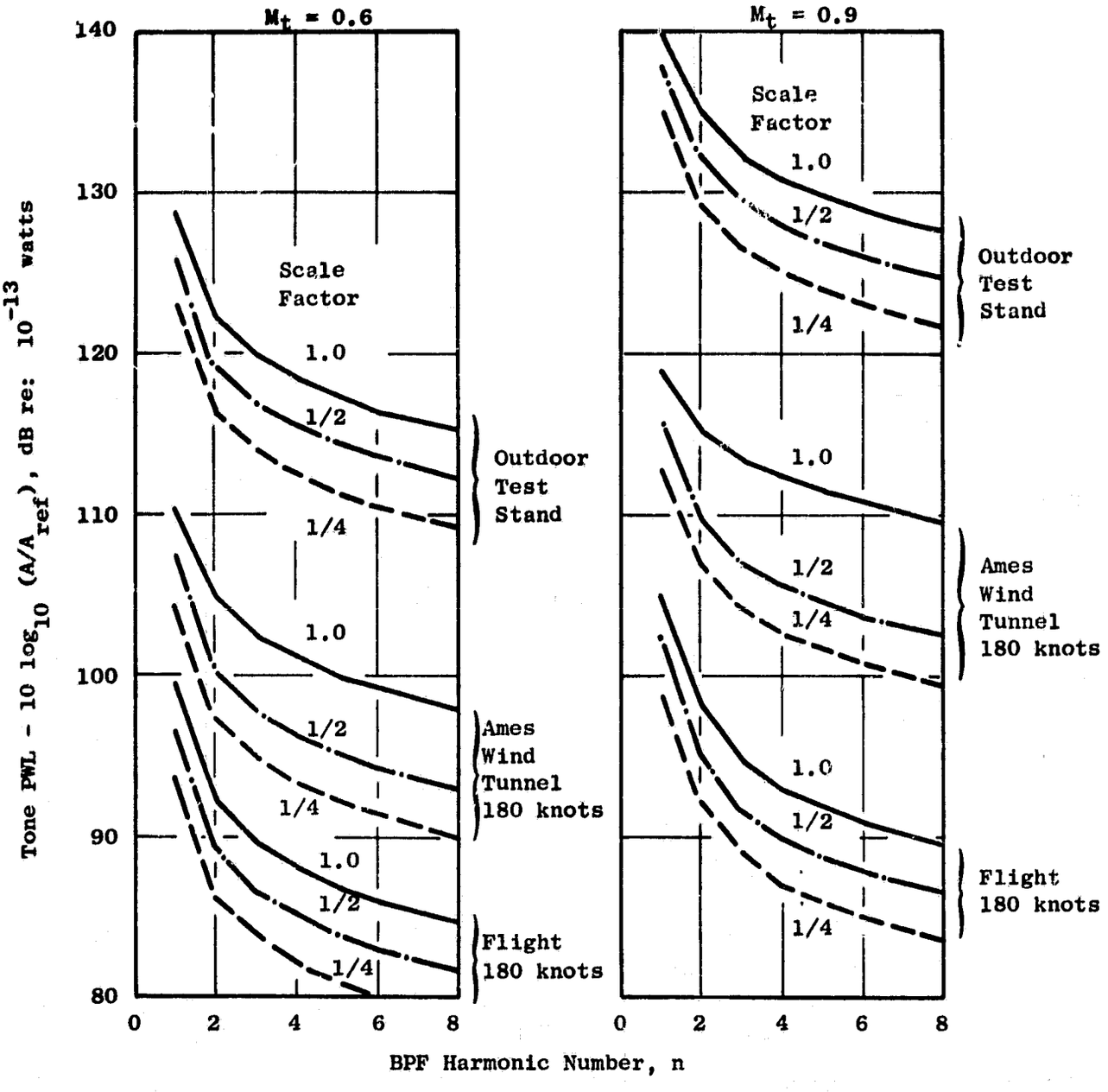

Figure 47. Effect of Fan Size on Tone PWL Spectrum for 38-Blade Fans on Low-Flow Operating Line.

C-2

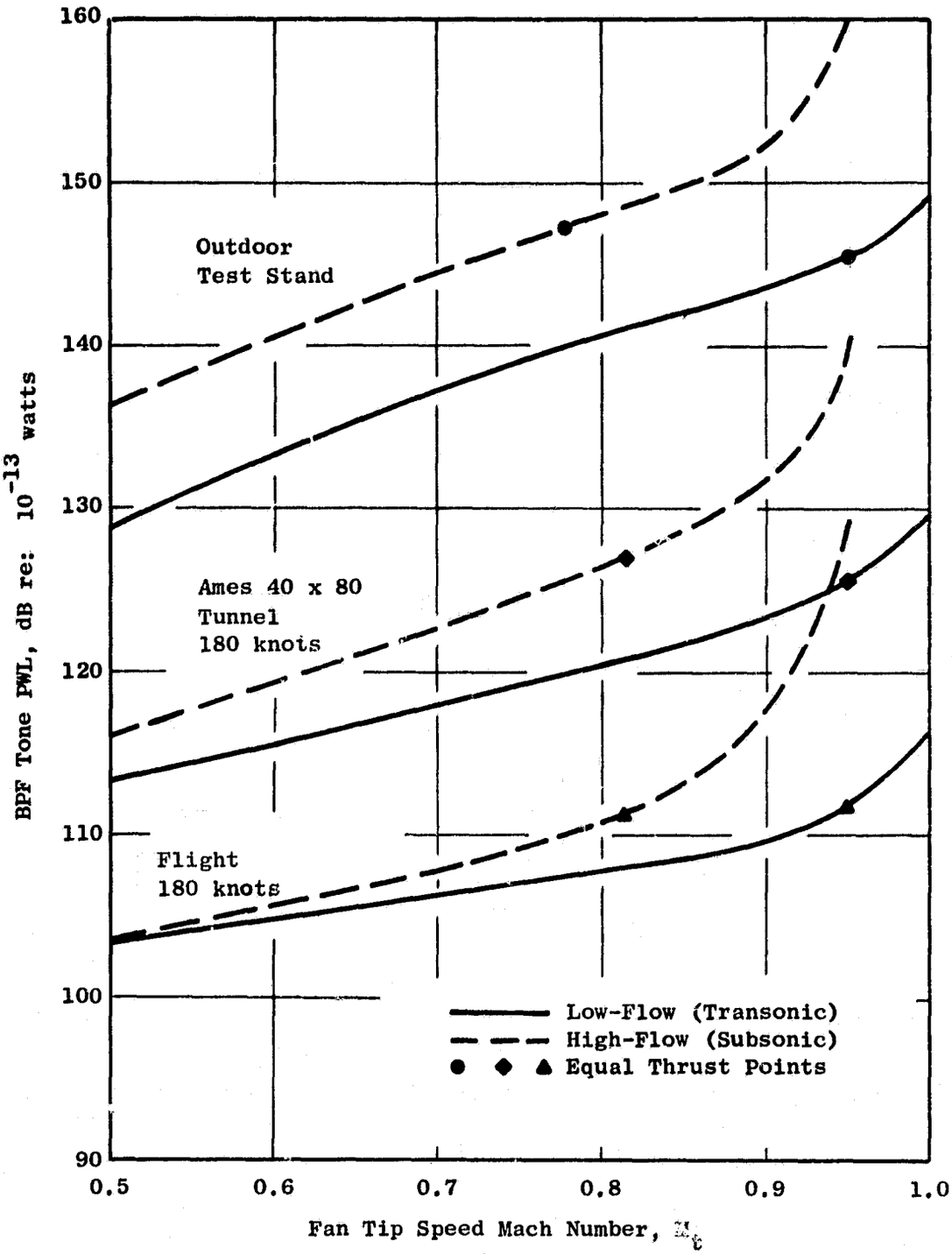

Figure 48. Effect of Operating Line on BPF Tone PWL for Full-Scale 18-Blade Fans.

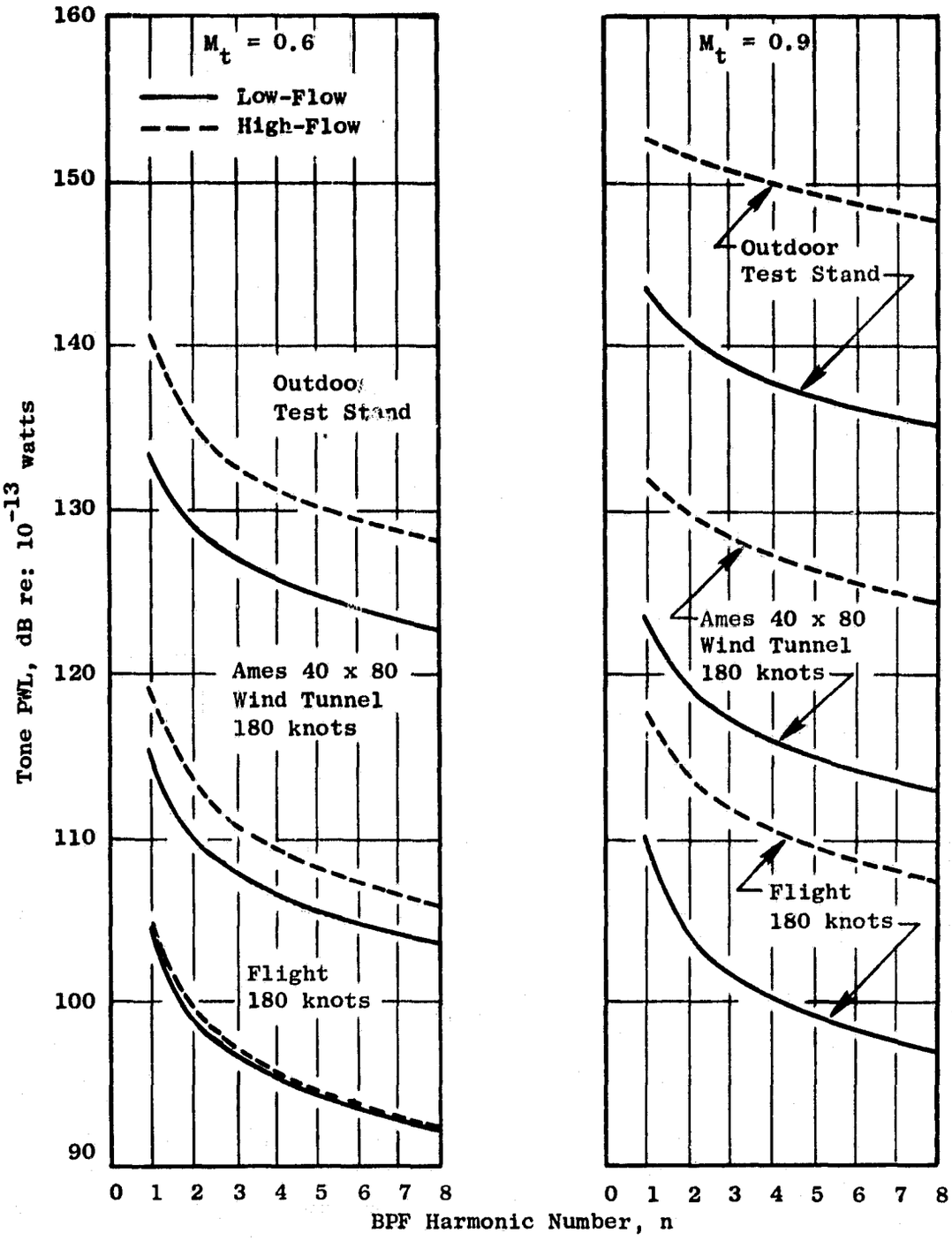

Figure 49. Effect of Operating Line on Tone PWL Spectrum for Full-Scale 18-Blade Fans.

The higher inlet relative Mach number for the high-flow fan is responsible for some of the noise differences shown in Figure 48. Assuming the noise to be proportional to M_r^6, a 3 dB higher noise level would be expected for the HF fan based on Mach number level differences alone. The aspect ratio for the HF fan is higher because of the lower tip solidity, see Table 6. The unsteady lift is therefore higher for the HF fan. The aspect ratio effect alone is estimated to be 3.0 - 3.7 dB for this case. These effects account for most all of the differences shown in Figure 48 for the Outdoor Test Stand.

For the Ames Wind Tunnel and Flight conditions, however, the higher axial Mach number for the HF fan gives a larger contraction ratio at a given tip speed. This has the effect of reducing the tangential length scale (ℓ_t/s), which increases the noise. However, it is also in the direction of reducing turbulence intensity at the fan face, which decreases the noise. The latter effect apparently overshadows the decreased-scale effect, since the HF fan and LF fan noise levels are nearly the same at low tip speeds. The rapid divergence near $M_t = 0.9$ between the two operating-line curves is due to the fact that for the HF fan the rotor inlet relative Mach number is approaching unity at these high speeds, causing the quadrupole source contributions to become disproportionately high as they approach their singularity point.

The HF fan will produce more propulsive thrust at a given tip speed than the LF fan, because the flow is higher and the pressure ratio is the same. It is therefore of interest to compare the HF fan with the LF fan at the same thrust. For a typical LF fan approach power tip speed Mach number of $M_t = 0.95$, the static gross thrust (based on fan exhaust momentum) is 85,975 N (19,329 lb_f). The corresponding net thrust at 180 knots flight speed (gross thrust minus ram drag) is 51,735 N (11,631 lb_f). The equivalent thrust tip speeds for the HF fan occur at $M_t = 0.78$ and $M_t = 0.815$ for the static and 180 knots cases, respectively. These equivalent thrust points are indicated on Figure 48 by closed symbols. It can be seen that the HF fan and LF fan rotor/turbulence noise levels are approximately the same at the same thrust.

8.0 NASA-AMES 40x80 FOOT WIND TUNNEL EVALUATION

Based on the results of the parametric study discussed in the preceding section, an evaluation of the NASA-Ames 40x80 ft Wind Tunnel was carried out to assess the range of fan geometries, operating speeds, and tunnel speeds over which the Ames tunnel adequately simulates flight conditions as far as rotor/ turbulence noise is concerned. The objective was to define the operational/ geometric boundaries for adequate flight simulation.

Before carrying out the evaluation, an assessment of the wind-tunnel rotor/turbulence noise prediction level variability was made to establish an uncertainty band in predicted levels. As discussed in the preceding sections, there is an uncertainty associated with taking turbulence properties measured 8-10 fan diameters upstream of the engine and projecting these to fan rotor inlet values using the sudden-contraction theory of Reference (5). One extreme is to assume that the sudden-contraction theory is correct, which qualitatively gives

$$(u_a/U_a)_{fan} \sim (u_a/V_o)_{up} \cdot C^{-2}$$

and

$$(u_t/U_a)_{fan} \sim (u_t/V_o)_{up} \cdot C^{-1/2}$$

Thus both axial and transverse intensities are lower after the contraction. This assumption gives the lower bound in noise predictions. The other extreme is to assume that the intensities do not change at all across the contraction (e.g., as in Reference 24), so that

$$(u_a/U_a)_{fan} = (u_a/V_o)_{up} \text{ and } (u_t/U_a)_{fan} = (u_t/V_o)_{up}$$

This gives an upper bound on the noise predictions. Now across a contraction, u_a will decrease by some amount and u_t will increase. In any case, u_t will be substantially larger than u_a, and hence the noise level will be primarily governed by the variations in u_t and variations in u_a will have little or no effect. An estimate of the difference between the upper and lower bound limits can therefore be made by noting (Reference 2) that the noise varies as the square of the turbulence intensity. Defining ΔPWL as the

difference between upper and lower bound predictions, where subscripts A and B refer to precontraction and postcontraction values, we can assume that

$$\Delta PWL \approx -20 \log_{10} \frac{(u_t)_B / U_a}{(u_t)_A / V_o} = 20 \log_{10} \frac{C}{f(C)} \qquad (26)$$

The numerator in Equation 26 represents the lower bound value of transverse intensity at the fan face given by sudden contraction theory, while the denominator represents the upper bound value corresponding to no change in intensity. Equation 26 was used to estimate the difference in calculated noise levels between the above two assumptions concerning contraction effects. Also, calculations were made over a range of tunnel speeds using the computer program directly; first with the sudden-contraction theory, and second with $(u_t/U_a)_B = (u_t/V_o)_A$. The difference between the two calculated levels was compared with the estimated difference given by Equation 26 above, and the agreement was within ±0.5 dB.

Equation 26 is shown plotted in Figure 50, along with range of contraction ratios encountered in this study for typical fan designs. It can be seen that the uncertainty band due to contraction effects is about 2-6 dB at V_o = 80 knots over a range of tip speeds $0.5 \leq M_t \leq 1.0$. At 180 knots, the uncertainty band is only 0-2 dB for the tip speed range $0.75 \leq M_t \leq 1.0$. For $M_t < 0.75$ at V_o = 180 knots, the contraction ratio is less than 1.0, i.e., $V_o > U_a$, and the applicability of contraction theory to expanding flows is questionable.

It is emphasized that the uncertainty band given in Figure 50 is not due to variability and/or randomness in the tunnel turbulence properties, but is only due to the uncertainty in the techniques being used to extrapolate that turbulence information to the fan face values. In fact, the same uncertainty applies to the flight case, because upstream atmospheric turbulence characteristics are being extrapolated to fan face values with the same techniques. Also the maximum (6 dB) uncertainty band is less than the tone fluctuation amplitudes usually observed for rotor/turbulence noise (References 21 and 22).

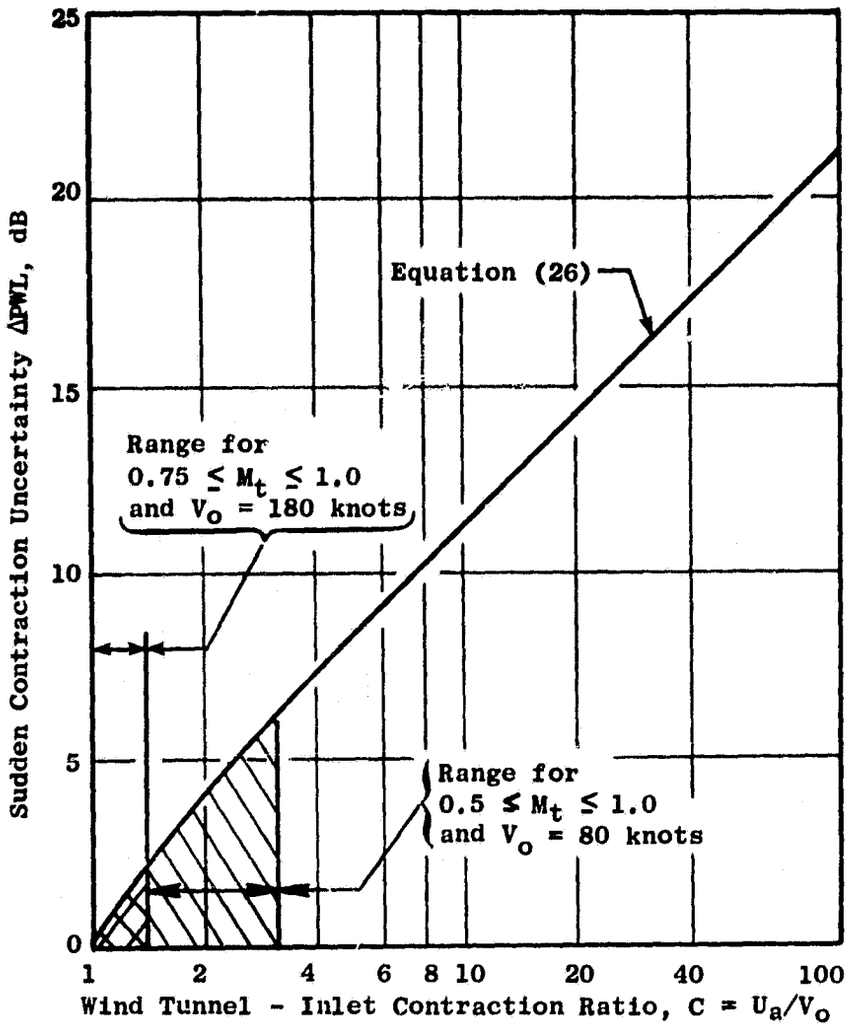

Figure 50. Estimate of Uncertainty in Predicting Rotor/Turbulence Noise from Turbulence Measurements Far Upstream.

The outdoor test stand predictions also have an uncertainty band due to the variability in turbulence properties which are measured at the fan face. For example, measured axial length scales varied from 86 to 259 ft (26 to 79 m) at the GE Peebles, Ohio test facility for one engine test. A parametric calculation of the influence of ℓ_a was made (ℓ_a/ℓ_t held constant) for the full-scale low-flow fan, and these results are shown in Figure 51. From these results, it can be concluded that an uncertainty of +1 dB to -4 dB can exist in predicted Outdoor Test Stand levels due to uncertainty in knowing axial length scale, recalling that a nominal value of ℓ_a = 100 ft (30.5 m) was used for all OTS calculations discussed in the previous section. Also, the measured transverse intensity u_t/U_a varied by a factor of two, implying an additional ±3 dB uncertainty due to variability in u_t/U_a.

To illustrate the above effects, measured values of BPF tone forward-arc PWL on a CF6-50 engine were compared with predicted rotor/turbulence noise tone levels using the above uncertainty estimates to define a band of expected levels. This comparison is shown in Figure 52. Even though the engine had an acoustic suppression liner in the inlet duct whose effect on rotor/turbulence interaction tones is quantitatively unknown, the data is seen to fall within the prediction band.

Finally, the uncertainty in predicted flight rotor/turbulence noise levels must be considered. Houbolt, Reference 25, quotes many data sources, and suggests that a rather alarming variability in atmospheric turbulence conditions can prevail, depending upon the proximity of weather fronts, wind shear, squall lines, thunderstorms, temperature gradients, terrain, etc. Aircraft wake turbulence in the vicinity of airports will introduce variations dependent upon traffic patterns, density and duration. Houbolt estimates the variation in atmospheric turbulence length scales to be 300 to 700 ft (91 to 213 m). A nominal value of 500 ft (152 m) was used in the present study. A parametric calculation of the effect of length scale (precontraction) is shown in Figure 53 for a full-scale, high-flow (18 blades) fan. Again it is seen that the uncertainty in predicted noise levels for the length scale range of 300 to 700 ft is about ±2 dB. Houbolt also states that atmospheric turbulence rms velocities of 3.0 - 3.5 fps are average values, with possible peak "gust" values of 20 times as much. Such extremes are rare and are confined

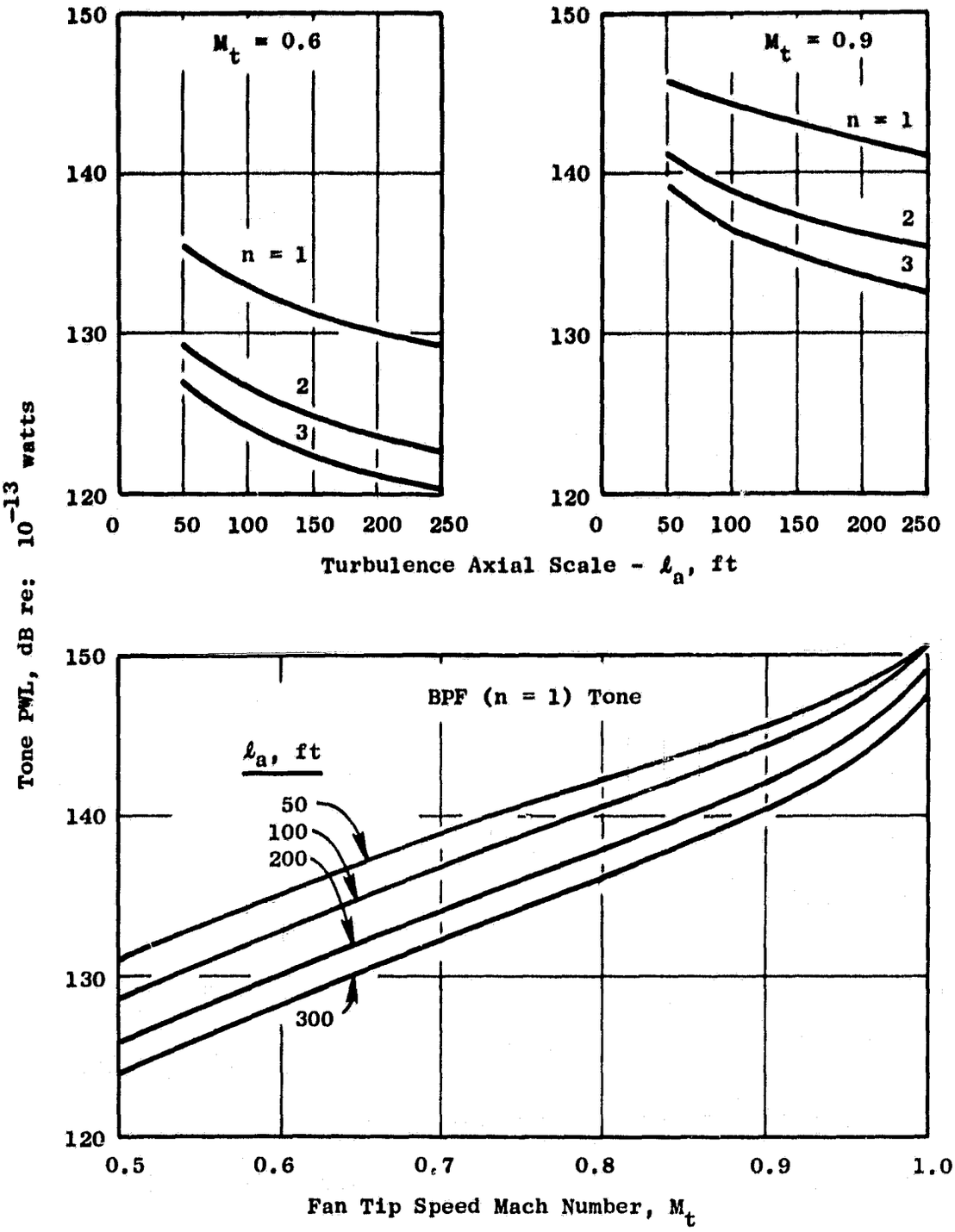

Figure 51. Effect of Axial Length Scale on Predicted Rotor Turbulence Noise Levels for Full-Scale Low-Flow Fan (N_B = 38) in Outdoor Test Stand (ℓ_a/ℓ_t = 250).

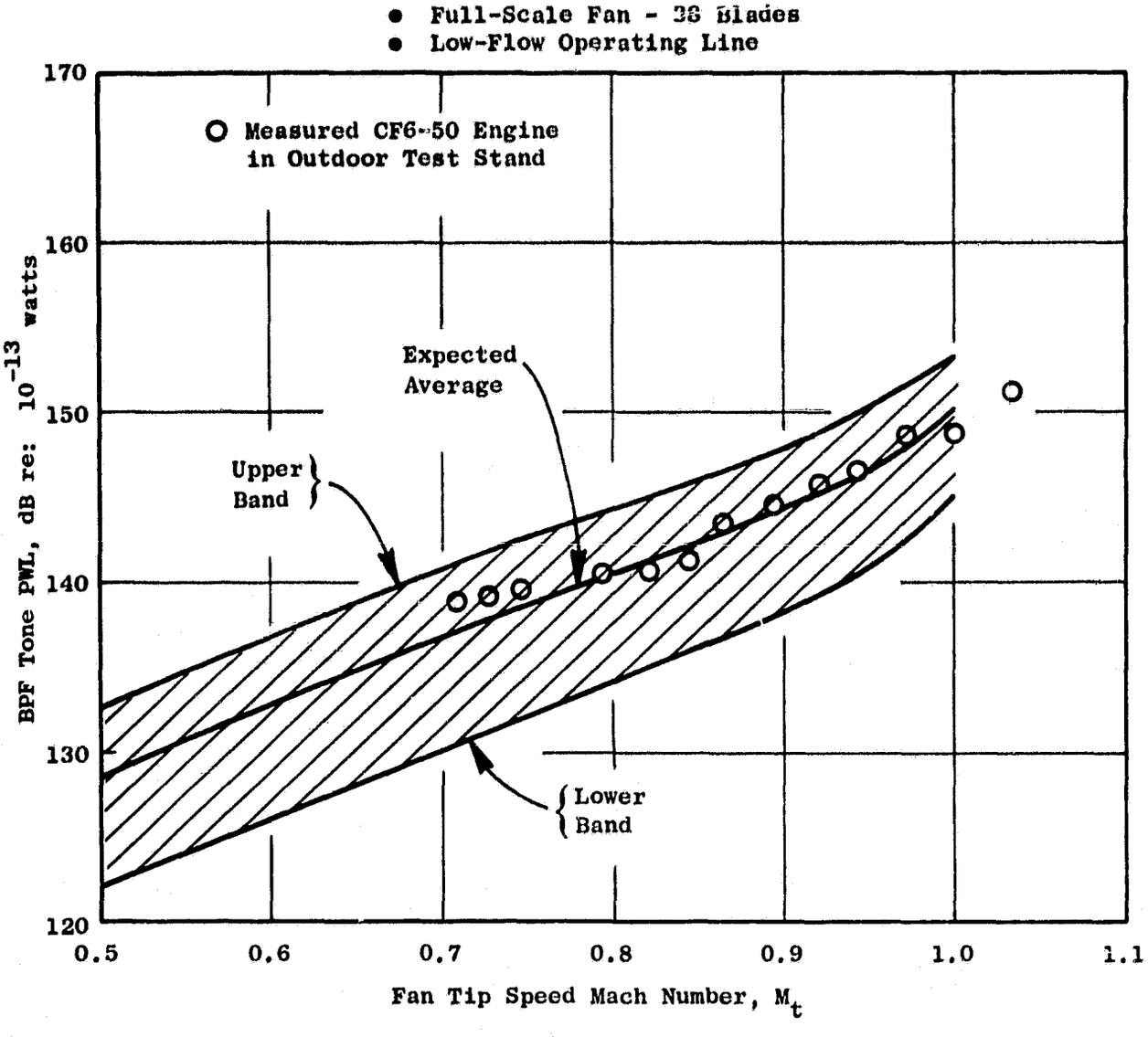

Figure 52. Typical Uncertainty Band in Predicted Outdoor Test Stand Rotor/Turbulence Noise BPF Tone Inlet PWL, and Comparison with Engine Test Data.

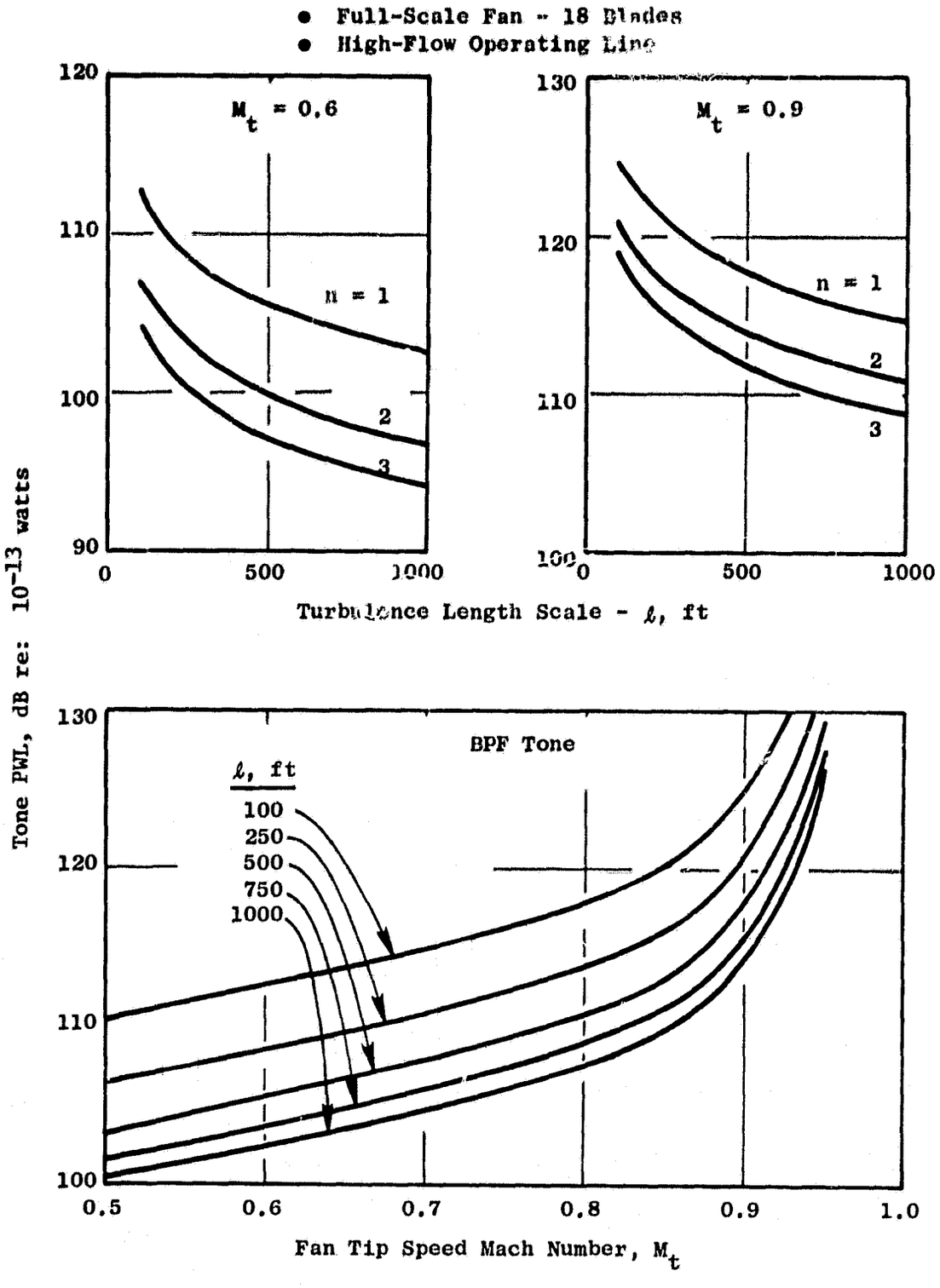

Figure 53. Effect of Variations in Atmospheric Turbulence Length Scale on Flight (V_o = 180 Knots) Rotor/ Turbulence Noise.

to severe weather conditions, but nevertheless highlight the variability that can be expected in rotor/turbulence noise in flight. A 4:1 variation in pre-contraction u_t is not unreasonable in flight, which would then yield a ±6 dB variation in noise. Combined with the ±2 dB uncertainty due to variations in length scale, a total uncertainty band on predicted flight rotor/turbulence noise levels of ±8 dB is the best that can be expected, based on atmospheric turbulence variability from the "expected average" values.

From the results shown in Figures 44 through 49, it is seen that rotor/turbulence noise levels in the Ames 40x80 Wind Tunnel are predicted to be 15-20 dB lower, on the average, than the Outdoor Test Stand levels, but still about 10-15 dB higher than corresponding Flight levels. The question that arises is, are the Wind tunnel levels low enough? To answer this, first recall that the noise level increases with decreasing blade number, and that full-scale fans produce more "noise-per-unit-area" than do scale model fans. If we take into account all of the above uncertainty band limits and consider as the worst case the full-scale 18-blade fan, the comparison of predicted BPF tone levels for the various test conditions would look more like Figure 54, where a band or range of values is shown rather than a single average line. The point to be learned from this figure is that when variability is taken into account, the wind tunnel levels can be as low as flight levels, even though the average line predictions show a 10-15 dB difference. Also, the uncertainty band associated with variability in turbulence properties for the Outdoor Test Stand and Flight conditions is considerably larger than the uncertainty for the Ames 40x80 Wind Tunnel due to extrapolating upstream turbulence characteristics to the fan face conditions.

Another way of assessing the adequacy of the NASA-Ames 40x80 Tunnel for simulating flight turbulence levels is to see how much tone reduction is obtained relative to the fan characteristic broadband level. An empirical method for correlating fan broadband noise was published in Reference 28, and this method was used to correlate the broadband levels of several scale model fan stages, using data with a turbulence control structure in place (Reference 6). The correlations, given in Reference 29, relate the peak broadband noise level to rotor inlet tip relative Mach number M_r and rotor

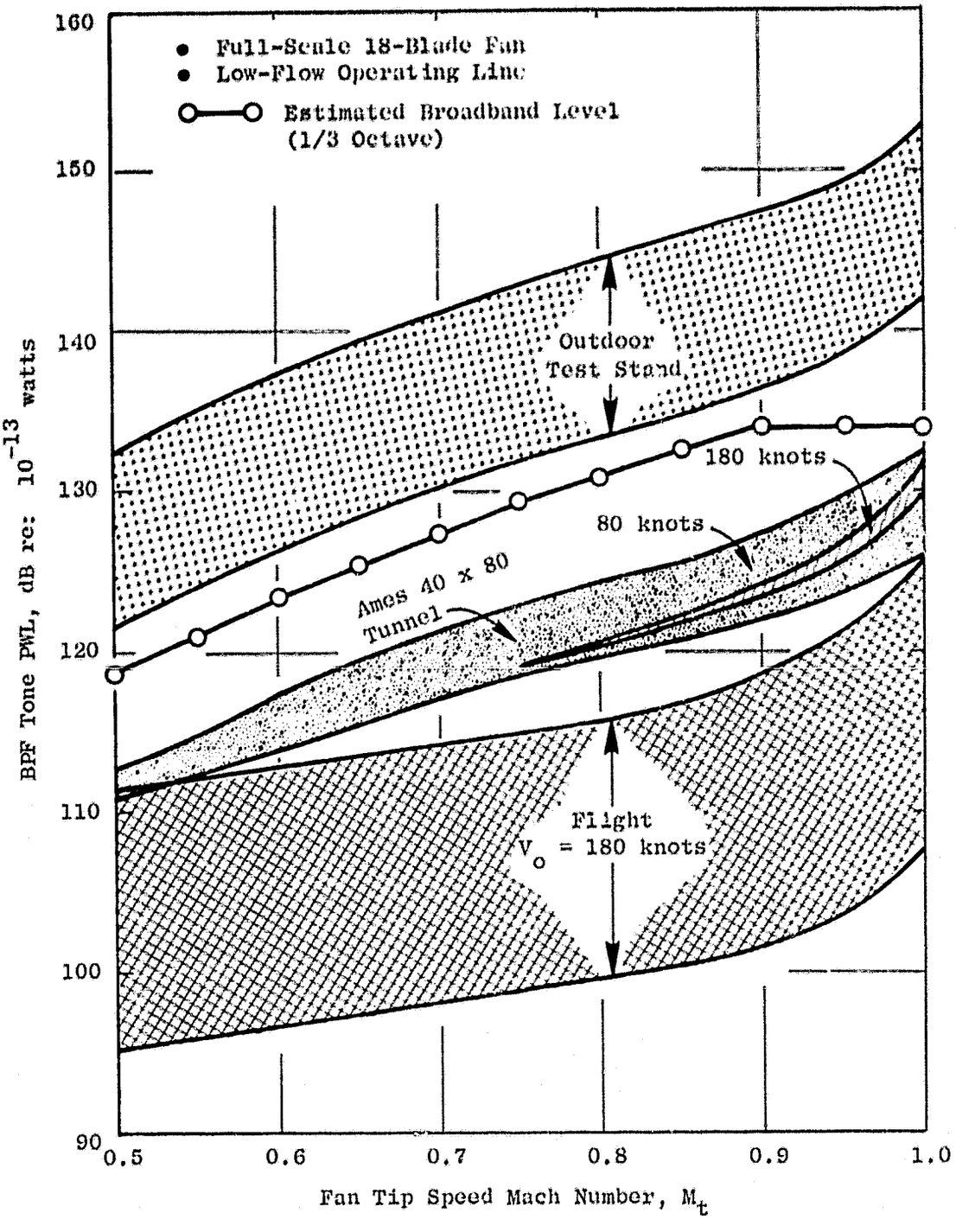

Figure 54. Predicted Variability in Rotor/Turbulence Noise BPF Tone PWL Due to Variations/Uncertainties in Fan Face Turbulence Levels.

tip incidence angle (relative air angle minus blade leading edge camberline angle). This correlation was used to estimate the broadband level (1/3 octave) at the blade-passing frequency, and these results are also shown in Figure 54. It can be seen that the NASA-Ames 40x80 Wind Tunnel Rotor/Turbulence tones are well below the predicted broadband levels at all but the highest tip speeds.

The spectral distribution of the rotor/turbulence tones is shown in Figure 55, compared with predicted 1/3-octave fan broadband noise spectra. It is apparent from this comparison that the higher harmonics of BPF rotor/turbulence tones are well below the fan broadband noise level for the Ames 40x80 Wind Tunnel case. Additional higher harmonic tone sources (i.e., rotor-stator interaction noise) will no doubt dominate the spectrum.

Finally, a check was made on the ability of the NASA-Ames 40x80 wind tunnel to simulate an aircraft accelerating taxi or "ground roll", where fan speed is held constant and wind speed or aircraft speed is increased from zero to some typical approach speed. Predictions were made of tone PWL for the JT15D engine (see DATA/THEORY COMPARISONS section) at a fan tip speed of M_t=0.93, over a range of tunnel velocities from 10 to 200 knots, using the sudden contraction theory (Reference 5). Taking into account the possibility that the transverse turbulence intensity at the fan face does not follow the sudden contraction theory but instead remains constant (Reference 24), additional calculations were made using Equation 26.

A "ground roll" calculation was also made, by specifying an initial precontraction static turbulence characteristic. This characteristic was chosen to yield approximate Outdoor Test Stand fan face turbulence at a very large contraction ratio. The flight speed was then progressively increased, causing contraction ratio to decrease, all the while holding precontraction turbulence properties constant.

The precontraction turbulence properties were selected based on the following reasoning. In an outdoor test stand, the transverse intensity at the fan face is typically 4%, which, for $U_a \approx 400$ fps at approach power setting, gives a fan face turbulence rms velocity of ~16 fps. From the data given by

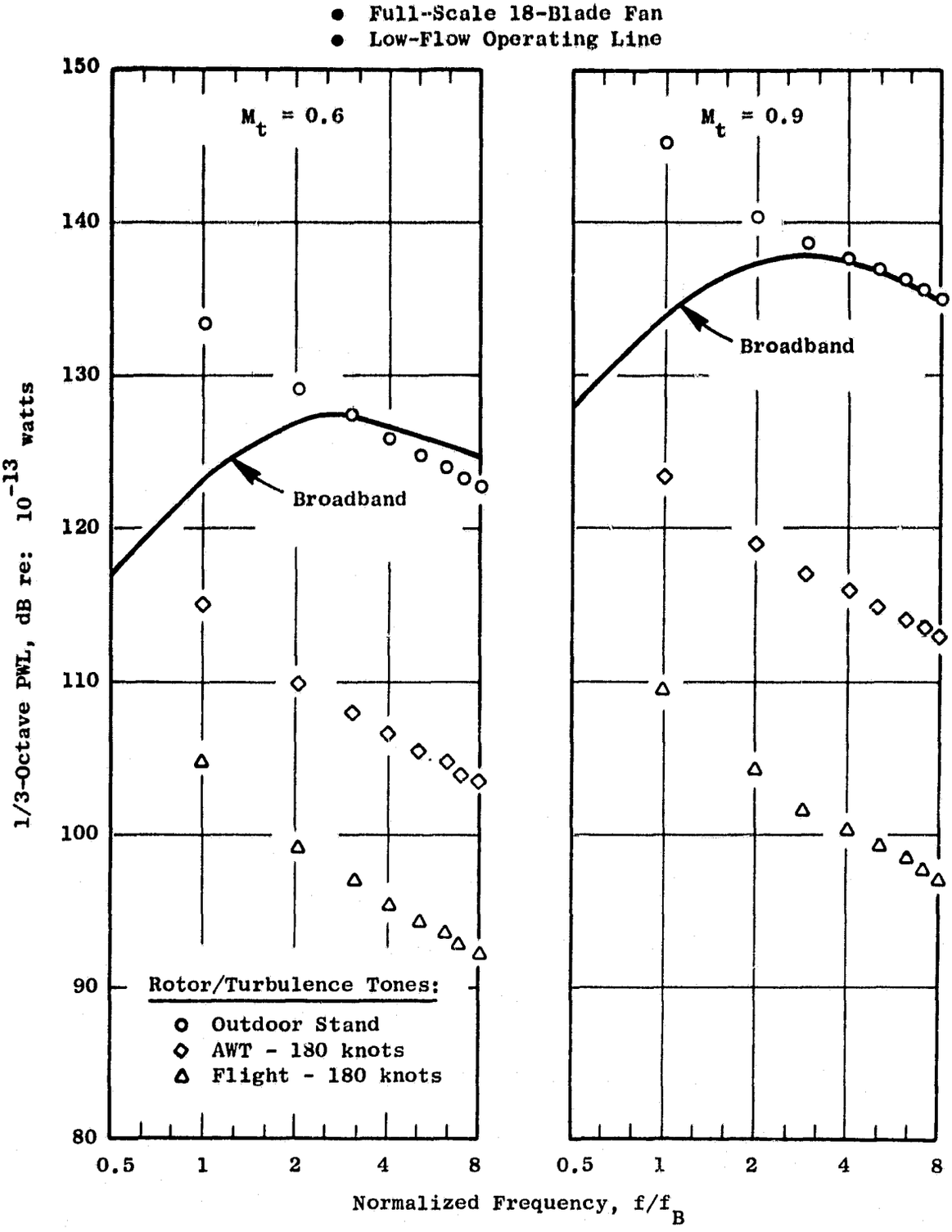

Figure 55. Comparison of Rotor/Turbulence Tone Levels with Fan 1/3-Octave Broadband Spectrum.

Houbolt (Reference 25), atmospheric turbulence levels are about 3 fps on a normal day. The implied transverse velocity ratio is 16/3 or 5.33, and sudden contraction theory then suggests that, for this velocity ratio, the contraction ratio is about C ≈ 40. Assuming a typical measured axial length scale inside the fan duct of ~100 ft, the corresponding transverse scale is ~0.4 ft, and the scale ratio $\ell_a/\ell_t \approx 250$, about what has been measured in Reference 6. The implied atmospheric length scale is $\ell \approx 2.5$ ft, not unrealistic for ground level turbulence. The sudden contraction theory then gives an axial turbulence intensity at the fan face of ~0.00053, much lower than the usually measured 0.005 to 0.010. However, it is the transverse intensity at the fan face which determines the noise level, so the underestimation of the axial intensity is of little consequence. It is also possible that these lower values of axial intensity cannot be properly measured due to instrumentation noise floors, contamination by acoustic velocity fluctuations, etc.

Figure 56 shows the results of the calculations described above. The "ground roll" curve shows a rapid decrease in tone level from the static level, reaching about 17 dB reduction at ~100 knots taxi speed. A similar effect was measured by Lowrie (Reference 30), his data showing approximately 15 dB reduction in BPF tone level at 80 knots, in an accelerating taxi test of a VC10-RB211 flying test bed. NASA Ames 40x80 Wind Tunnel test data on the JT15D engine (Contract NAS2-8675 with GE, unpublished data) is also shown in Figure 56. Considering the possible variability in atmospheric turbulence properties and the reasonable agreement between "ground-roll" predictions and both predicted and measured wind tunnel levels shown in Figure 56, it can be concluded that the 40x80 wind tunnel is an adequate simulation of rotor/turbulence noise forward-speed effects.

In summary, based on all the calculations and parametric studies discussed herein, it is concluded that the NASA-Ames 40x80 Wind Tunnel provides adequate suppression (or reduction) of rotor/turbulence noise such that proper simulation of flight fan source noise characteristics is obtained, for subsonic tip speeds. Near M_t approaching unity, wind tunnel rotor/turbulence tones may be as high as or higher than the broadband level, but cut-on of the rotor-alone noise field at $M_t = 1$ will probably mask this effect.

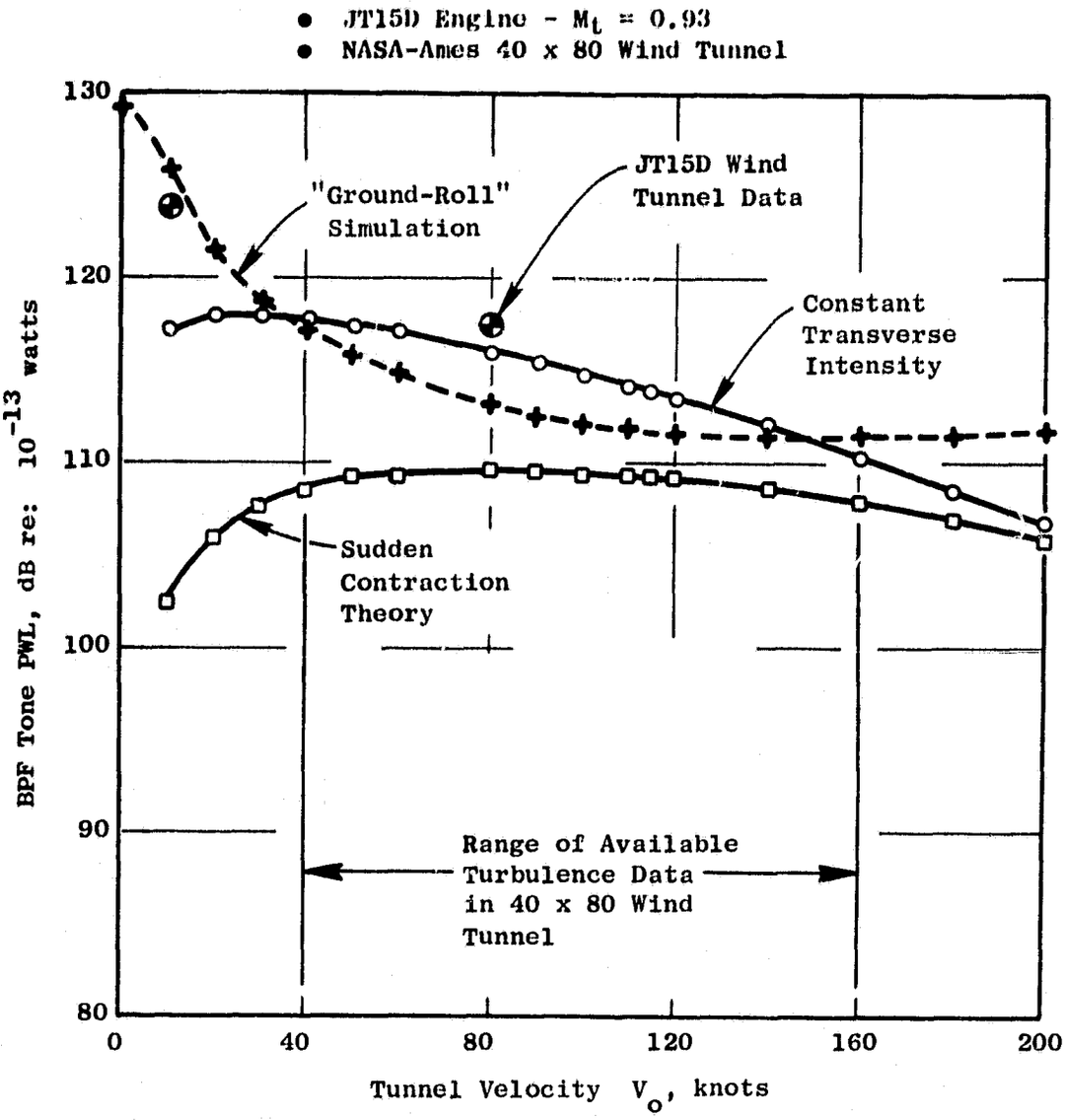

Figure 56. Comparison of Predicted "Ground Roll" Rotor/ Turbulence BPF Tone PWL with Predicted and Measured Wind Tunnel Turbulence Levels.

9.0 CONCLUSIONS

The following conclusions were drawn relative to the results obtained from this study:

1. The NASA-Ames 40x80 Wind Tunnel adequately simulates forward velocity effects on fan noise inlet arc tones produced by rotor/turbulence interaction, for fans from 0.5 to 2.0 m in diameter, for all subsonic tip speeds, and for blade numbers from 18 to 38. The simulation should be adequate for higher and lower values of diameter and blade number, but the present study was confined to the above ranges. The wind tunnel rotor-turbulence interaction tones are sufficiently low in level such that internally generated fan noise sources dominate the fan noise observed spectrum, and the rotor-turbulence noise has no contribution to the observed spectrum.

2. The adequacy of utilizing sudden contraction theory to predict fan inlet turbulence spectra from measured turbulence properties at some distance (several diameters) upstream of the fan inlet is questionable.

3. Rotor/turbulence interaction noise produced by ingestion of large-scale turbulence in a contracting inflow is primarily a narrow-band tone source, with no significant contribution to the fan broadband level.

4. For large scale inlet turbulence ($\ell > D_t$), the associated noise levels are primarily determined by the ratio of transverse turbulence scale to blade spacing at the fan face, and are not materially affected by axial scale if transverse scale is maintained constant. Maximum noise occurs when $\ell_t/s < 1$.

5. Rotor/turbulence noise in the NASA-Ames 40x80 Wind Tunnel is 15-20 dB below that produced in an outdoor static test stand for wind tunnel velocities greater than 40 kts. The reduction is due to the much smaller turbulence scales and intensities in the wind tunnel environment.

6. The Rotor/turbulence noise in the NASA-Ames 40x80 Wind Tunnel is 10-15 dB higher than that produced in flight at the same flight speed, but still several dB lower than the other sources of fan noise, e.g. broadband, rotor-alone multiple-pure-tones, rotor-stator interaction, etc. Even though the flight atmospheric turbulence intensities are higher, the turbulence scales are so large at altitude ($\ell_t/s \gg 1$) that the short wavelength components of the turbulence spectra have very low turbulence energy and so yield correspondingly low noise levels.

7. Under contracting inflow conditions ($U_a > V_o$), the transverse turbulence intensity controls the level of generated rotor/turbulence noise, and the axial intensity has a relatively small influence.

8. A rather wide uncertainty band in expected rotor/turbulence noise levels exists, $\pm$5-8 dB, for outdoor static and flight conditions, due to the random variability in turbulence conditions. The wind tunnel turbulence characteristics are, on the other hand, much more consistent.

REFERENCES

1. Hanson, D.B., "Spectrum of Rotor Noise Caused by Atmospheric Turbulence," Journal of the Acoustical Society of America, Vol. 6, No. 1, July 1974.

2. Mani, R., "Noise Due to Interaction of Inlet Turbulence With Isolated Stators and Rotors," Journal of Sound and Vibration," Vol. 17, No. 2, 1971, pp. 251-260.

3. Mani, R., "Isolated Rotor Noise Due to Inlet Distortion or Turbulence," NASA Contractor Report No. 2479, October 1974.

4. Mani, R. and Bekofske, K., "Experimental and Theoretical Studies of Subsonic Fan Noise," NASA Contractor Report No. 2660, March 1976.

5. Ribner, H.S. and Tucker, M., "Spectrum of Turbulence In a Contracting Stream," NACA Report 1113, 1953.

6. Kantola, R.A. and Warren, R.E., "Basic Research in Fan Source Noise - Inlet Distortion and Turbulence Noise," NASA Contractor Report No. 159451, December 1978.

7. Osborne, C., "Unsteady Thin-Airfoil Theory for Subsonic Flow," AIAA Journal, Vol. 11, No. 2, February 1973, pp. 205-209.

8. Amiet, R.K., "High-Frequency Thin-Airfoil Theory for Subsonic Flow," AIAA Journal, Vol. 14, No. 8, August 1976, pp. 1076-1082.

9. Goldstein, M.E., Dittmar, J.H., and Gelder, T.F., "Combined Quadrupole-Dipole Model For Inlet Flow Distortion Noise From a Subsonic Fan," NASA TN D-7676, May 1974.

10. Batchelor, G.K., "The Theory of Axisymmetric Turbulence," Proceedings of the Royal Society of London, Series A, Vol. 186, 1946, pp. 480-502.

11. Chandrasekhar, S., "The Theory of Axisymmetric Turbulence," Philosophical Transactions of the Royal Society of London, Series A, Vol. 242, 1950, pp. 557-577.

12. Sreenivasan, K.R. and Narasimha, R.N., "Rapid Distortion of Axisymmetric Turbulence," Journal of Fluid Mechanics, Vol. 84, Pt. 3, February 13, 1978, pp. 497-516.

13. Chandrashekhara, N., "Tone Radiation From Axial Flow Fans Running In Turbulent Flow," Journal of Sound and Vibration, Vol. 18, No. 4, 1971, pp. 533-543.

14. Chandrashekhara, N., "Sound Radiation From Inflow Turbulence In Axial Flow Fans," Journal of Sound and Vibration, Vol. 19, No. 2, 1971, pp. 133-146.

15. Robbins, B. and Lakshminarayana, B., "Effect of Inlet Turbulence on Compressor Noise," Journal of Aircraft, Vol. 11, No. 5, 1974, pp. 273-281.

16. Hanson, D.B., "Measurements of Static Inlet Turbulence," AIAA 2nd Aeroacoustics Conference, Hampton, Va., March 24-26, 1975, Paper No. 75-467.

17. Lakshminarayana, B., "Influence of Turbulence on Fan Noise," paper presented at the workshop on Ventilation System/Cooling Fan Noise, 19-20, November 1975, Naval Ship R.&D.C., Anapolis, Md.

18. Moiseev, N., Lakshminarayana, B., and Thompson, D.E., "Noise Due to Interaction of Boundary Layer Turbulence With a Compressor or a Propulsor Rotor," AIAA 3rd Aero-Acoustics Conference, Palo Alto, Calif., July 20-23, 1976, Paper No. 76-568.

19. Hodder, B.K., "Investigation of the Effect of Inlet Turbulence Length Scale on Fan Discrete Tone Noise," NASA-TM-X-62300, September 1973.

20. Hodder, B.K., "40- by 80-Foot Wind Tunnel Freestream Turbulence Measurements," FSA Technical Memorandum No. 17, April 22, 1977.

21. Shaw, L.M., Woodward, R.P., Glaser, F.W., and Dastoli, B.J., "Inlet Turbulence and Fan Noise Measured In an Anechoic Wind Tunnel and Statically With an Inlet Flow Control Device," AIAA 4th Aeroacoustics Conf., Atlanta, Ga., Oct. 3-5, 1977, Paper No. 77-1345.

22. Woodward, R.P., Wazyniak, J.A., Shaw, L.M., and MacKinnon, M.J., "Effectiveness of an Inlet Flow Turbulence Control Device to Simulate Flight Fan Noise In an Anechoic Chamber," NASA Tech. Memorandum No. TM-73855, 1977.

23. Bekofske, K.L., Sheer, R.E., and Wang, J.C.F., "Basic Noise Research Program - Fan Noise - Inlet Distortion and Turbulence Noise," Contract No. NAS3-17853, General Electric Company Contractor Final Report No. NASA CR-135177, February 1977.

24. Hodder, B.K., "The Effects of Forward Speed on Fan Inlet Turbulence and its Relation to Tone Noise Generation," NASA TM X-62, 381, August 1974.

25. Houbolt, J.C., "Atmospheric Turbulence," AIAA Journal, Vol. 11, No. 4, April 1973, pp. 421-437.

26. Bilwakesh, K.R., Clemons, A., and Stimpert, D.L., "Quiet Clean Short-Haul Experimental Engine (QCSEE) Acoustic Performance of a 50.8 cm (20-inch) Diameter Variable-Pitch Fan and Inlet, Test Results and Analysis, Vol. I," NASA CR-135177, April 1979.

27. Uberoi, M.S., "Effect of Wind-Tunnel Contraction on Free-Stream Turbulence," Journal of Aeronautical Sciences, Vol. 23, No. 8, August 1956, pp. 754-764.

28. Ginder, R.B. and Newby, D.R., "An Improved Correlation for the Broadband Noise of High Speed Fans," AIAA Journal of Aircraft, Vol. 14, No. 9, September 1977, pp. 844-849.

29. Gliebe, P.R., "The Effect of Throttling on Forward Radiated Fan Noise," AIAA 5th Aeroacoustics Conference, Seattle, Wash., March 12-14, 1979, Paper No. 79-0640.

30. Lowrie, B.W., "Simulation of Flight Effects on Aero Engine Fan Noise," AIAA Paper No. 75-463, 2nd Aeroacoustics Conference, Hampton, Va., March 24-26, 1975.

APPENDIX A

LONG AXIAL LENGTH SCALE APPROXIMATION

As discussed in Reference 2, the rotor/turbulence noise spectrum theoretical model employed in the present study consists of a summation of component spectra centered at blade-passing frequency and its harmonics, n = 1,2,3....., etc. The component spectra have shapes which are essentially the turbulence spectrum shape as axial wave number k_1 is varied over the range $-\infty \leq k_1 \leq +\infty$, with integrals over k_2 and k_3 performed at each value of k_1. This component summation is illustrated qualitatively in Figure 57.

For very large length scales $\ell_a/s \gg 1$, the component spectra 1-1, 2-2, 3-3, etc., shown in Figure 57 become very "peaky" and narrow, and the contributions of component spectra adjacent to a spectrum centered at $f=nf_b$ are negligible in the vicinity of $f=nf_b$. For example, the 1-1 and 3-3 component spectra in Figure 57 would contribute a negligible amount to the total spectrum at and around $f=2f_b$, and the 2-2 component is all that is required to evaluate the total spectrum level around $f=2f_b$.

When the spectrum around $f=nf_b$ is very narrow, as occurs when $\ell_a/s \gg 1$, the total power level contained in the peak can be evaluated by integrating over f and hence k_1. If the turbulence spectrum drops off very rapidly with k_1, compared to variations in either unsteady lift amplitude or quadrupole source amplitude, these factors can be approximated by their values at $k_1 = 0$ and the integral of only the turbulence spectrum over k_1 need be taken. Further, the spectrum levels need only be evaluated at harmonics of blade-passing frequency $f=nf_b$, where n = 1, 2, 3,....etc., and only the component spectrum centered at $f=nf_b$, i.e., the n-n component, need be calculated. Thus no summation of component spectra is required.

The integral of the turbulence spectra over k_1 can be derived in closed form from equations (16). The resulting expressions are as follows:

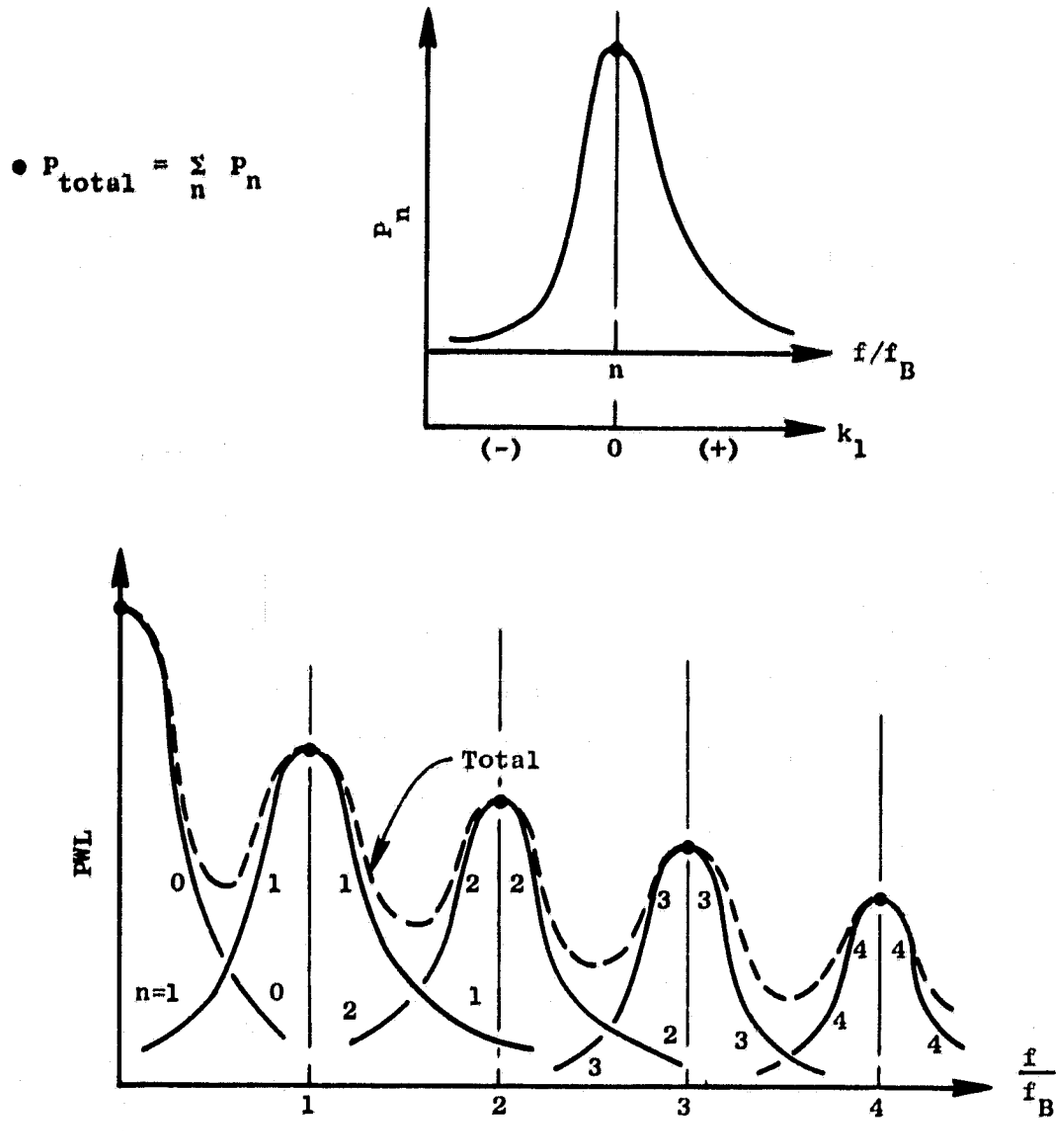

Figure 57. Illustration of Rotor/Turbulence Noise Prediction Model Component Contributions and Summation.

$$\phi^*_{11}(k_2) = \int_{-\infty}^{\infty} \tilde{\phi}_{11}(k_1,k_2)\, d\, k_1 = \frac{u_a^2\, \ell_t}{2\pi A_2^2}\left[1 + 2\,\frac{\ell_t^2\, k_2^2}{A_2^2}\right] \tag{27}$$

$$\phi^*_{12}(k_2) = \int_{-\infty}^{\infty} \tilde{\phi}_{12}(k_1, k_2)\, d\, k_1 = 0 \tag{28}$$

$$\phi^*_{22}(k_2) = \int_{-\infty}^{\infty} \tilde{\phi}_{22}(k_1, k_2)\, d\, k_1 = \frac{\ell_t\, u_t^2}{\pi A_2^2} \tag{29}$$

where

$$A_2^2 = 1 + k_2^2\, \ell_t^2 \tag{30}$$

Thus, in the long length-scale approximation $\ell_a/s \gg 1$, the total sound power in the vicinity of $f = nf_b$ is calculated by evaluating the unsteady lift dipole and quadrupole source strengths at $k_1=0$ and multiplying by a suitably weighted combination of the turbulence spectra given by equations (27-30) above.

It can be seen from equations (27-30) that the turbulence spectra for $\ell_a/s \gg 1$,i.e., integrated over k_1, are independent of ℓ_a/s. This is consistent with the results shown in Figure 10 which indicate that the noise level approaches a constant value independent of ℓ_a/s for $\ell_a/s \gg 1$. This occurs because the peak value at $f = nf_b$ (Figures 4 and 7) varies linearly with ℓ_a/s for $\ell_a/s \gg 1$, whereas the effective bandwidth decreases inversely with ℓ_a/s.

When the turbulence undergoes a contraction, the long length-scale approximation can still be employed. Referring to equations (19-21), the postcontraction spectra $\Phi_{11}(\underline{\kappa})$ and $\Phi_{22}(\underline{\kappa})$ only need to be considered since for $\ell/s \gg 1$ the integral over k_1 (or κ_1) of $\Phi_{12}(\underline{\kappa})$ vanishes. Now the integral over κ_1 of Φ_{11} and Φ_{22} involves the expression

$$\int_{-\infty}^{\infty} \phi_{11}(\underline{\kappa})\, d\,\kappa_1 = \frac{1}{C} \int_{-\infty}^{\infty} \phi_{11}(\underline{\kappa})\, d\, k_1$$

and a similar one for ϕ_{22}. It can be seen from examination of equations (19-21) that only the leading terms will contribute significantly since they involve the integrals $\int \phi_{11}\, dk_1$ and $\int \phi_{22}\, dk_1$, whereas the remaining terms involve $\int k_1^N\, \phi_{ij}\, dk_1$, which should be small if ϕ_{ij} drops off rapidly enough with k_1. The postcontraction spectra corresponding to equations (27-29) can therefore be approximated by the following:

$$\phi_{11}^*(\kappa_2) = \iint_{-\infty}^{\infty} \phi_{11}(\underline{\kappa})\, d\kappa_3 d\kappa_1 \approx \frac{\sqrt{C}}{C} \iint_{-\infty}^{\infty} \frac{1}{C^2}\, \phi_{11}(\underline{k})\, dk_3 dk_1$$

or

$$\phi_{11}^*(\kappa_2) \approx \frac{1}{\sqrt{C}}\, \frac{\phi_{11}^*(k_2)}{C^2} \tag{31}$$

Similarly,

$$\phi_{22}^*(\kappa_2) \approx \frac{1}{\sqrt{C}}\, C\, \phi_{22}^*(k_2) \tag{32}$$

where $k_2 = \kappa_2/\sqrt{C}$, as before. Equations (31,32) are used in place of (27,29) to account for contraction effects for $C = U_a/V_o \geq 1$.

APPENDIX B

SYMBOLS AND ABBREVIATIONS

A	- Fan rotor inlet annulus area, also turbulence spectrum variable
AWT1	- Ames wind tunnel, V_o = 80 knots
AWT2	- Ames wind tunnel, V_o = 180 knots
a	- Constant
BPF	- Blade-passing frequency
C	- Contraction ratio
C_ℓ	- Rotor blade lift coefficient
CR	- Contraction ratio
c	- Rotor blade chord
DV	- Discharge valve (throttle) setting
D_t	- Fan rotor tip diameter
$F(\underline{k})$	- Turbulence spectrum function
FLT	- Flight, V_o = 180 knots
f	- Frequency, also isotropic turbulence correlation function
f_B	- Blade-passing frequency
$G(\underline{k})$	- Turbulence spectrum function
g	- Isotropic turbulence correlation function
HF	- High-flow operating line of M_a versus M_t
HS	- Half-scale
h	- Blade height
$\underline{k}$	- Precontraction wavenumber
k_i	- i^{th} component of $\underline{k}$
L	- Turbulence integral length scale
LF	- Low flow operating line of M_a versus M_t
ℓ	- Isotropic turbulence length scale
ℓ_a	- Axisymmetric turbulence axial length scale
ℓ_t	- Axisymmetric turbulence transverse length scale
M_a	- Fan inlet axial Mach number
M_t	- Fan inlet tip speed Mach number
M_r	- Fan inlet relative Mach number $\sqrt{M_a^2+M_t^2}$

N_B - rotor blade number

N_F - fan rotative speed, rpm

n - blade-passing frequency harmonic number

OTS - outdoor test stand

P - acoustic power, watts

P_o - peak acoustic power, watts

P_1 - acoustic power at band edge, watts

P_t - total acoustic power in band, watts

PWL - acoustic power level, dB re: 10^{-13} watts

PWL_o - decibel equivalent of P_o

PWL_1 - decibel equivalent of P_1

PWL_t - decibel equivalent of P_t

ΔPWL - $PWL_o - PWL_1$

Q_1, Q_2, Q_3 - axisymmetric turbulence correlation functions

q_{ij} - axisymmetric turbulence correlation tensor

QS - quarter-scale

R_{ij} - turbulence velocity correlation function

r - spanwise radial coordinate

r_h - rotor inlet hub radius

r_t - rotor inlet tip radius

r_p - rotor inlet rms pitchline radius

SAC - Schenectady anechoic chamber

s - blade-to-blade spacing $2\pi r/N_B$

TCS - turbulence control structure

U - local mean flow velocity

U_a - fan rotor inlet axial velocity

U_t - fan rotor inlet tip speed

u_a - axial component of rms turbulence velocity

u_t - transverse component of rms turbulence velocity

V_o - wind tunnel velocity or flight speed

x_i - i^{th} component of separation vector $\underline{x}$

x_t - transverse separation $\sqrt{x_2^2+x_3^2}$

Γ_{ij} - turbulence spectrum coefficient

δ_{ij} - kronecker delta

ϵ_{ijk} - alternating unit tensor

θ - integration variable

$\underline{\kappa}$ - postcontraction wavenumber

κ_i - i^{th} component of $\underline{\kappa}$

λ - length scale ratio ℓ_a/ℓ_t

μ - turbulence velocity ratio u_t/u_a

τ - cross-correlation time delay

Φ_{ij} - precontraction three-dimensional turbulence spectrum

$\tilde{\Phi}_{ij}$ - precontraction two-dimensional turbulence spectrum

Φ_{ij} - postcontraction three-dimensional turbulence spectrum

$\tilde{\Phi}_{ij}$ - postcontraction two-dimensional turbulence spectrum

Subscripts

1 - axial direction

2 - tangential direction

3 - radial direction

0 - free stream

a - axial

t - transverse, tangential, tip

b - blade

p - pitchline

h - hub